Space Division Multiple Access Systems: Computational Electromagnetic Studies of the Physical and Network Layers

by

Kapil Ramesh Dandekar, B.S.E.E, M.S.E.

Dissertation

Presented to the Faculty of the Graduate School of

The University of Texas at Austin

in Partial Fulfillment

of the Requirements

for the Degree of

Doctor of Philosophy

The University of Texas at Austin

May 2001

Space Division Multiple Access Systems: Computational Electromagnetic Studies of the Physical and Network Layers

Approved by
Dissertation Committee:

Guanghan Xu, Co-Supervisor

Hao Ling, Co-Supervisor

Space Division Multiple Access Systems: Computational Electromagnetic Studies of the Physical and Network Layers

Publication No._____

Kapil Ramesh Dandekar, Ph.D.

The University of Texas at Austin, 2001

Supervisors: Guanghan Xu, Hao Ling

Space Division Multiple Access (SDMA) systems exploit the spatial diversity of mobile users for the purpose of increasing the quality and capacity of cellular communications systems. SDMA systems exploit spatial diversity through the use of smart antenna arrays at the base stations of cellular systems. This dissertation demonstrates how electromagnetic modeling techniques can be applied to the holistic study of SDMA systems. This research develops a foundation for unifying low-level electromagnetic principles with propagation and system-level concepts in communication system performance. Specifically, computational electromagnetics techniques, including electromagnetic ray tracing and the Method of Moments, are applied to study low-level radio frequency propagation statistics and mutual coupling characteristics as well as high-level SDMA system planning issues. Whenever possible, empirical data, collected

using the smart antenna testbed at the University of Texas at Austin, is used to guide simulation construction and verify simulation results.

This dissertation demonstrates through field measurements and simulation how consideration of the mutual coupling in an SDMA system can improve direction finding and downlink beamforming performance. This study also illustrates a novel use of computational electromagnetics in the simulation and prediction of the urban vector channel encountered by SDMA systems. Specifically, ray tracing is used to examine power-angle profiles, power-delay profiles, spatial signature angle change, and downlink beamforming in urban environments. In addition, a new vector autoregressive, Kalman filter-based approach is used to predict spatial signatures in a time division duplexed SDMA system. Finally, the tools used in this dissertation culminate in the development of a system-planning and channel visualization software package for SDMA systems. This package is used in a novel study of urban vector channel propagation statistics as well as urban microcell architecture and handoff.

Table of Contents

List of Tables

List of Figures

Chapter 1 – Introduction

1.1 – MOTIVATION

Space Division Multiple Access (SDMA) systems exploit the spatial diversity of mobile users for the purpose of increasing the quality and capacity of cellular communications systems. SDMA systems exploit spatial diversity through the use of smart antenna array systems at the base stations of cellular systems. The communication channel encountered by this array of antennas is referred to as the vector channel.

This dissertation demonstrates how electromagnetic modeling techniques can be applied to the holistic study of SDMA systems. Past studies of SDMA systems generally focused on smart antenna array signal processing algorithm simulation and thus considered the underlying vector channel to be a black box. Similarly, most past studies of adaptive antenna arrays considered the system from a purely electromagnetic perspective independent of application in communications or radar systems. Fundamentally, this work develops a foundation for unifying low-level electromagnetic principles with propagation and system level concepts in communication system performance. Specifically, computational electromagnetics techniques, including electromagnetic ray tracing (ERT) and the Method of Moments (MoM), are used to investigate:

1. Mutual coupling characteristics
2. Radio frequency (RF) propagation statistics
3. SDMA urban microcell system planning issues

Whenever possible, empirical data, collected using the smart antenna testbed at the University of Texas at Austin, is used to guide simulation construction and verify simulation results.

1.2 – DISSERTATION ORGANIZATION

Figure 1.1 illustrates the hierarchy of topics that are studied in this dissertation.

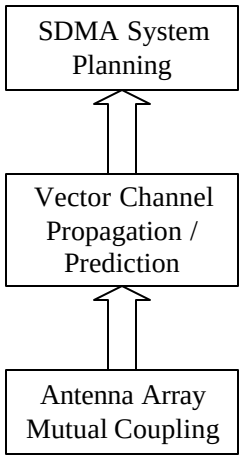

Figure 1.1 – Research Topic Hierarchy

Chapter 2 of this dissertation provides background information on SDMA systems necessary for later chapters. Chapter 3 starts at the bottom topic illustrated in Figure 1.1, antenna array mutual coupling, and describes the measurements and MoM-based simulations conducted in this area. As illustrated by Figure 1.1, Chapter 4 makes use of further MoM and ERT simulations along with field measurements to present a higher-level study of vector channel propagation and prediction. As the highest level of the figure drawing on the developed computational techniques, a system-planning and visualization tool for

SDMA systems is presented in Chapter 5. Chapter 6 concludes the dissertation with a summary of the completed work.

Chapter 2 – Background Information

Designers need to develop methods for increasing system capacity to fulfill the continually increasing demand for wireless services. The need to increase system capacity motivated the advent of multiple access techniques that efficiently distribute limited bandwidth among competing users. Time Division Multiple Access (TDMA) increases system capacity by allowing multiple users to transmit at the same frequency, but in different time slots. Frequency Division Multiple Access (FDMA) systems assign each user their own frequency slot in which they can transmit simultaneously. Code Division Multiple Access (CDMA) increases system capacity through a more abstract method: multiple users are allowed to transmit at the same time and frequency, but are each assigned a unique code through which the information they transmit can be extracted.

Space Division Multiple Access (SDMA), which can theoretically be used in conjunction with any of the other multiple access schemes mentioned above, exploits the spatial diversity of multiple users (possibly transmitting at the same time and frequency) to increase system capacity. In essence, mobile users can be distinguished since they are each transmitting from different locations. The base station makes use of a smart antenna array and, for the purposes of this study; the mobile user has a conventional antenna. Spatial diversity can be exploited in both uplink (mobile user transmitting to base station) and downlink (base station

transmitting to mobile user). Uplink transmission in an SDMA system is illustrated in Figure 2.1.

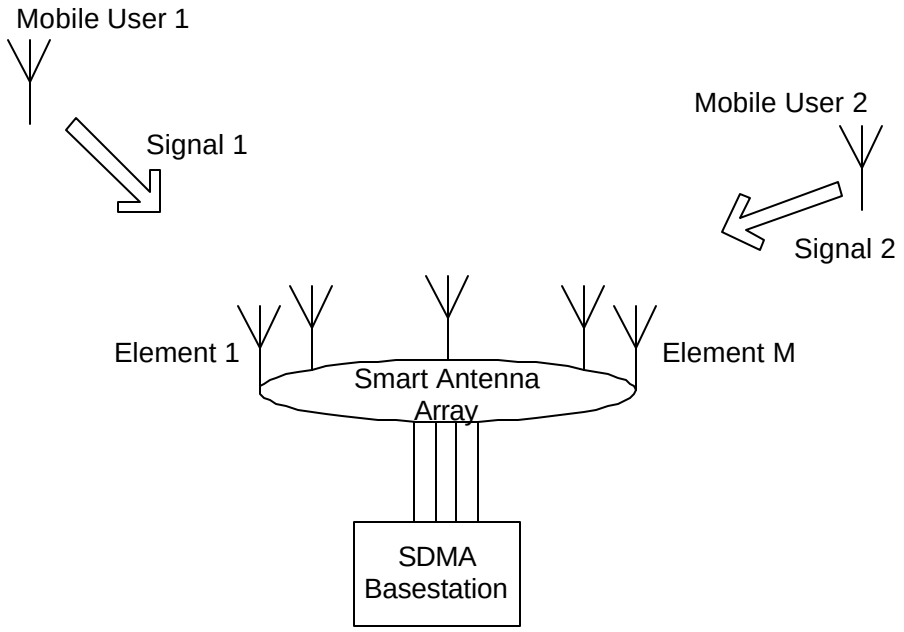

Figure 2.1 – SDMA System Operation (Uplink)

2.1 – DIRECTIONAL TRANSMISSION AND RECEPTION

It is necessary to consider the operation of smart antenna systems from an electromagnetic perspective in order to fully understand the manner in which SDMA systems operate. By definition, a smart antenna is an antenna array that dynamically adapts its radiation pattern to improve some aspect of system performance. A radiation pattern is a plot of transmitted power versus angle during downlink. The overall radiation pattern of a smart antenna system is determined by the relative amplitude and phase of the excitation currents fed to each of the antenna array elements. It is possible to choose these excitation currents such that, far from the array, the overall array radiation pattern is focused

in a desired direction, allowing for directive transmission. By the principle of superposition of electric fields, directional transmission in several directions simultaneously is possible by simply taking a linear combination of the vector of excitation currents used to drive the array. Directional transmission techniques will be discussed in greater detail in Section 2.6. By the principle of reciprocity, directional reception is possible by taking an appropriate linear combination of signals received from each element in the antenna array.

It is important to make the distinction between downlink and uplink smart antenna operation. During downlink, the overall radiation pattern of the array is modified through use of array excitation currents. During uplink, however, the array is operating in a passive mode in which incident electromagnetic signals from mobile users induce currents on the array elements. Signal processing algorithms are applied to these signals to obtain directional uplink information.

The collective directional uplink and downlink capability of smart antenna arrays is referred to as beamforming. During downlink, beamforming techniques can be used to place nulls in the overall array radiation pattern. This allows the antenna array to have active interference suppression when necessary. For example, during the downlink period in an SDMA system with two mobile users, the smart antenna can be used to focus mobile user data to the appropriate user while placing a null in the radiation pattern of the other mobile user. This allows the interference signal seen by one mobile user (i.e. the downlink data intended for the other mobile) to be minimized. This idea is illustrated in Figure 2.2.

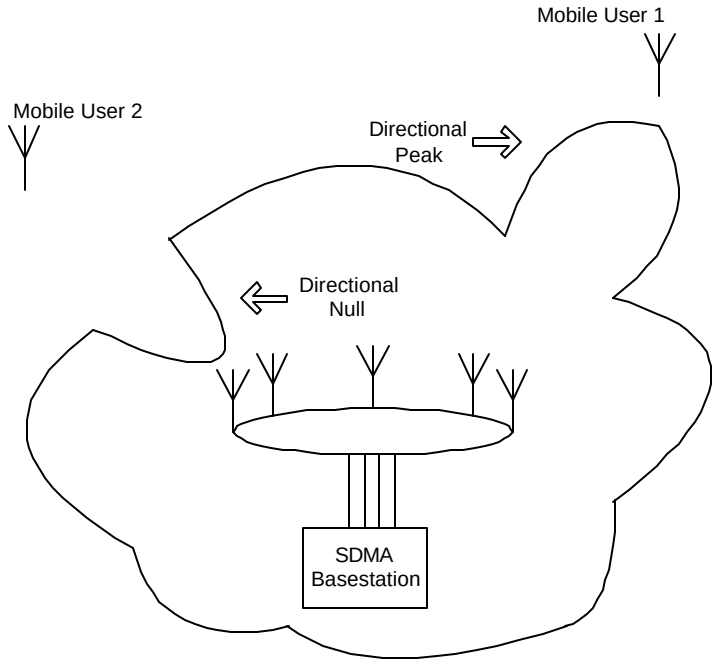

Figure 2.2 – Illustration of Directional Transmission / Nulling (Downlink)

2.2 – SYSTEM BLOCK DIAGRAM

The basic components of an SDMA system are illustrated in Figure 2.3. During uplink operation, the received signals from the antenna array are first processed by the receive beamformer. This is a purely mathematical operation that uses either a direction of arrival (DOA) algorithm or a spatial signature estimation algorithm.

DOA signal processing algorithms detect how much power is incident upon the array from various directions of arrival. This power versus incident angle graph is referred to as a spatial spectrum. The manner in which the spatial spectrum is generated depends upon which DOA algorithm is being used. The algorithms used in this dissertation are described in greater detail in Section 2.5.

While the spatial spectrum is not a power spectrum in the conventional sense of the term, it yields valuable information that allows the DOAs of the various users to be extracted.

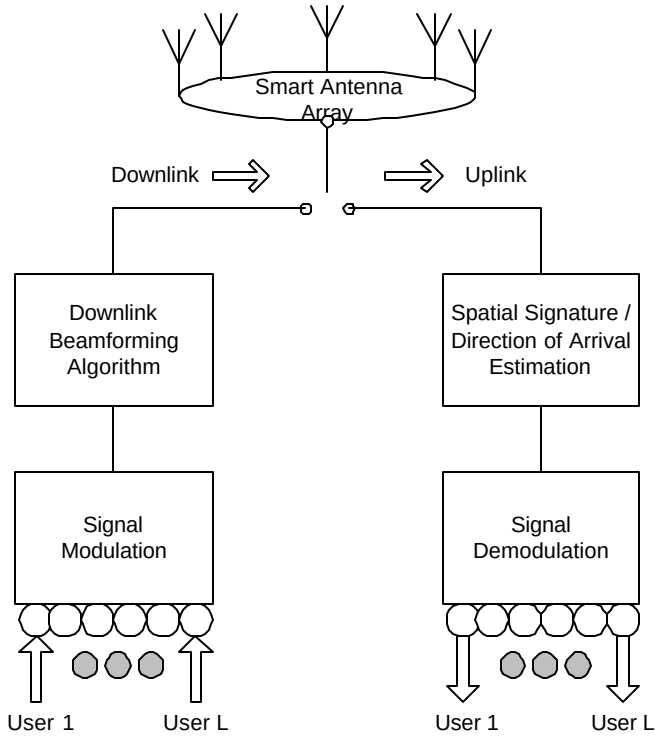

Figure 2.3 – SDMA System Block Diagram

A spatial signature estimation algorithm determines a vector for each mobile user that characterizes the spatial diversity of that mobile user. Spatial signatures are defined in Section 2.4 and algorithms describing their estimation can be found in [1-3]. Once the DOAs or estimated spatial signatures have been associated with the user transmitting the information, the individual signal of each mobile user can be extracted.

The base station also uses the estimated DOA or spatial signature information during downlink for directional transmission. This information is used to excite the individual elements in the antenna array to transmit the modulated signal. How this is done depends upon which downlink beamforming method is in use. The beamforming methods considered in this study are described in Section 2.6.

2.3 – STEERING VECTOR CONCEPT

Assume that there are M elements in the base station antenna array located at (x_i, y_i), $1 \le i \le M$. A steering vector, $\vec{\mathbf{a}}(\theta)$, (sometimes called array response vector) can be thought of as the spatial analog of an impulse response in temporal processing. Specifically, it characterizes the relative phase response of each antenna array element to an incident signal with DOA θ. Equation (2.1) represents the basic form of the theoretical (uncompensated) steering vector and an illustration of this concept is given in Figure 2.4.

$$\vec{\mathbf{a}}_U(\mathbf{?}) = \begin{bmatrix} \exp(-jk(x_1 \cos\theta + y_1 \sin\theta)) \\ \cdots \\ \exp(-jk(x_M \cos\theta + y_M \sin\theta)) \end{bmatrix} \tag{2.1}$$

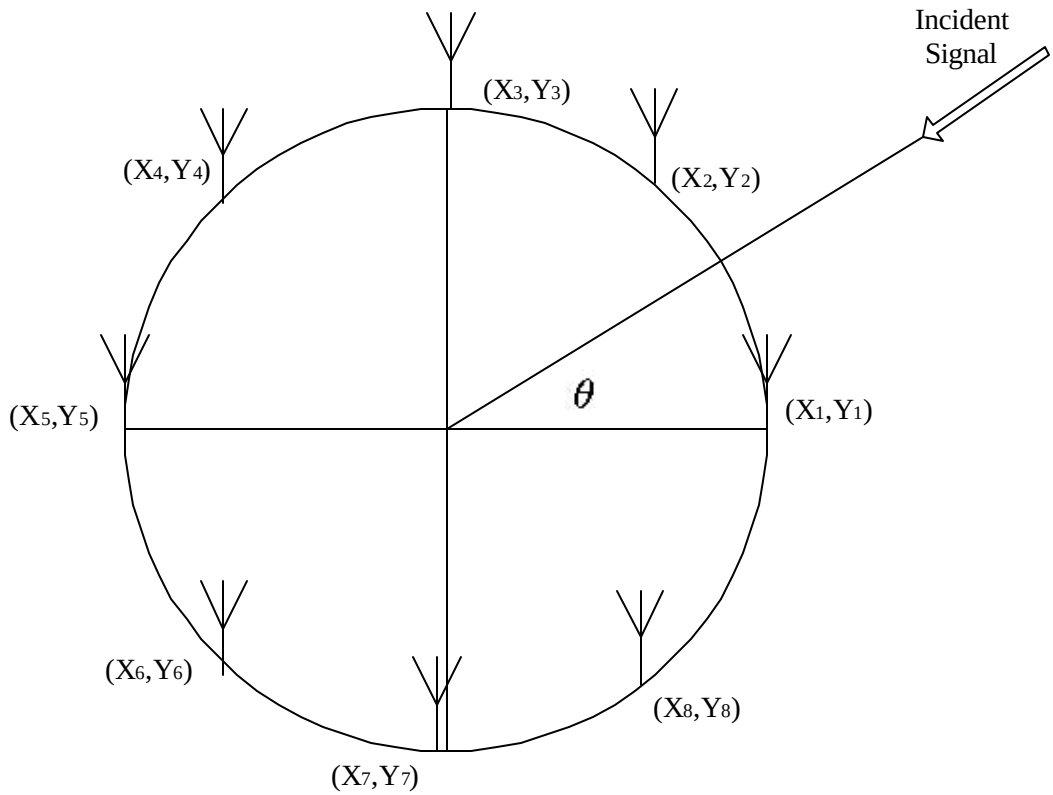

Figure 2.4 – Illustration of Steering Vector Concept

$k=2\pi/\lambda$ is the wavenumber of the incident electromagnetic radiation. At 1.8 GHz, the signal wavelength is approximately 16.7 cm. An array manifold matrix, **A**, contains as its columns a collection of steering vectors corresponding to a finite set of angles.

2.4 – VECTOR CHANNEL PROPAGATION MODEL

The Spatial Signature model considers the signal received by the antenna array due to a single user to be a linear combination of the steering vectors of all direct path and multipath components. In the model, the coefficients applied to

each of the steering vectors are dependent upon the relative amplitude and phase of the DOA. The relative amplitude of each steering vector coefficient models the path loss due to reflection and diffraction that a particular multipath DOA encounters when traveling from the mobile user to the base station antenna array. The relative phase of each of the steering vector coefficient models the delay of the DOA due to the different path lengths taken from mobile user to antenna array. The direct path component of this superposition of steering vectors is defined to have relative amplitude of 1 and a relative phase of 0. The signal received at the antenna array by a single mobile user, $\vec{\mathbf{x}}_1(t)$ (in the absence of noise) is:

$$\vec{\mathbf{x}}_1(t) \cong \alpha_1(t)\vec{\mathbf{a}}(\theta_1)s_1(t) + \sum_{i=2}^{N_M(t)} \alpha_i(t)\vec{\mathbf{a}}(\theta_i)s_1(t) = \vec{\mathbf{a}}_1(t)s_1(t) \tag{2.2}$$

Here, $\vec{\mathbf{a}}(\theta_1)s_1(t)$ is the direct path component and $\alpha_i(t)\vec{\mathbf{a}}(\theta_i)s_1(t)$, $2 \le i \le N_M(t)$, are the multipath components. The α_i contain the relative amplitude and phase of the ith signal component with α_1=1 by definition. $\vec{\mathbf{a}}_1(t)$ is defined to be the spatial signature of mobile user 1; this procedure can be repeated to create spatial signatures for all L mobile users in the system. With noise in the system, $\vec{\mathbf{x}}_1(t)$, can also be simply written as:

$$\vec{\mathbf{x}}(t) = \vec{\mathbf{a}}_1(t)s_1(t) + \vec{\mathbf{n}}(t) \tag{2.3}$$

Representing the output of the antenna array in this way requires a narrowband assumption [4,5] be used. This assumption states that the longest delay of a multipath signal component must be much less than the inverse of the signal bandwidth. Equation (2.2) is not adequate if this assumption does not hold. This is the motivation behind the Spatial Channel Impulse Response Model,

which additionally considers the delay, Δ_i, of the ith signal component if the minimum delay is greater than the inverse signal bandwidth. This method expresses the array output as [5]:

$$\vec{\mathbf{x}}(t) = \alpha_1(t)\vec{\mathbf{a}}(\theta_1)s_1(t-\Delta_1) + \sum_{i=2}^{N_M(t)} \alpha_i(t)\vec{\mathbf{a}}(\theta_i)s_1(t-\Delta_i) \tag{2.4}$$

For vector channel models based upon environmental effects, the paper by Ertel [6] provides a good introduction. Other than the ray tracing approach discussed by Ertel (that will be further seen in Chapter 4), many of the methods discussed in that paper are statistical characterizations of typical cellular communications scenarios.

2.5 – UPLINK DIRECTION OF ARRIVAL ALGORITHMS

An important quantity in many array signal processing algorithms is the Spatial Covariance Matrix, **R**, defined as:

$$\mathbf{R} = E\left(\vec{\mathbf{x}}(t)\vec{\mathbf{x}}^H(t)\right) \tag{2.5}$$

$\vec{\mathbf{x}}^H(t)$ indicates the complex conjugate transpose of vector $\vec{\mathbf{x}}(t)$. In practice, this matrix is estimated using N snapshots of the actual antenna array output (with sampling interval T):

$$\tilde{\mathbf{R}} = \frac{1}{N}\sum_{k=1}^{N} \vec{\mathbf{x}}(kT)\vec{\mathbf{x}}^H(kT) \tag{2.6}$$

An eigenvalue decomposition of **R** can be used to find the orthogonal projector onto the estimated noise subspace, $\Pi^{\perp}$. The equations for the Bartlett and Multiple Signal Classification (MUSIC) spatial spectra can be derived using this information, along with knowledge of the steering vectors of the array.

$$\mathbf{P}_{\text{BARTLETT}}(\theta) = \frac{\vec{\mathbf{a}}^H(\theta)\tilde{\mathbf{R}}\vec{\mathbf{a}}(\theta)}{\vec{\mathbf{a}}^H(\theta)\vec{\mathbf{a}}(\theta)} \tag{2.7}$$

$$\mathbf{P}_{\text{MUSIC}}(\theta) = \frac{\vec{\mathbf{a}}^{\text{H}}(\theta)\vec{\mathbf{a}}(\theta)}{\vec{\mathbf{a}}^{\text{H}}(\theta)\Pi^{\perp}\vec{\mathbf{a}}(\theta)} \tag{2.8}$$

For a survey of DOA algorithms and their derivation, refer to Krim [4].

2.6 – DOWNLINK BEAMFORMING ALGORITHMS

DOA information, gathered during uplink, is used by a downlink beamforming algorithm to efficiently transmit information from the base station to the mobile user. Each downlink beamforming method has its own technique for how best to accomplish this efficient transmission [7-9]. Each algorithm determines a weight vector, $\vec{\mathbf{w}}$, that is a function of either the mobile user DOAs or spatial signatures estimated during uplink. This function reflects the strategy used for the placement of directional peaks and nulls.

2.6.1 Dominant DOA Method

The Dominant DOA (DomDOA) method is the most intuitive of the downlink beamforming methods. In principle, for a given mobile user, it takes the angle at which there is the greatest received power during uplink and focuses all transmitted energy in that direction. This concept is illustrated in Figure 2.5.

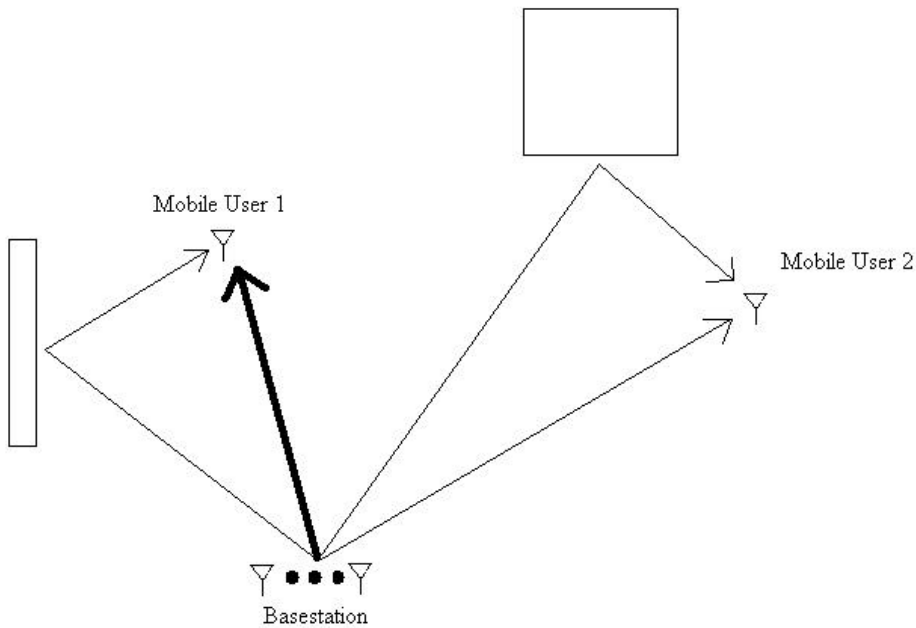

Figure 2.5 – Dominant DOA Beamforming Method Illustration

The arrows above represent various paths that transmitted energy can take from the base station to each of the mobile users (and vice versa). The highlighted arrow illustrates the DOA that would be identified by the DomDOA method to transmit to mobile user 1. The downlink weight chosen is simply the steering vector corresponding to angle, $\theta_{Dom} = \arg\max_{\theta} P(\theta)$, the angle corresponding to the maximum uplink spatial spectrum value.

$$\vec{\mathbf{w}}_{DomDOA} = \vec{\mathbf{a}}(\theta_{Dom}) \tag{2.9}$$

2.6.2 Pseudoinverse DOA Downlink Beamforming Method

The Pseudoinverse DOA (PseDOA) method is conceptually similar to the DomDOA method. In addition to transmitting in the direction of the strongest DOA of the desired user, the PseDOA method places nulls in the array radiation

pattern at both the non-dominant DOAs of the desired user and all the DOAs of any other mobile users. Instead of trying to maximize signal power alone, signal power is maximized while minimizing interference power seen by other mobile users. This concept is illustrated in Figure 2.6.

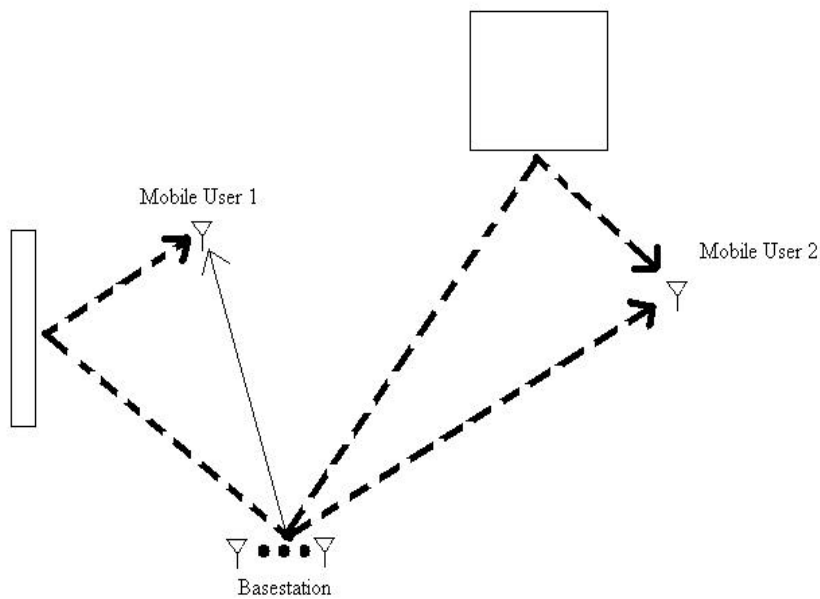

Figure 2.6 – Pseudoinverse DOA Method Illustration

The dashed lines indicate the non-dominant DOA of the mobile user 1 and all DOAs of mobile user 2 which are nulled by the transmitting base station. The non-dashed line indicates the direction in which transmission is focused just as in the DomDOA method. To illustrate how the weight is constructed using the PseDOA method, we first construct the matrix with the following partitions as shown in equation (2.10), and then apply equation (2.11):

$$\mathbf{X} = \begin{bmatrix} \vec{\mathbf{a}}(\theta_{\mathrm{DOM}}) & \hat{\mathbf{A}}_1 & \mathbf{A}_2 \end{bmatrix} \tag{2.10}$$

$$\vec{\mathbf{w}}_{\text{PseDOA}} = \{\text{row}(\text{pinv}(\mathbf{X}),1)\}^{\text{H}} \tag{2.11}$$

$\vec{\mathbf{a}}(\theta_{\text{DOM}})$ is the steering column vector of the dominant DOA of user 1 and $\mathbf{A_2}$ is the array manifold matrix of mobile user 2. $\hat{\mathbf{A}}_1$ is the array manifold matrix of mobile user 1 with the column corresponding to the dominant DOA of user 1 eliminated. The resulting weight vector is orthogonal to the non-dominant DOAs of mobile user 1 and all DOAs of mobile user 2.

2.6.3 Spatial Signature Downlink Beamforming Method

The Spatial Signature (SS) method uses the spatial signature of mobile user 1 alone when constructing the downlink weight vector. Since the representation of spatial signature encapsulates the relative magnitude and phase of energy coming from different directions during uplink, this information is similarly applied during downlink using this method. Figure 2.7 illustrates this concept.

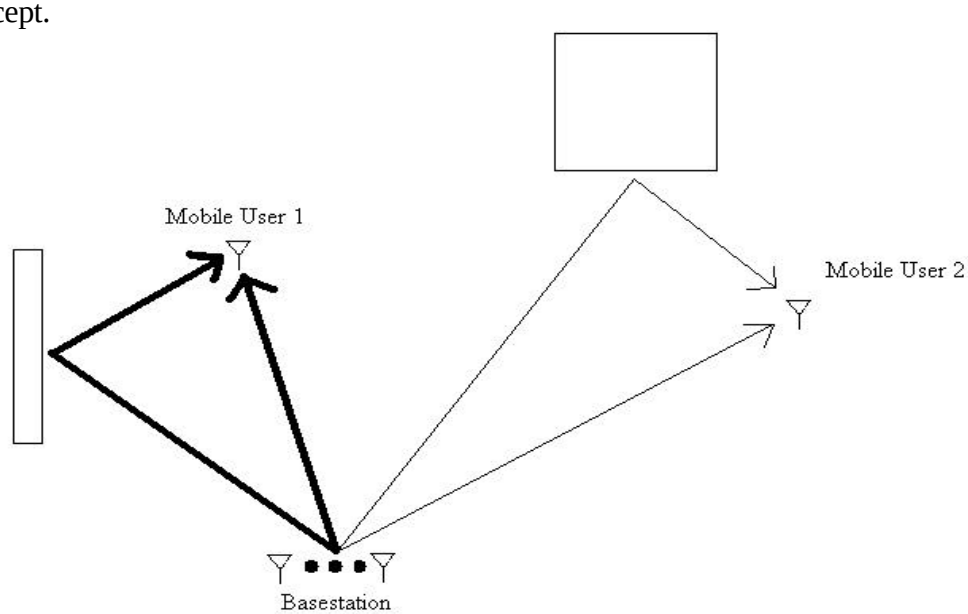

Figure 2.7 – Spatial Signature Method Illustration

The dark lines illustrate the directions in which the beam will be steered by the base station. The equation for the weight vector in the SS method is simply the spatial signature of the desired mobile user.

$$\vec{\mathbf{w}}_{SS} = \vec{\mathbf{a}}_1 \tag{2.12}$$

2.6.4 Pseudoinverse Spatial Signature Downlink Beamforming Method

The final downlink beamforming method considered in this dissertation is the Pseudoinverse Spatial Signature (PseSS) method. In this method nulls are inserted at the DOAs corresponding to the spatial signature of the other mobile users in the system. Figure 2.8 illustrates this concept.

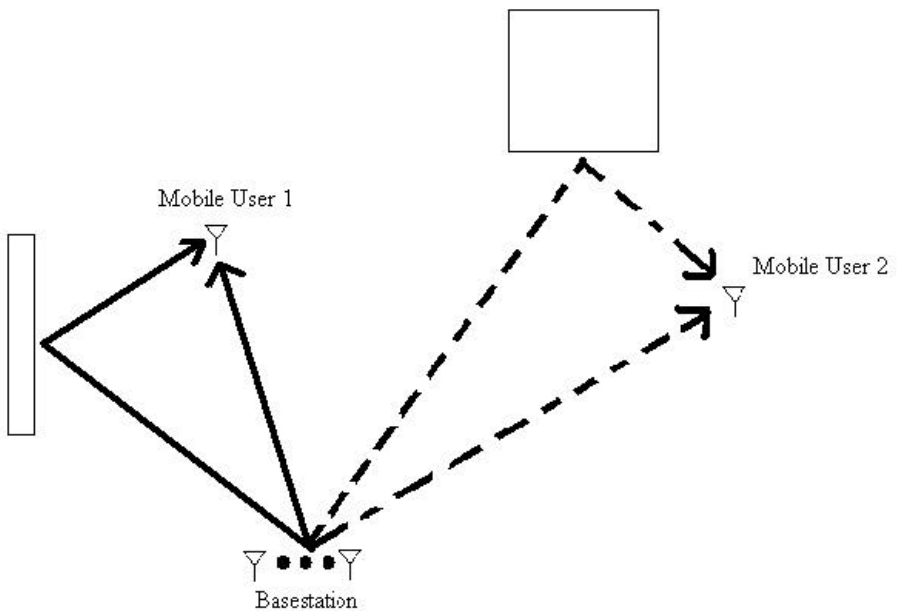

Figure 2.8 – Pseudoinverse Spatial Signature Method Illustration

The idea behind this method for transmission to mobile user 1 is that the beam is steered according to the spatial signature of user 1 (dark lines in above figure) while placing nulls according to the spatial signature of user 2 (dashed

lines in Figure 2.8). The weights for this method are calculated similarly to the PseDOA method:

$$\mathbf{X} = \begin{bmatrix} \vec{\mathbf{a}}_1 & \vec{\mathbf{a}}_2 \end{bmatrix} \tag{2.13}$$

$$\vec{\mathbf{w}}_{\mathrm{PseSS}} = \left\{ \mathrm{row}(\mathrm{pinv}\,(\mathbf{X}),1) \right\}^{\mathrm{H}} \tag{2.14}$$

Chapter 3 – Antenna Array Mutual Coupling

3.1 – BACKGROUND INFORMATION

As discussed in Chapter 2, an SDMA base station determines the incoming DOAs of the mobile users that it serves. These DOA algorithms directly use knowledge of the array steering vector to generate a spatial spectrum that intuitively gives signal power as a function of direction. A simple approach to this DOA estimation is to assume the ideal steering vector given in equation (2.1). This ideal steering vector is a function of array geometry and incident angle that does not take into account mutual coupling effects. Specifically, equation (2.1) does not take into account the scattering (or retransmission) of signal energy from each antenna element to the others. This concept is illustrated in Figure 3.1 below:

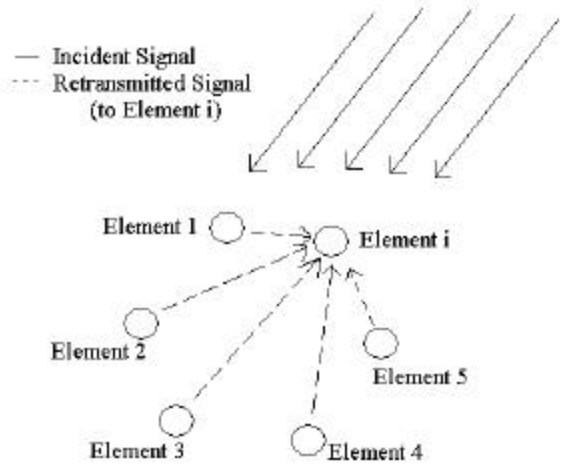

Figure 3.1 – Illustration of Mutual Antenna Array Element Coupling

It has become clear to the smart antenna community that the actual response of the antenna array can deviate significantly from the assumed and simplistic model due to electromagnetic coupling among the antenna elements as well as scattering from the antenna tower and nearby structures [10]. Most studies of mutual coupling in antenna arrays can be best characterized as array calibration methods [10-14]. These methods are generally derived using parametric antenna array models that do not directly consider the underlying electromagnetic principles. A costly alternative to these methods involves determining the actual array response using field measurements.

The same problem can also be approached from a fundamental electromagnetics perspective [15-19]. In this dissertation, this approach is applied to uniform circular arrays to demonstrate in field measurements the effects of mutual coupling compensation. In this mutual coupling compensation technique, the Method of Moments [20] (MoM) is used to compute an array response that compensates for mutual coupling. The study will then examine uplink DOA algorithm performance in field measurements for scenarios involving up to two co-channel mobile users. The study will also consider compensation in downlink beamforming scenarios and thus determine the applicability of the technique.

A distortion matrix, C, is used to encapsulate the effect of mutual coupling as well as the amplitude and phase distortions caused by imperfect antenna array elements. This matrix, which can be estimated from measurement data [10-14], is

applied to the equation of the theoretical steering vector form of equation (2.1) to develop a steering vector that takes mutual coupling and unknown sensor gains and phases into account.

$$\vec{\mathbf{a}}_C(\theta) = C(\theta)\vec{\mathbf{a}}_U(\theta) \tag{3.1}$$

In the literature, to simplify the problem, the distortion matrix is generally considered to be independent of angle. The validity of this assumption will be considered by this study. Array calibration methods attempt to estimate the matrix C algorithmically off-line [11,12], on-line [13,21], or specifically measure $\vec{\mathbf{a}}_C(\theta)$ using field measurements. However, one of the main problems in estimating the distortion matrix is that it is hard to separate coupling, gain, and phase issues from environmental factors such as tower platform effects and other scatterers located close to the array [18].

Section 3.2 discusses the specific approach used to compensate for mutual coupling effects and describes the procedure used to test and simulate the performance of this technique. Section 3.3 presents the results of this mutual coupling study, by first illustrating through field measurements the benefit of compensation in direction finding applications. Next, this section shows how this increased direction finding capability translates to increased downlink beamforming performance by considering the methods described in Chapter 2.

3.2 – METHOD OF MOMENTS APPROACH

Fundamentally, the MoM represents the induced current on an object in terms of a given basis function and enforces Maxwell's boundary conditions at a finite number of points on the object being modeled [20]. Thus, in the MoM, each antenna array element is represented as a wire of finite thickness divided up into segments. At the heart of the MoM is the calculation of a system impedance matrix Z_{QQ} giving the coupling between segment i and j in the antenna array model ($1 \leq i,j \leq Q$) where Q is the total number of wire segments in the model. The value of Q needs to be chosen to be large enough so that the obtained current solution on each of the antenna elements converge to a fixed function. In general, the higher the number of segments, the greater the validity and resolution of the answer (at the expense of greater computational effort). A detailed formulation of the modeling of an antenna array using the MoM can be found in the work of Pasala [16] and Adve [19].

The approach in this study of mutual coupling compensation is to develop an estimate for the actual array response $\vec{\mathbf{a}}_C(\theta)$, given an arbitrary geometry antenna array, via MoM code. The initial approach to MoM simulations was to develop a MoM code that specifically studied the role of mutual coupling in antenna arrays. This tool included a flag that allowed the inclusion of mutual coupling to be toggled. Thus, the transmission radiation pattern of the antenna array could be visualized for the cases when mutual coupling was present and when it was not. However, this initial approach suffers from two problems. The first is that the MoM code only included support for the most elementary basis

function and as a result had very strict convergence issues. This lack of convergence unfortunately manifested itself as large sidelobes in the radiation pattern of the antenna array, causing a great deal of confusion given the results being observed with the code. The second problem was that the code had yet to undergo any kind of validation process with real world measurements.

To address these issues, the MoM code used in this study is NEC (Numerical Electromagnetics Code), which was originally developed at the Lawrence Livermore Laboratory [22] to perform MoM analysis to model the interaction between electromagnetic fields and wire segments. A wire segment model of an arbitrary geometry antenna array can be specified in an input file to NEC. NEC results are well accepted in the literature and versions of NEC are freely distributed on the World Wide Web.

A 7 element circular array was used in simulations and measurements in this study. The simulated antenna elements are each coaxial dipole elements containing four collinear $\lambda/2$ dipole antennas (illustrated in Figure 3.2) with an operating frequency of 1.88 GHz. Each of the dipole elements is represented as a wire divided up into segments for MoM analysis. Lump loading is used to model the isolation between the dipole antennas and the load impedance of the array elements.

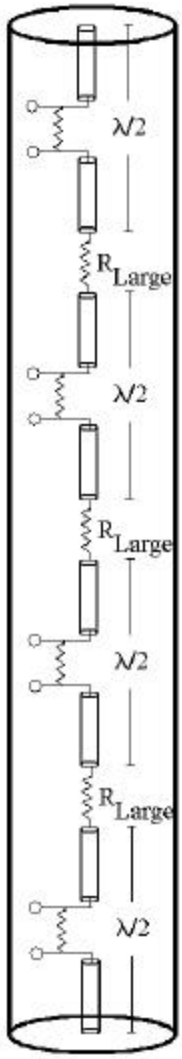

Figure 3.2 – Collinear Dipole Antenna Array Element

Two types of mutual coupling compensation using MoM were considered in this chapter. In the first type of compensation, MoM calculations were used to determine the true steering vectors in the azimuth plane perpendicular to the axis of the array elements. The complete array manifold is then used when performing uplink DOA analysis. In the second compensation technique, based upon [10-

14,18], the steering vectors at only a few angles are computed, and equation (3.1) is solved for the distortion matrix (assuming angular independence) using pseudoinverse of matrix A_{theo}:

$$C = A_{true} A_{theo}^{H} (A_{theo} A_{theo}^{H})^{-1} \tag{3.2}$$

where the columns of A_{true} and A_{theo} are the MoM determined (compensated) steering vectors and the theoretical (uncompensated) steering vectors respectively, corresponding to a particular set of angles. This distortion matrix is then applied using equation (3.1) to determine compensated steering vectors. Field measurement comparsion of the results of these two types of compensation allow the assumption of angular independence of the distortion matrix to be examined.

Measurement data was collected using the smart antenna testbed at the University of Texas at Austin. It is this hardware system that was reported in the past [23] to produce a "rebounce" effect that seemed indicative of strong mutual coupling effects. However, this claim was never specifically studied until addressed by this research. The smart antenna testbed was mounted in a van supplied by the Electrical Engineering Research Laboratory at Pickle Research Campus. This van has a deployable antenna support structure that was used to raise the mounted UCA that corresponds to the same array simulated in NEC.

Data collection was performed outdoors on an open field in the Pickle Research Campus at the University of Texas at Austin. The antenna array was deployed approximately 20 meters off the ground at the center of the site chosen to minimize the amount of signal multipath. There were two signal generators

used to represent mobile users transmitting to the smart antenna base station. The first signal generator was held stationary. The second signal generator was moved to five distinct angles at approximately the same distance and the same transmission power as the first signal generator. Data was then collected using the smart antenna testbed and uplink spatial spectra were considered for each generator transmitting individually and both generators transmitting together. The position of each of the signal generator locations is listed in Table 3.1. These positions were measured using the average of the angles indicated using the compensated and uncompensated uplink spatial spectra of the signal generator transmitting alone.

Position	Angular Position
Stationary User	29°
Position 1	42°
Position 2	48°
Position 3	65°
Position 4	78°
Position 5	97°

Table 3.1 – Signal Generator Positions

3.3 – RESULTS

In Section 3.3.1, the effects of mutual coupling will be directly demonstrated through consideration of the radiation pattern of a single antenna array element. Section 3.3.2 will quantify the difference between the simulated and theoretical array response vectors. Sections 3.3.3 shows through field measurements how uplink DOA algorithm performance is improved through

mutual coupling compensation. Section 3.3.4 shows simulations illustrating how this improved direction finding capability translates to downlink beamforming algorithm performance.

3.3.1 – Active Element Pattern

Figure 3.3 shows the effect of mutual coupling on the azimuth radiation pattern (i.e. in the plane perpendicular to the axis of the antenna array elements) of a single antenna array element. This graph shows the radiation pattern of a single antenna array element in the presence of the other elements in the array. Without mutual coupling, this pattern will be omni-directional for all antenna array elements in the array. For the other elements of the circular array, the pattern will be a rotated version of the pattern shown in Figure 3.3(B). Further consideration of the pattern shown in Figure 3.3(B) shows that the directions in which the pattern is attenuated corresponds to the locations of the other array elements. Study of similar patterns in other array geometries suggest that this qualitative result can be applied to arbitrary geometry antenna arrays. This is an intuitive result since mutual coupling results from the scattering of signal energy by the other elements in the array.

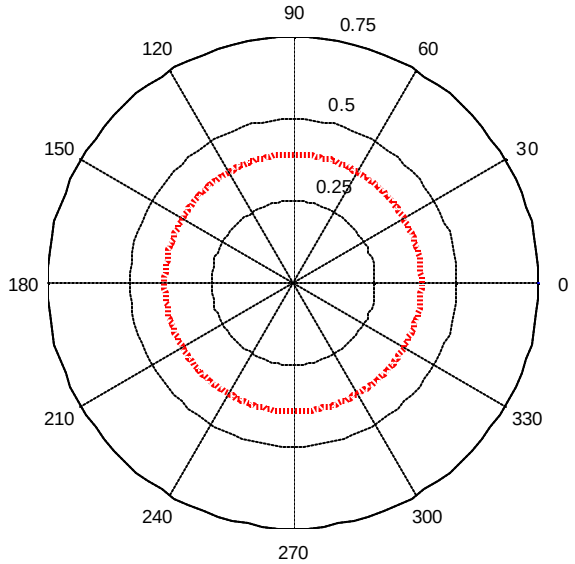

(A)

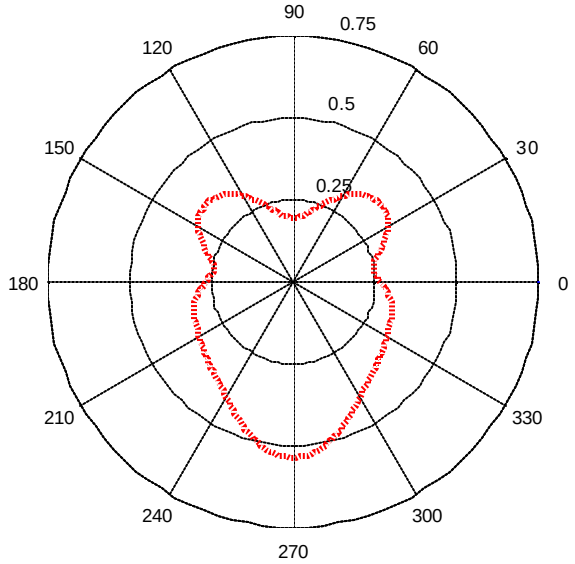

(B)

Figure 3.3 – Active Element Pattern – (A) Without Mutual Coupling Effects and (B) With Mutual Coupling Effects

3.3.2 – Relative Angle Change

Next, consider the difference between the ideal (from equation (2.1)) and compensated (from NEC simulations) array steering vectors. Relative angle change (RAC) measures the difference between theoretical and compensated array vectors. For a compensated steering vector, a_C, and an uncompensated steering vector, a_U, this metric can be written as:

$$\mathrm{RAC}(\%) = 100 \times \sqrt{1 - \left| \frac{\mathbf{a}_C^* \cdot \mathbf{a}_U}{\|\mathbf{a}_C\| \|\mathbf{a}_U\|} \right|^2} \tag{3.3}$$

This metric has been used in simulations and measurements [9,24] to provide a measure of the difference between spatial signatures. It is used in this study to quantify the difference between compensated and uncompensated steering vectors, and is shown in Figure 3.4. This graph shows that there is an appreciable difference between the compensated and uncompensated steering vectors and further shows that the magnitude of this difference is a function of angle. Also note that the number of local maxima and the number of local minima is the same as the number of antenna array elements. The angles of the local minima correspond to the angles of the elements in the uniform circular array. This implies that compensation will have less effect at DOAs matching the locations of array elements. It also implies that the effect of scattering from one element to another is minimized when the DOA matches the array element angle.

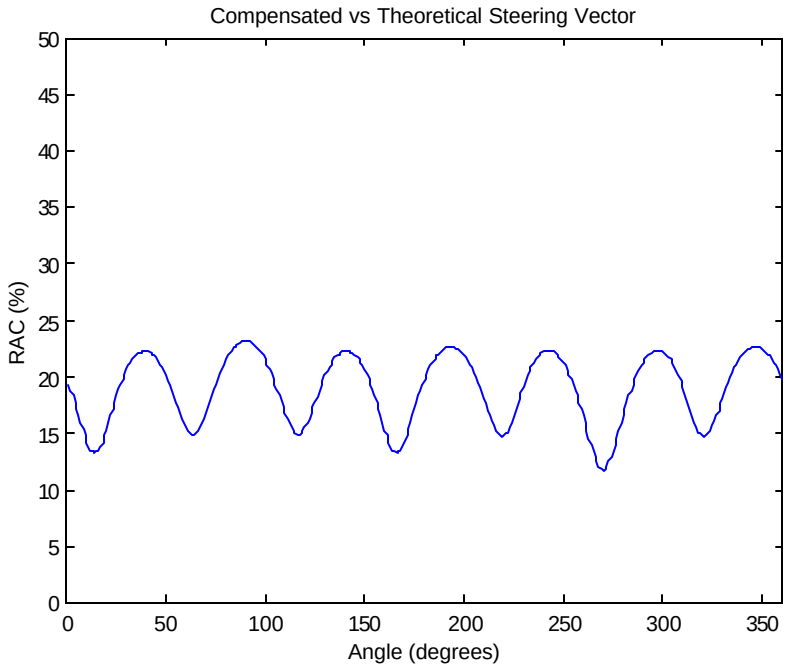

Figure 3.4 – Compensated vs. Theoretical Steering Vector RAC

3.3.3 – Uplink Direction of Arrival Algorithms

Figure 3.5 shows the spatial spectra generated using uncompensated and compensated steering vectors for measurement data due to a single mobile user (referred to as "Stationary User" in Table 3.1). In this figure, we consider the application of the full array manifold calculated using the MoM. Figure 3.5(A) contains Bartlett DOA algorithm output and Figure 3.5(B) contains the MUSIC spatial spectrum. These spatial spectra show that while the effect on the detected DOA is minimal for both uncompensated and compensated results, sidelobe levels are significantly reduced through use of mutual coupling compensation. Specifically, Figure 3.5(B) shows the typical (for all tested cases) sidelobe

reduction of approximately 3 dB. While compensation has little effect on the main lobe of the Bartlett spatial spectra in Figure 3.5(A), the effect is more pronounced on the MUSIC spatial spectra in Figure 3.5(B).

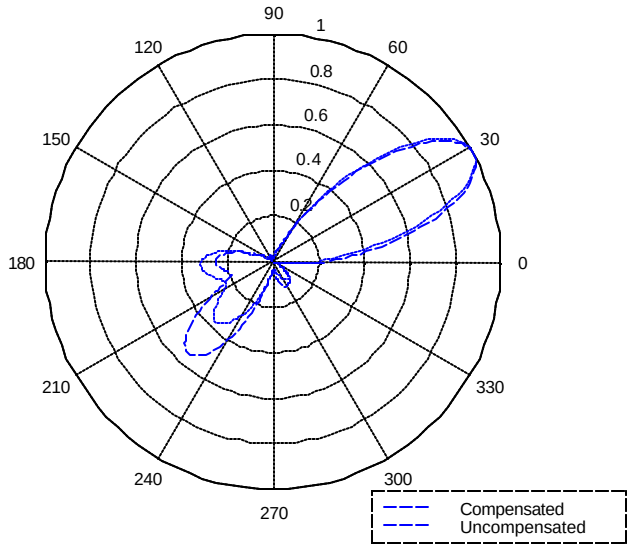

(A)

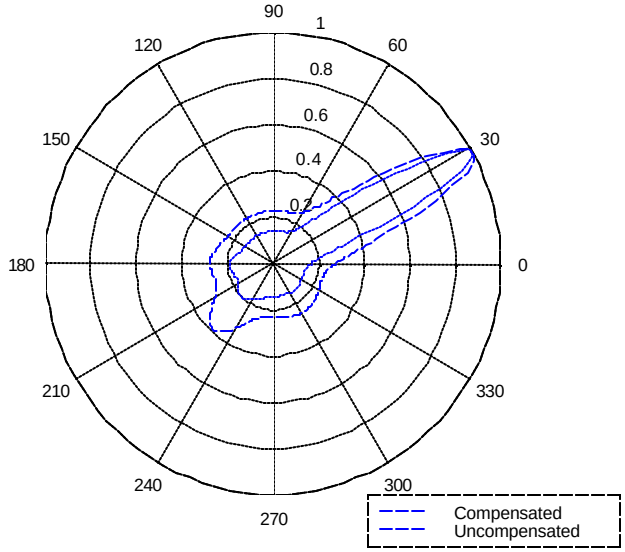

(B)

Figure 3.5 – Experimental Data Stationary User Spatial Spectra – (A) Bartlett DOA Algorithm (B) MUSIC DOA Algorithm

Figure 3.6 shows the same results as Figure 3.5 for a different mobile user. Specifically, it represents the Bartlett and MUSIC DOA algorithm output given the full NEC calculated array manifold for a single mobile user (referred to as "Position 1" in Table 3.1). Again, this figure shows that mutual coupling compensation has a greater effect on the main lobe of MUSIC spatial spectrum output shown in Figure 3.6(B) compared with the effect on the main lobe of the Bartlett spatial spectrum shown in Figure 3.6(A). Both spatial spectra in Figure 3.6 show a reduction in unwanted sidelobe levels. The increased direction finding capabilities of the MUSIC method is realized through greater consideration of the underlying array model and is thus more vulnerable to model errors.

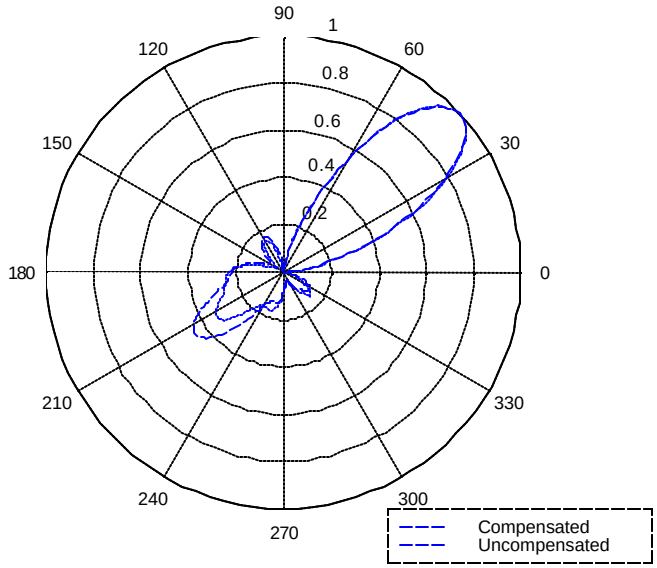

(A)

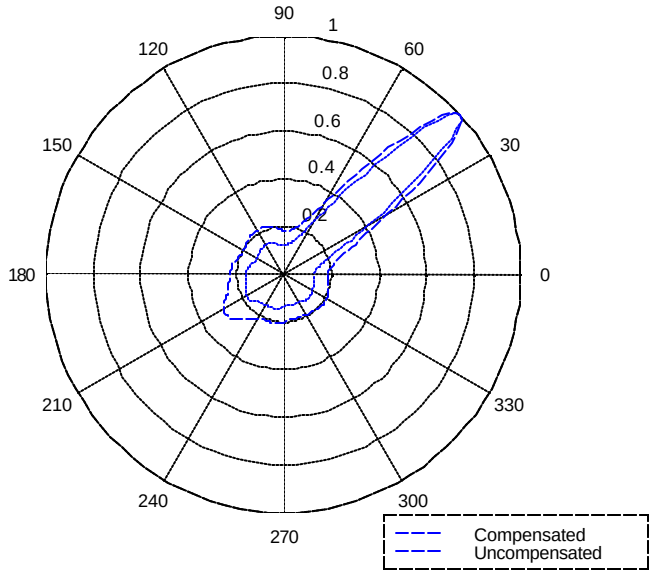

(B)

Figure 3.6 – Experimental Data Mobile Position 1 Spatial Spectra - (A) Bartlett DOA Algorithm (B) MUSIC DOA Algorithm

Figure 3.7 shows the uncompensated and compensated MUSIC spatial spectra for a situation in which there was two mobile users ("Stationary User" and "Position 5" in Table 3.1) transmitting simultaneously. This figure again illustrates the previous results of significant sidelobe reduction along with sharpening of the lobes corresponding to mobile users. Specifically, note that the DOA of the stationary user is made much more prominent compared to the sidelobes due to compensation. These sidelobes could be mistaken for either another mobile user or multipath signal energy – either of which has adverse consequences for downlink beamforming methods such as the PseDOA method. In general for all tested cases (single and multiple user scenarios), mutual coupling compensation increased lobes in the spatial spectra corresponding to desired users' DOAs and decreased all other sidelobes.

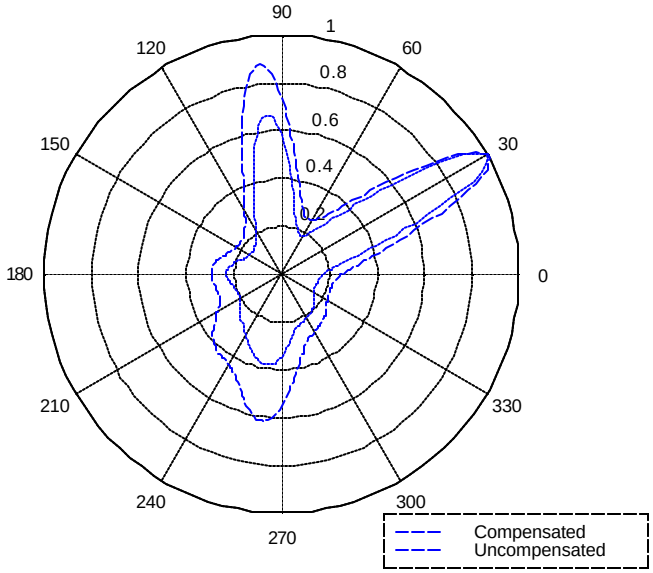

Figure 3.7 – Experimental Data Multiuser MUSIC Spatial Spectra – Stationary User & Mobile Position 5

Figure 3.8 shows the effect of assuming the distortion matrix is independent of angle using the same spatial spectrum considered in Figure 3.5(B). For all of the results in this study not including those of Figure 3.8, the compensation technique involved using the entire array manifold computed through NEC. In Figure 3.8, this technique is referred to as the "Look-up Table" approach. The other tested compensation technique is to compute the distortion matrix (assuming angular independence) using equation (3.2) with a relatively small number (12) of MoM-generated and theoretical steering vectors. The angular independence of the C matrix is a generally a good assumption. Results show that making use of the assumption yields a performance increase over theoretical steering vector use. The very slight performance increase of using the MoM-generated manifold instead of the C-matrix calculation comes at the cost of requiring more storage.

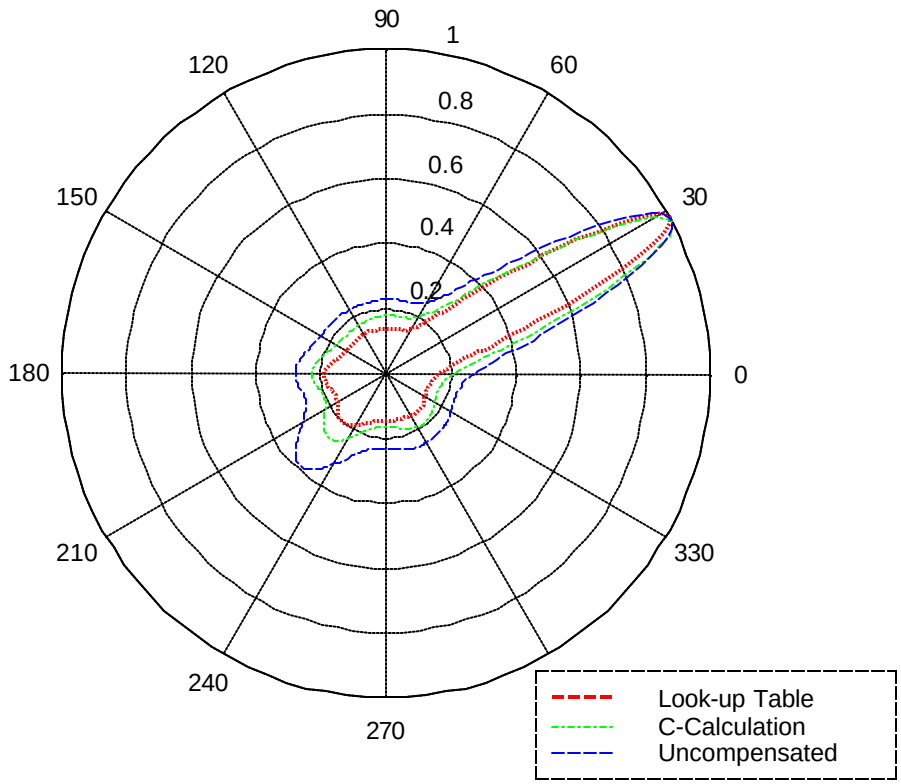

Figure 3.8 – Compensation Technique Effect – Stationary User Spatial Spectra

3.3.4 – Downlink Signal to Interference Ratio

The MoM model for the antenna array was used to determine the effect that mutual coupling compensation has on downlink beamforming. The uplink spatial spectra from measurement data for all of the tested cases were used to compute downlink beamforming weights for scenarios involving the Stationary User (User 1) and the mobile user at each of 5 different tested positions (User 2). Figure 3.9 shows the resulting simulated radiation pattern from using each of the four downlink beamforming methods described in Chapter 2.6. Figure 3.9(A) shows the downlink radiation patterns for the Stationary User and Figure 3.9(B)

shows the patterns for the mobile user at Position 4. This figure shows, for the DOA based methods DomDOA and PseDOA, the effects of using compensated and uncompensated steering vectors. As seen in the top pattern of Figures 3.9(A) and (B), use of compensated steering vectors does not significantly improve the performance of the DomDOA method. Specifically, both of these patterns show that the main lobes of the uncompensated and compensated DomDOA method are practically the same. Furthermore, both patterns show similar performance to that of the SS method. However, the bottom pattern of Figures 3.9(A) and (B) shows that there is significant improvement in the performance of PseDOA method when using compensated steering vectors. These patterns clearly show an improved main lobe when using the compensated PseDOA method instead of the uncompensated PseDOA method. In addition, these patterns show that use of compensation allows the PseDOA method to work comparably to the PseSS method.

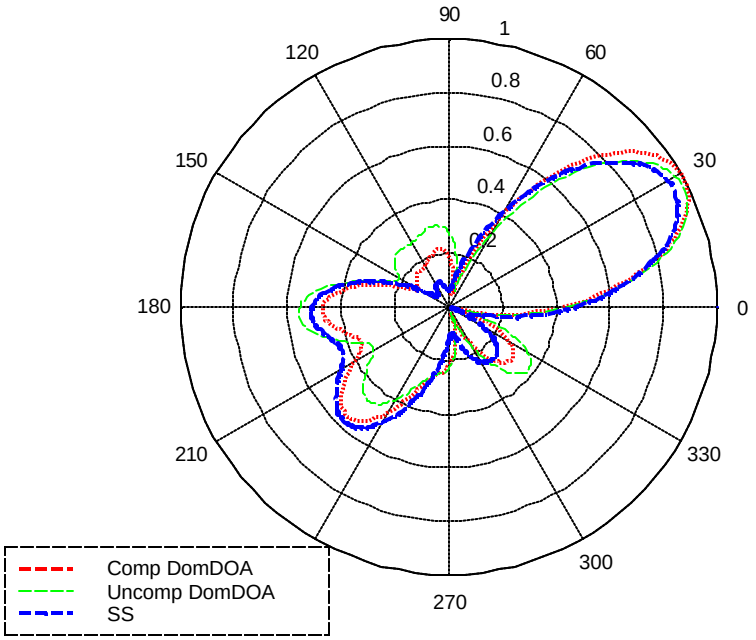
90
1
120
60
0.8
0.6
150
30
0.4
0.2
180
0
210
330
300
270
Comp DomDOA
Uncomp DomDOA
SS

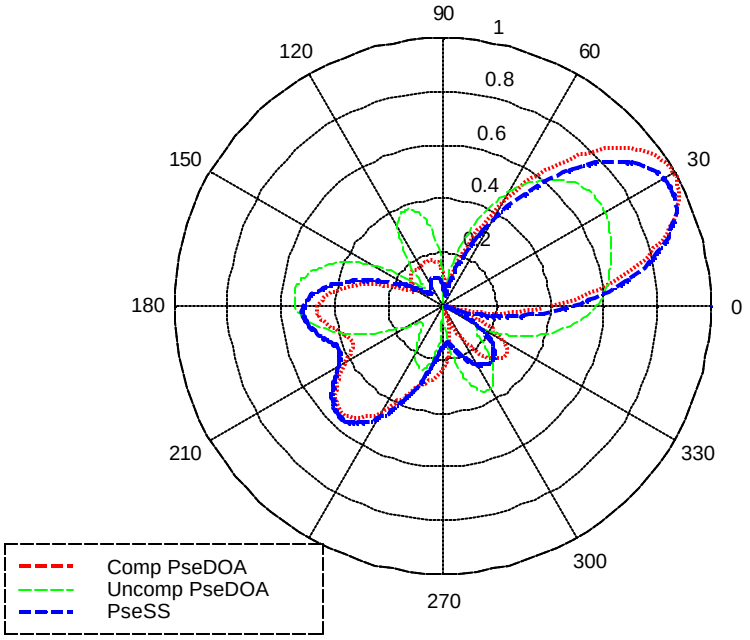
90
1
120
60
0.8
0.6
150
30
0.4
0.2
180
0
210
330
300
270
Comp PseDOA
Uncomp PseDOA
PseSS

(A)

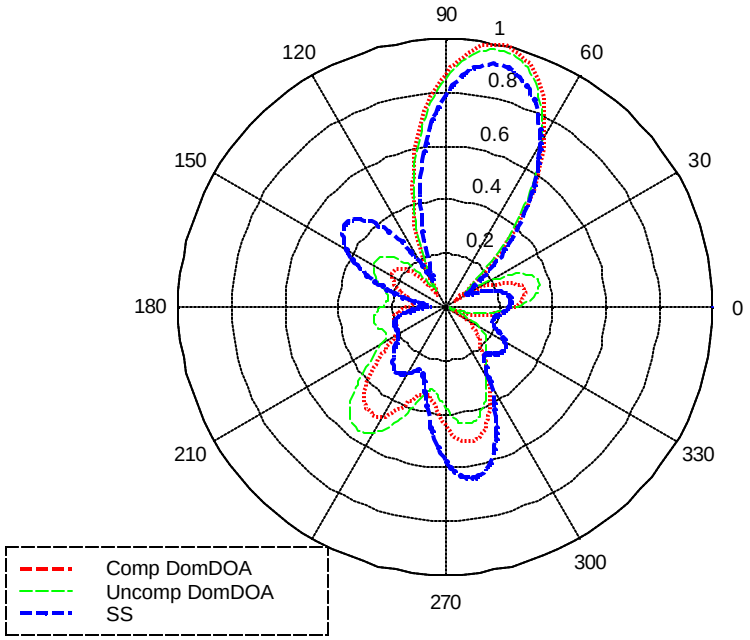

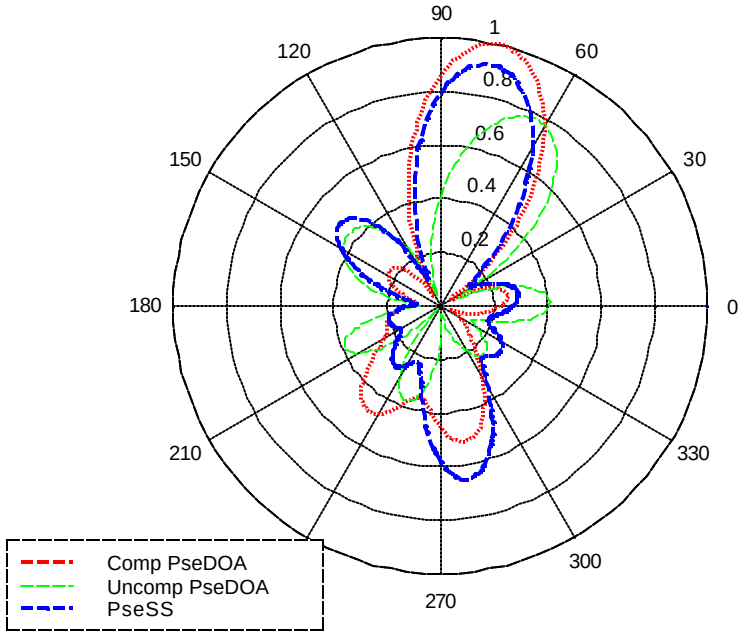

(B)

Figure 3.9 – Downlink Beamforming Radiation Patterns for (A) Stationary User and (B) User at Position 4

Trial	User 1 Benefit over Uncomp PseDOA Method (dB)	User 1 Benefit over PseSS Method (dB)	User 2 Benefit over Uncomp PseDOA Method (dB)	User 2 Benefit over PseSS Method (dB)
1	0.93	0.17	-0.82	0.76
2	4.48	0.22	4.71	1.08
3	2.73	0.46	0.65	0.45
4	3.06	0.29	3.60	0.71
5	3.33	-0.12	25.67	-0.74

Table 3.2 – Compensated PseDOA Method Improvement between Stationary User (User 1) and User 2 (at each of 5 tested positions)

To quantify the results illustrated by Figure 3.9, Table 3.2 shows the gain in signal power for each mobile user that is realized through use of the compensated PseDOA method over the uncompensated PseDOA method and the PseSS method. Signal power is determined by the value of the radiation plot at the known DOA of the desired user. As seen in this table, the use of compensated steering vectors instead of uncompensated vectors in the PseDOA method (Column 1 for User 1 and Column 3 for User 2) nearly always significantly improves transmitted signal power. Furthermore, this table shows that use of compensated steering vectors allows the PseDOA method to work just as well as the PseSS method (Column 2 for User 1 and Column 4 for User 2), which is normally not true [8].

Table 3.3 shows the improvement in SIR for the two mobile users using the compensated PseDOA method over the uncompensated PseDOA method. In this table, signal power is determined as before and interference power for one mobile user is determined by the value at that user's DOA on the other user's

radiation plot. This table shows that use of compensated steering vectors instead of uncompensated vectors often significantly improves SIR (Column 1 versus Column 2 for User 1 and Column 3 versus Column 4 for User 2). The results in this table also show that SIR performance is more stable as a function of user position when using compensated steering vectors (Column 1 for User 1 and Column 3 for User 2). This result has beneficial implications for the minimization of cellular call dropping because more stable SIR performance will reduce the number of unnecessary handoffs from one base station to another.

Trial	User 1 Comp SIR (dB)	User 1 Uncomp SIR (dB)	User 2 Comp SIR (dB)	User 2 Uncomp SIR (dB)
1	19.68	23.70	22.39	25.16
2	21.59	14.45	23.19	23.62
3	22.59	26.57	23.38	22.86
4	21.38	16.36	23.93	12.36
5	23.98	14.15	22.51	-10.48
Mean	21.84	19.05	23.08	14.70
Variance	2.02	26.12	0.33	179.01

Table 3.3 – PseDOA Method SIR Improvement between Uncompensated and Compensated Calculations

3.4 - SUMMARY

In this chapter, the benefit of mutual coupling compensation was examined during uplink DOA estimation and during downlink beamforming. Results from field measurements allow several comments regarding mutual coupling compensation. It has been shown through the use of MoM calculations that steering vectors taking into account mutual coupling differ significantly, in

terms of relative angle change, from theoretical steering vectors. By using more accurate steering vectors, we observed the expected performance improvement. The performance improvement in terms of direction finding comes from reduced sidelobe levels, which allows for easier distinction of signal sources. The DOA performance increase also translates into improved downlink SIR performance, allowing a DOA-based downlink beamforming method (Pseudoinverse DOA method) to work comparably to spatial signature based methods.

While the smart antenna community has recognized the existence of mutual coupling, there has been little work considering the quantitative effects of coupling over a wide range of communications topics. The contribution of this dissertation is the demonstration, through field measurements, of the benefits of antenna array moment-method mutual coupling compensation. The novel aspect of this research is the demonstration of the implications of mutual coupling compensation at a higher level in communications system performance. Specifically, the role of mutual coupling in direction-finding and downlink beamforming was studied in depth. The work is also significant because it showed how off-line calculations using basic electromagnetic computations could lead to significant improvements in smart antenna system performance.

Chapter 4 – Vector Channel Propagation

4.1 – BACKGROUND INFORMATION

Characterizing the performance of SDMA systems is a relatively new area of study. There are many more factors that can be examined instead of strictly considering bit error rate as a function of signal to noise ratio. Study of nearly all of these additional system performance parameters benefits from consideration of the underlying electromagnetics. In particular, characterization of the vector channel encountered by SDMA systems is of great importance.

Winters [25] identifies three main limiting factors to communications system performance. These are:

- Multipath fading
- Delay spread
- Co-channel interference

Multipath fading can easily be understood using the computational ray tracing approach of this study. A receiver in a particular environment will be receiving rays that are launched from the transmitter. These rays take different paths when traveling from transmitter to receiver and will thus have different amplitudes and phases. The principle of superposition states that the total field at the receiver will be the sum the contributions of each of the individual rays. At the receiver, the rays will destructively and constructively interfere with each other. Over time the level of this interference will fluctuate rapidly since it is extremely sensitive to position, orientation, and environment. Thus, the total

power reaching the receiver will experience large fluctuations that are referred to as multipath fading. In conventional systems, an increase in base station transmit power is generally needed when combating multipath fading while maintaining a constant bit error rate (BER).

Delay quantities are also closely related to multipath fading. Since signals propagating from transmitter to receiver take different paths to reach the receiver, it makes sense that at any given instant the receiver is receiving "current" information as well as an "echo" of past information that took a longer propagation path to reach the receiver. The power distribution as a function of propagation time from transmitter to receiver is referred to as a power-delay profile and is characterized by the quantity delay spread. According to Winters [25], if the mean delay spread exceeds 10% of the symbol duration, there will be significant levels of intersymbol interference (ISI) that decreases the maximum sustainable data rate. Combating ISI generally involves the use of complex coding or channel equalization techniques. In addition to studying power-delay profiles, it is also insightful to study power-angle profiles. Knowledge of signal power versus direction is relevant because of the directional properties of SDMA systems. Thus, there are implications not only in the geometrical design of the antenna arrays themselves, but also implications for both uplink direction finding and downlink beamforming algorithms.

Co-channel interference (CCI) refers to the signal energy received by a particular mobile user or base station from all of the other mobile users and base stations in the system using the same channel. Since the signal of one mobile user

contributes to the interference of all the other users, simply increasing transmit power is not a feasible solution. The amount of co-channel interference that a communications system can tolerate is closely linked to the maximum capacity of the system. Combating CCI involves decreasing the coverage area of cellular base station sites. This is not an attractive solution, however, since building many base stations is expensive.

The research of Winters [25] has shown that the use of SDMA systems can combat all three of these fundamental limitations to communication system performance. In this chapter, small-scale (i.e. on the order of wavelengths of mobile displacement) vector channel quantities will be studied. Section 4.2 will motivate and discuss the vector channel quantities studied in this dissertation. The ray tracing approach used to study the vector channel quantities of interest is discussed in Section 4.3. Section 4.4 will present results of the small-scale vector channel study in both generic environments and in downtown Austin. Section 4.5 will then introduce a novel approach to the prediction of spatial signatures and demonstrate the potential of this technique.

4.2 – VECTOR CHANNEL CHARACTERISTICS

4.2.1 – Spatial Signature Variation

Spatial signature variation provides a measure of the level of change of the spatial signature over time. Observing spatial signature variation is valuable in terms of the discussion in Section 4.1 because it specifically shows how multipath fading effects and the changing angular position of the mobile user with respect to the base station influences SDMA system performance. Spatial signature

variation is divided into two components, relative angle change and relative amplitude change. These are both relative stability measures between any two given spatial signatures. The relative amplitude change and relative angle change between two spatial signatures $\vec{\mathbf{a}}_i$ and $\vec{\mathbf{a}}_j$ are:

$$\text{Relative Amplitude Change (dB)} = 20\log_{10}\frac{\left\|\vec{\mathbf{a}}_j\right\|}{\left\|\vec{\mathbf{a}}_i\right\|} \tag{4.1}$$

$$\text{Relative Angle Change (\%)} = 100\times\sqrt{1-\left|\frac{\vec{\mathbf{a}}_i^{*}\cdot\vec{\mathbf{a}}_j}{\left\|\vec{\mathbf{a}}_i\right\|\left\|\vec{\mathbf{a}}_j\right\|}\right|^2} \tag{4.2}$$

Past studies in the literature have considered both of these variation metrics [24, 26]. In this work, focus will be placed on relative angle change (RAC) because of its similarity to spatial signature correlation [23] and because of the study of Arredondo and Dandekar linking relative angle change to loss in signal to interference ratio [27].

Spatial signature variation information can be used to examine two separate facets of SDMA system performance. If i and j are always chosen to be adjacent uplink spatial signatures, variation information can be used to examine how dynamic spatial signatures are over small displacements. This information can be used to provide a measure of spatial signature stability when the mobile user is stationary and all motion is relatively small. If i is held constant and j is allowed to increase relative to i, variation information can be used to provide a measure of how long uplink spatial signature estimates are valid for a mobile user. It can then further be used to determine how often uplink spatial signature estimates need to be obtained in order to adequately choose downlink beamforming weights.

4.2.2 – Power-Delay / Power-Angle Profile

Power-delay profiles and Power-angle profiles are easily simulated using ray tracing techniques. The simulation reports the total distance that each ray travels from transmitter to receiver and the angle at which it arrives. While there is no information-bearing signal transmitted in the ray tracing simulations to produce intersymbol interference (ISI), typical reference system values can be used to place the simulated delay profiles into perspective. Delay is measured relative to the first ray to reach the receiver from the transmitter and the relative power of each ray is given with reference to the strongest received ray.

Power-angle profiles are significant in terms of the directional capabilities of SDMA systems. In this study, angle profiles are studied in terms of angular deviation from the direction of the dominant signal component. Power-angle profiles can be used to gain insight into the array geometry needed to effectively resolve multipath signal components in a particular environment. By the principle of reciprocity, this information can also be used to consider array geometries needed for synthesis of beam patterns during downlink beamforming.

Delay-profiles and angle-profiles are for a given reference element in the antenna array. The array dimension is small enough compared to the scale of the environment that the ray solutions do not differ significantly from one element to the next. Although small differences in ray phase received at each element makes array signal processing possible, this is best studied by spatial signature variation metrics in 4.2.1.

4.2.3 – Signal to Interference Ratio

Signal to Interference Ratio (SIR) information can be used to describe the amount of CCI that is present in an SDMA downlink channel. Consider scenarios measuring SIR for two mobile users: the signal from the base station array to one mobile user is the interference of the other mobile user and vice versa. SIR depends upon the downlink beamforming methods described in Chapter 2. The simulation of SIR in this study was strictly in terms of signal and interference power rather than through consideration of a specific modulation scheme for bit error rate calculations.

4.3 – ELECTROMAGNETIC RAY TRACING APPROACH

4.3.1 – Background

Using electromagnetic ray tracing (ERT) to study vector channel propagation allows for a level of accuracy, control, and reproducibility that cannot be matched by conventional measurement studies. Simulation parameters can be tightly controlled and varied individually to isolate their effect upon system performance. Ray tracing allows measurements to be made at a resolution much higher than what can reliably be attained with field measurements. Also, the ray tracing technology used to simulate channel propagation is portable to any communications environment (indoor, outdoor, urban, rural, etc) by simply changing the environment model used by the ray tracing system. Small-scale issues like fast fading can be observed in addition to large-scale power distribution information.

There are several important past ray tracing papers that are closely related to the work conducted in this study. Erceg [28], at AT&T Bell Laboratories and Lucent Technologies, developed a ray tracing system called the Wireless System Engineering (WiSE) tool for indoor and outdoor wireless communications applications. This system was used to simulate urban scenarios in Manhattan and Boston at 900 MHz and 2 GHz. Greenstein [29], also at AT&T Bell Laboratories, simulated Manhattan prior to the Erceg study. Lawton [30] and Catedra [31] also conducted urban environment measurement studies to complement their own ray tracing systems. They primarily differ from this work in that they exclusively consider traditional, single antenna communications systems. In the thesis [9] leading up to this work, the application of ray tracing to the study of communications systems making use of antenna arrays was first demonstrated using the CPATCH ray tracing system [32-34].

4.3.2 – System Parameters

In general, ERT, like any other experimental tool, has relative strengths and weaknesses that can only be understood with at least a rudimentary understanding of how these systems work. The first piece of information needed by a ray tracing system is a model that describes the environment to be studied. These models use facets: simple polygons (usually triangles) assigned position and orientation information. A simple plane can be described with two facets, but urban environments and complex structures must be described in terms of tens of thousands of facets, if not more. In addition, each facet must be assigned properties that describe how it will respond to incident electromagnetic radiation.

Many electromagnetic simulations make use of perfect electric conductors (PEC) for the facets used in the model. PEC materials reflect all incident radiation and do not model field strength loss by reflection. For more sophistication, material properties can be specified to better model the materials reaction to signal reflections. However, these material properties are difficult to determine without site-specific measurements.

For the purposes of this work, distinctions were only made between ground materials and building material. Based upon the information in Lytle [35] and Kavak [36] a relative permittivity of $\varepsilon_r = 2$ was used to model the asphalt ground surface of urban environments. Based upon the work of Lawton [30], a relative permittivity of $\varepsilon_r = 9$ was used to model the building walls. The latter permittivity information has no clear accepted value in the literature, with values ranging from 4 to 15 being reported [30]. This is because the measurement of this value is highly dependent upon weather conditions and building materials. Thus many ERT studies of this type measure this quantity empirically for the particular environment under study.

The lack of accurate, site-specific models is considered one of the greatest weaknesses of using ERT for communications channel study. The other main weakness, computational effort, is no longer considered as significant with continually increasing computer processing speeds. Concerning the site-specific modeling problem, studies must either be conducted with generic models to view typical system behavior or must be conducted with complex site-specific models that are often difficult to develop.

The ray mechanisms considered by the ray tracing system refer to the electromagnetic principles considered by the system as the rays propagate through the model. These principles include reflection and diffraction. A ray propagating from transmitter to receiver through a single reflection or diffraction is considered to experience a first order effect. ERT systems must all have specified the maximum order that they will model. For example, considering third order effects (reflection-reflection-reflection, reflection-reflection-diffraction, …, diffraction-diffraction-diffraction) carry with it a tremendous computational cost that is orders of magnitude greater than considering first order effects alone. However, there is a diminishing return as increasingly higher order effects are modeled since signal energy is lost at each reflection or diffraction. Thus, in this work, only second order ray effects are considered. In summary, all of the ray tracing mechanisms considered in this study are given in Table 4.1.

Direct Ray	
Reflected Ray	Diffracted Ray
Reflected-Diffracted Ray	Diffracted-Reflected Ray
Double Reflected Ray	Double Diffracted Ray

Table 4.1 – FASANT Ray Mechanisms

The computational cost of even the simplest urban scenario can be considerable, sometimes requiring hours or days of CPU-intensive calculations. The time taken for a simulation relies upon the maximum order effects considered, the number of facets, and the number of field observation points. There has been a great deal of research into developing efficient ray tracing

systems not only for communications applications, but also for radar, virtual reality, and scientific visualization applications.

There are two main types of ERT algorithms [31]: Direct and Indirect algorithms. In Direct algorithms rays are launched from the transmitter with some pre-specified density. The computer then maintains the path of each ray in the model as it undergoes whatever effects are considered by the system. Some rays will then be "caught" by the receiver and the contribution of that ray to the total field at the receiver will be computed. Some of the more common Direct methods are referred to as Shooting and Bouncing Ray (SBR) techniques or Pincushion methods. It is conceivable using this method that CPU time could go to waste since it is possible that few, if any, of the rays launched from the transmitter actually reach the receiver. Indirect algorithms attempt to address the problem by only considering rays that connect the receiver and transmitter with the ray mechanisms active in the system. However, determining which rays connect receiver and transmitter in a complex model file is itself a very computationally intensive task.

The M.S. thesis by Dandekar [9] gives preliminary results in vector channel propagation study using ray tracing. This thesis focused on studying various vector channel propagation characteristics for various mobile user trajectories through generic cellular environments. The thesis made use of the ray tracing system, CPATCH [32]. However since this system made use of only reflection ray mechanisms, there was a tendency in urban models for regions to be highly shadowed (i.e. receive no rays). To alleviate this problem required the use

of a ray tracing system that takes into account diffraction ray mechanisms along with reflection ray mechanisms. For this reason, the FASANT [31] ray tracing system developed at the Universidad de Cantabria in Spain by Catedra was used.

4.3.3 – Hybrid Simulation Tool

ERT is an appropriate technique for modeling the effect of the mobile environment on traveling electromagnetic radiation. However, to model the effects of local scattering close to the base station as well as electromagnetic interactions between the base station array elements themselves requires use of the CEM technique MoM described in Chapter 3. Developing hybrid computational tools to consider local effects through MoM and the effect of environment through ERT is a current area of electromagnetics research [37]. All FASANT ERT simulations considered in this study model the effects of mutual coupling through the use of MoM. Specifically, the moment method is used to generate the radiation patterns of the base station antenna array elements with coupling effects included, and this radiation pattern is used when modeling the environment with ERT.

4.3.4 – Simulated Scenarios

Table 4.2 summarizes the scenarios simulated in this chapter of the dissertation. A description of each of these scenarios along with illustrations indicating the view from the base station and mobile user trajectory are included in the following subsections. These models all represent generic urban situations with multiple mobile users. The simulations were all run at 1.8 GHz on models meant to study a base station cell radius of approximately 500 meters. These

simulations were all run at relatively high spatial resolution (i.e. on the order of fractions of a wavelength of mobile user displacement) for the purpose of observing small-scale channel effects during individual trajectories through the environment. Large-scale effects and statistical characterizations of the urban vector channel for the purpose of aiding in system planning issues is the topic of Chapter 5. Linear arrays were used in all but the Austin simulation to allow qualitative comparisons to be made to the measurement study using the smart antenna testbed at the University of Texas at Austin described in [8] and [24]. A circular array was used in the simulation of downtown Austin so that results could similarly be compared to testbed measurements described in [23].

Scenario Name	Array	User	Situation
Case 1	Linear	1	Line of Sight
		2	Line of Sight
Case 2	Linear	1	Line of Sight w/ Dominant Multipath
		2	Line of Sight w/ Dominant Multipath
Case 3	Linear	1	Non Line of Sight
		2	Line of Sight w/ Local Scatterer
Alley	Linear	1	Non Line of Sight
		2	Non Line of Sight
Sixth Street	Circular	1	Non Line of Sight

Table 4.2 – Simulated Scenarios

4.3.4.1 – Case 1

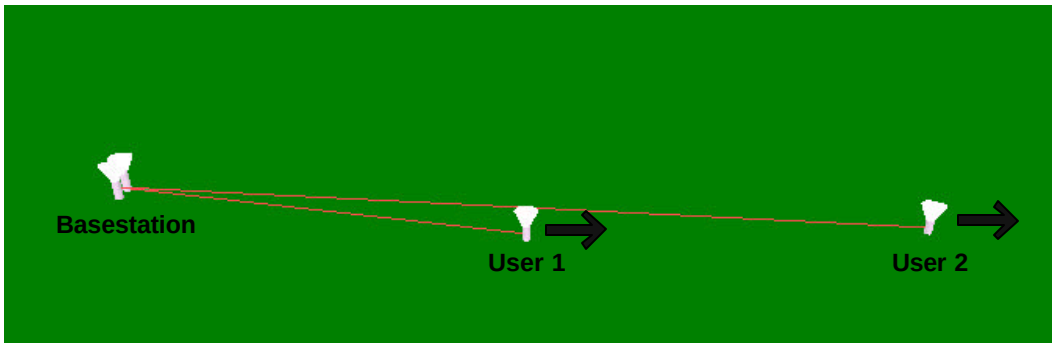

(A)

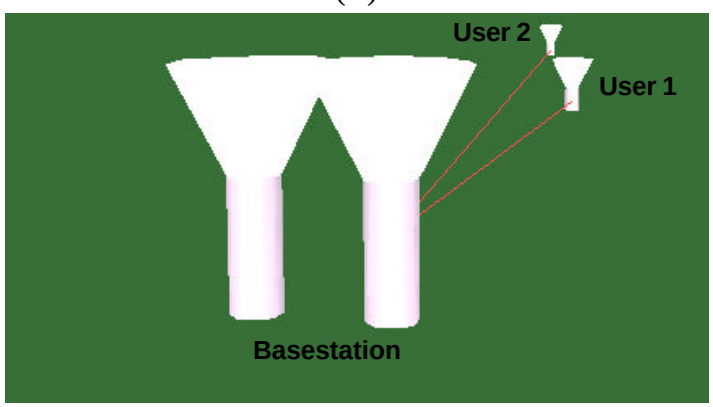

(B)

Figure 4.1 – Case 1 Illustration (A) Side View (B) View from Base station

In this situation, the mobile users are both in the line of sight (LOS) of the base station and move directly away from the array. Other than a ground plane corresponding to an asphalt surface, there are no scatterers in the environment to produce multipath signal components. Using the narrowband assumption and considering the spatial signature model explained in Chapter 2, the output at the array $\vec{\mathbf{x}}_i(t)$ due to mobile user i can be modeled as:

$$\vec{\mathbf{x}}_1(t) \cong \alpha_1(t)\vec{\mathbf{a}}(\theta)s_1(t) \tag{4.3}$$

$$\vec{\mathbf{x}}_2(t) \cong \alpha_2(t)\vec{\mathbf{a}}(\theta+\delta)s_2(t) \tag{4.4}$$

where δ is on the order of 1°. The $\alpha_i(t)$ take into account the relative strength of the signals from each of the mobile users, which will be smaller for user 2 who is further from the array. Note that while there are multipath components in this scenario, corresponding to rays bouncing off of the asphalt ground plane, the array architecture and model presented can only distinguish azimuth-varying signal components. From the perspective of the base station array, the only effect of these "ground-bounce" components is to constructively and destructively interfere with the direct path signal component and change the magnitude of $\alpha_i(t)$.

4.3.4.2 – Case 2

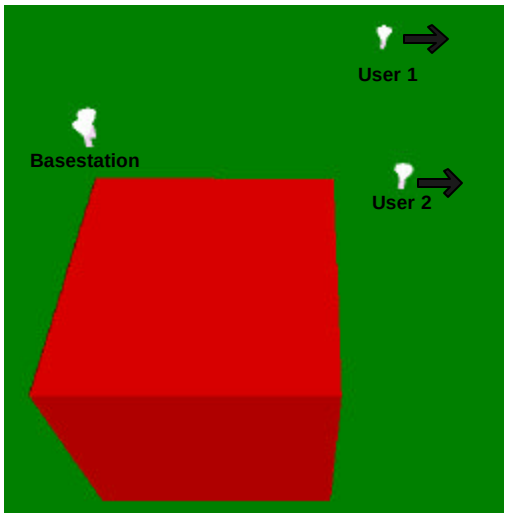

(A)

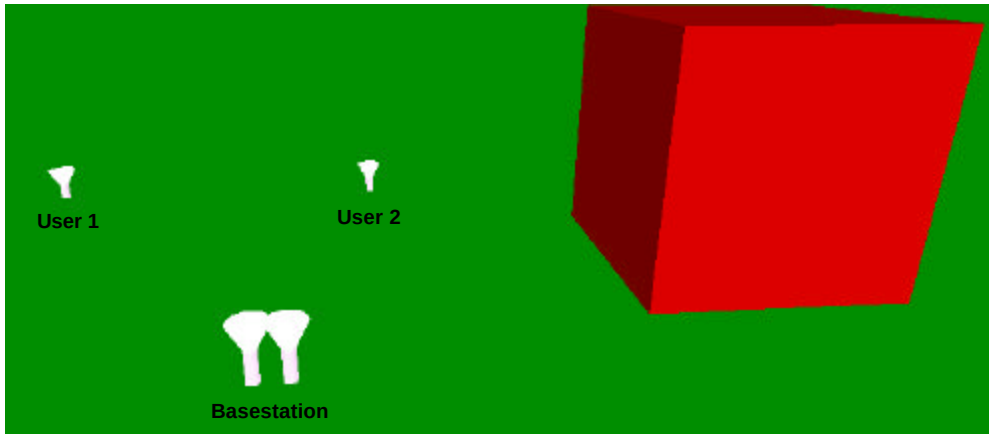

(B)

Figure 4.2 – Case 2 Illustration (A) Side View (B) Base station View

In this scenario, both users are again in the LOS of the base station and move away from the array. However, there is a building inserted that produces a multipath signal component for user 1 and a stronger multipath signal component corresponding to user 2. Neglecting relatively weaker diffraction effects, the array output to the signals of each of these users can be modeled as:

$$\vec{\mathbf{x}}_1(t) \cong (\alpha_{DOM,1}(t)\vec{\mathbf{a}}(\theta_{DOM,1}) + \alpha_{REF,1}(t)\vec{\mathbf{a}}(\theta_{REF,1}))s_1(t) \tag{4.5}$$

$$\vec{\mathbf{x}}_2(t) \cong (\alpha_{DOM,2}(t)\vec{\mathbf{a}}(\theta_{DOM,2}) + \alpha_{REF,2}(t)\vec{\mathbf{a}}(\theta_{REF,2}))s_2(t) \tag{4.6}$$

where the attenuation of the signal components corresponding to the dominant multipath component for each user $\alpha_{DOM,i}(t)$ are approximately equal due to the fact that the users are the practically the same distance from the base station array. Due to the location of each user relative to the building, the attenuation of the signal component corresponding to the building reflection, $\alpha_{REF,i}(t)$, will in general be larger for user 2 than for user 1. In addition each of the components

seen by the array for both users is superposed with a ground bounce ray that is included in the corresponding α coefficient.

4.3.4.3 – Case 3

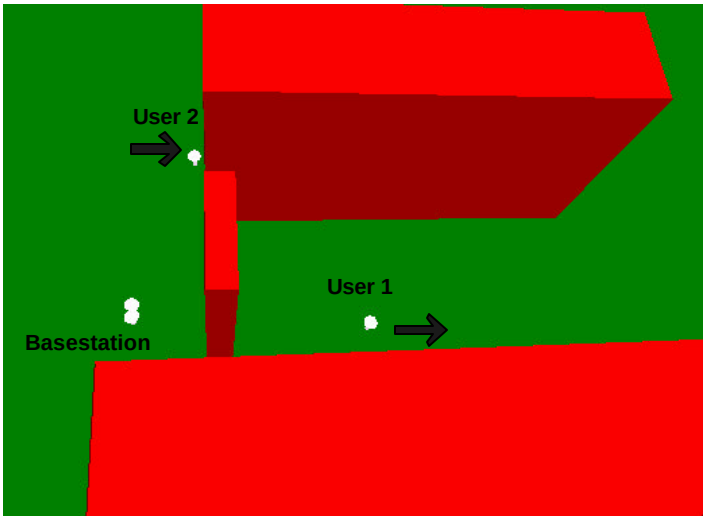

(A)

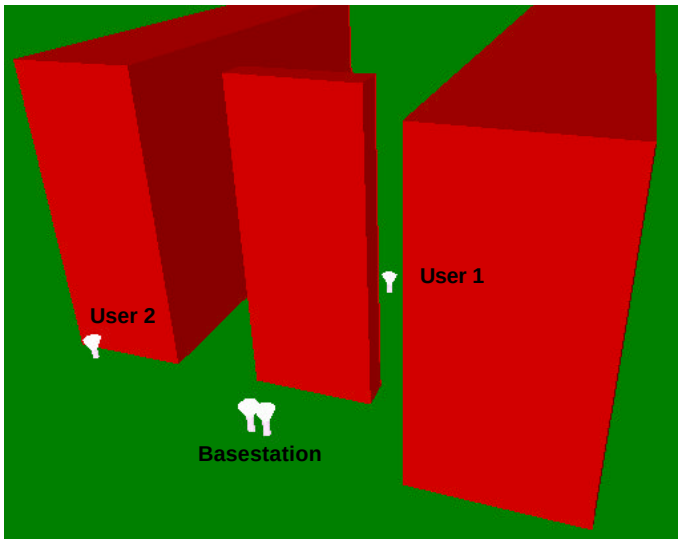

(B)

Figure 4.3 – Case 3 Illustration (A) Side View (B) Base station View

In this scenario, the first mobile user is non line of sight (NonLOS) since it is effectively surrounded by buildings, and is moving away from the array. The second mobile user is in LOS with the array, but is moving away from the array towards a building that provides local scattering. The output of the array due to these users signals can be represented by:

$$\vec{\mathbf{x}}_1(t) \cong \sum_{j=1}^{N_{M,1}} \alpha_{j,1}(t)\vec{\mathbf{a}}(\theta_{j,1})s_1(t) \tag{4.7}$$

$$\vec{\mathbf{x}}_2(t) \cong \left[\alpha_{DOM,2}(t)\vec{\mathbf{a}}(\theta_{DOM,2}) + \sum_{j=1}^{N_{M,2}} \alpha_{j,2}(t)\vec{\mathbf{a}}(\theta_{j,2})\right]s_2(t) \tag{4.8}$$

where $N_{M,i}$ are the number of multipath signal components corresponding to mobile user i. Diffraction based ray mechanisms become more significant now for mobile user 1 because of the shadowed region but still not as large as reflected ray mechanisms. The presence of local scatterers in the path of mobile user 2 also imply that $\theta_{j,2}$ ($j=1..N_{M,2}$) will be clustered around $\theta_{DOM,2}$.

4.3.4.4 – Alley

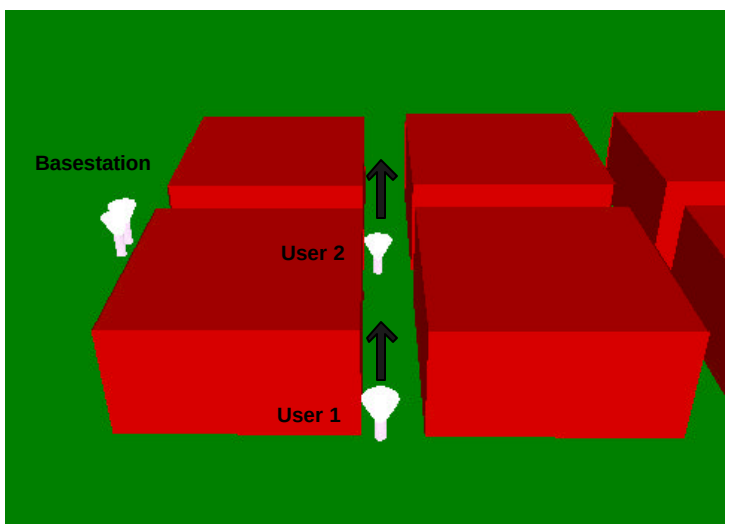

(A)

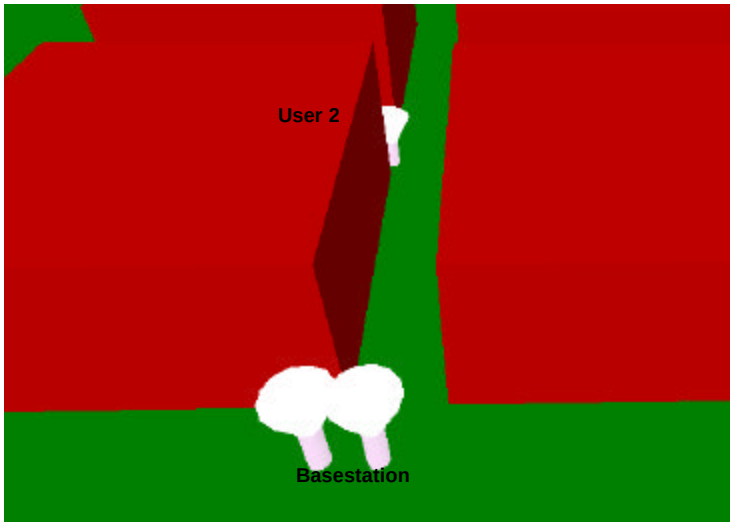

(B)

Figure 4.4 – Alley Illustration (A) Side View (B) Base station View

The alley case has two mobile users moving through the sidestreet of a rectangular grid of buildings. Both users are predominantly NonLOS with the antenna array. Specifically, mobile user 1 is NonLOS during its entire trajectory moving generally towards the array whereas mobile user 2 starts off LOS and quickly moves to NonLOS away from the array. The output of the array can be represented as:

$$\vec{\mathbf{x}}_1(t) \cong \sum_{j=1}^{N_{M,1}} \alpha_{j,1}(t)\vec{\mathbf{a}}(\theta_{j,1})s_1(t) \tag{4.9}$$

$$\vec{\mathbf{x}}_2(t) \cong \left[\alpha_{DOM,2}\vec{\mathbf{a}}(\theta_{DOM,2}) + \sum_{j=1}^{N_{M,2}} \alpha_{j,2}\vec{\mathbf{a}}(\theta_{j,2})\right]s_2(t) \tag{4.10}$$

The variables are in the above equation are defined as before. In the above expression the value of $\alpha_{DOM,2}(t)$ decays relatively quickly to zero as user 2 moves from LOS to NonLOS.

4.3.4.5 – Sixth Street

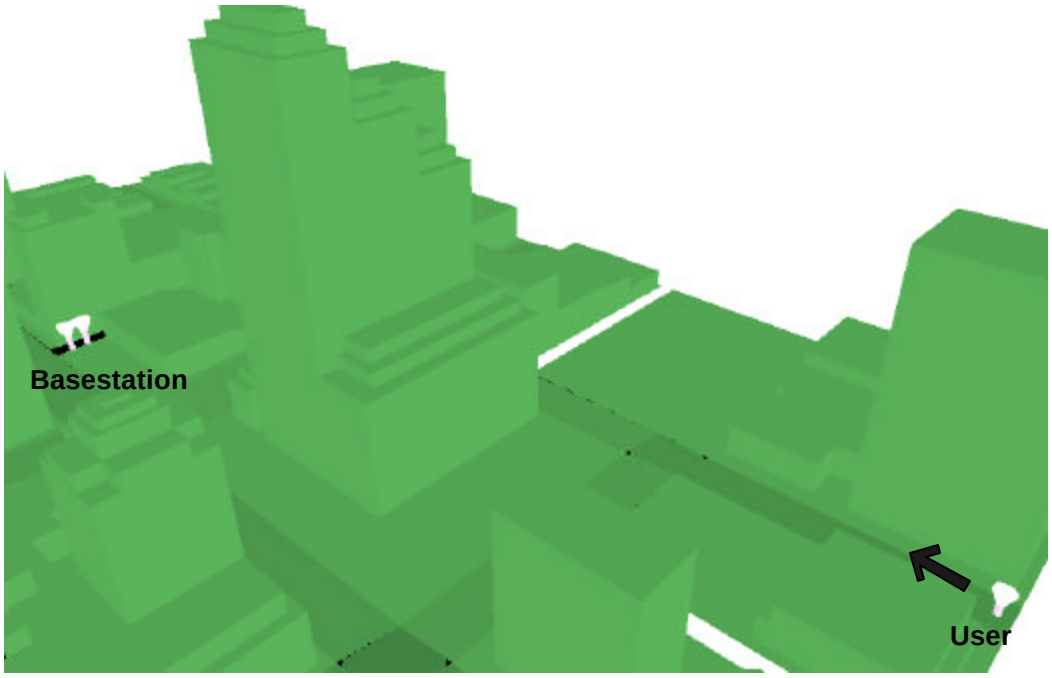

Figure 4.5 – Sixth Street Illustration

The Sixth Street scenario is the first to illustrate use of the computer model of downtown Austin, Texas. In this model, the base station array is placed 20 meters off of the ground plane in a 4 x 4 city block section of the city. The mobile user is moving along one of the streets in the grid of irregular buildings 1.5 meters off of the ground plane. During the mobile displacement considered in this part of the study, the mobile user is entirely NonLOS and moving generally towards the base station. Using a different set of steering vectors corresponding to those of the circular array geometry, the array output can be expressed similar to before for NonLOS mobile users:

$$\vec{\mathbf{x}}_1(t) \cong \sum_{j=1}^{N_{M,1}} \alpha_{j,1}(t)\vec{\mathbf{a}}(\theta_{j,1})s_1(t) \tag{4.11}$$

4.4 – RESULTS

The first set of results (Sections 4.4.1-4.4.3) involve studying the vector channel quantities described in Section 4.2 using the mobile user environments and trajectories of Section 4.3. Large-scale comments on these parameters appropriate to urban system planning will be discussed in Chapter 5. Section 4.4.4 describes the results of a method used to further model the vector channel for the purposes of forecasting future user spatial signatures based upon past spatial signatures.

4.4.1 – Power-Delay and Power-Angle Profiles

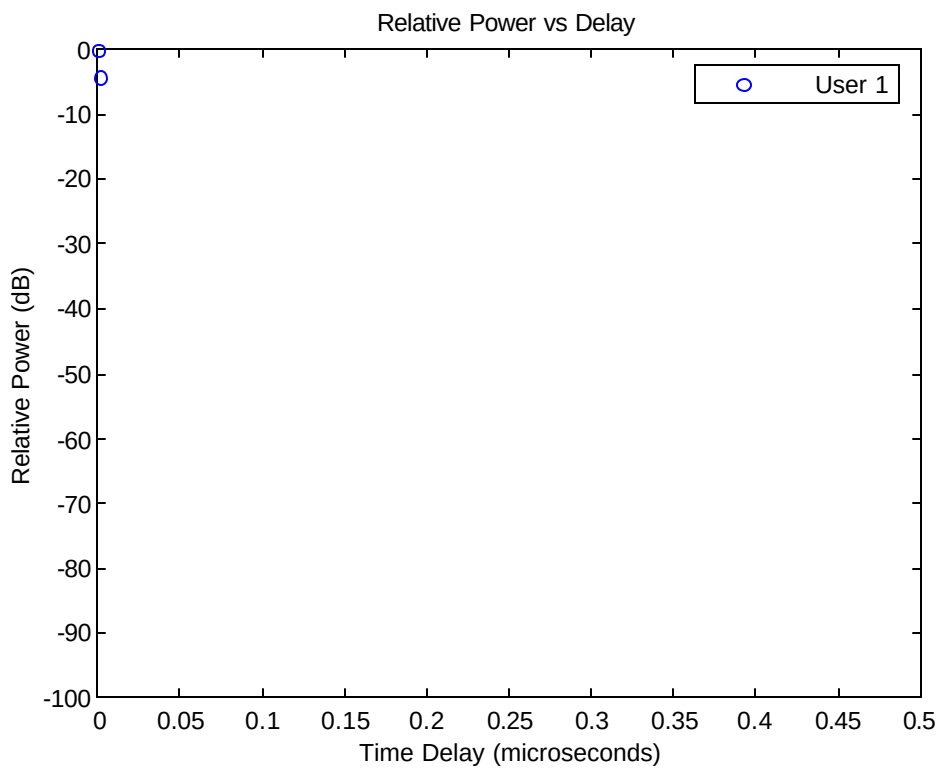

Figure 4.6 – Case 1 Mobile User 1 Power-Delay Profile

Figure 4.6 shows the power-delay profile of mobile user 1 in case 1. The profile shows, as a function of arrival time of the first multipath signal component, the strength of each multipath signal component relative to the power of the dominant signal component. Figure 4.6 simply illustrates the direct path signal component arriving very slightly before the ground-bounce multipath signal component in the top left hand corner of the graph. However, as further stated in Section 4.3.4.1, and observed through the power-angle profile, this ground-bounce signal component is not resolvable by the array and only has the effect of variably attenuating the received signal at the angle of incidence to the array.

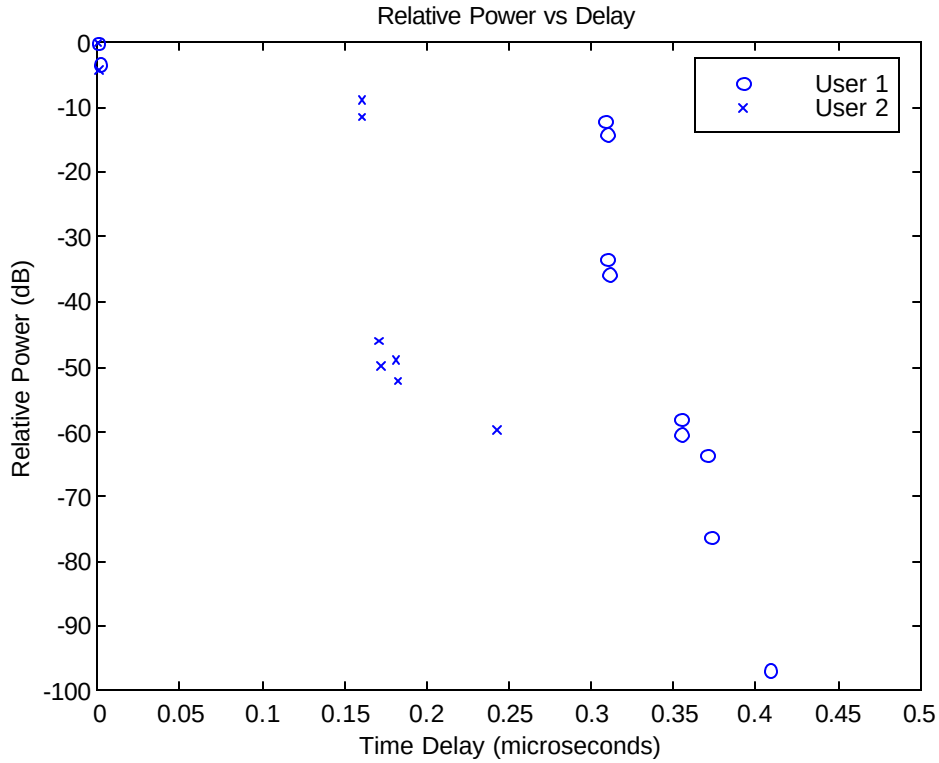

(A)

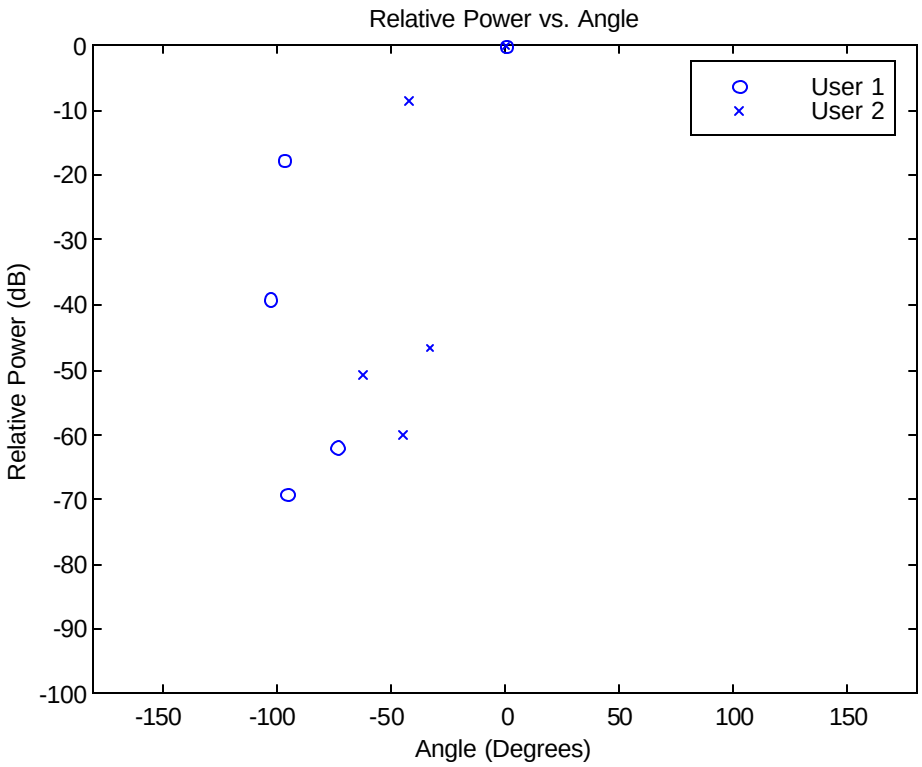

(B)

Figure 4.7 – Case 2 (A) Power-Delay Profiles and (B) Power-Angle Profiles

Figure 4.7 shows the power-delay and power-angle profiles for both mobile users in Case 2. Figure 4.7A clearly shows the LOS signal components corresponding to the direct ray mechanism (in Table 4.2) for both users and also illustrates dominant multipath signal components arriving at approximately 0.30μs and 0.15μs for users 1 and 2 respectively. These rays correspond to the reflected ray mechanism from Table 4.2. These observations agree with the discussion in Section 4.3.4.2 pertaining to representation of array output. Again, also note that both the LOS signal component and the dominant multipath signal

components for both mobile user have clearly identifiable ground-bounce signal components.

Figure 4.7B shows the power-angle profile of both users in Case 2. This profile shows, as a function of base station arrival angle relative to the angle of the dominant signal component of each user, the relative power of the other signal components. This graph clearly shows the dominant multipath signal components at approximately -100° and -50° for mobile user 1 and 2 respectively. There are other rays illustrated in both parts of Figure 4.7 that correspond to diffraction rays as well as second order ray transfer mechanisms. In LOS scenarios such as Case 2, these ray mechanisms are negligible when compared to the dominant rays in the system.

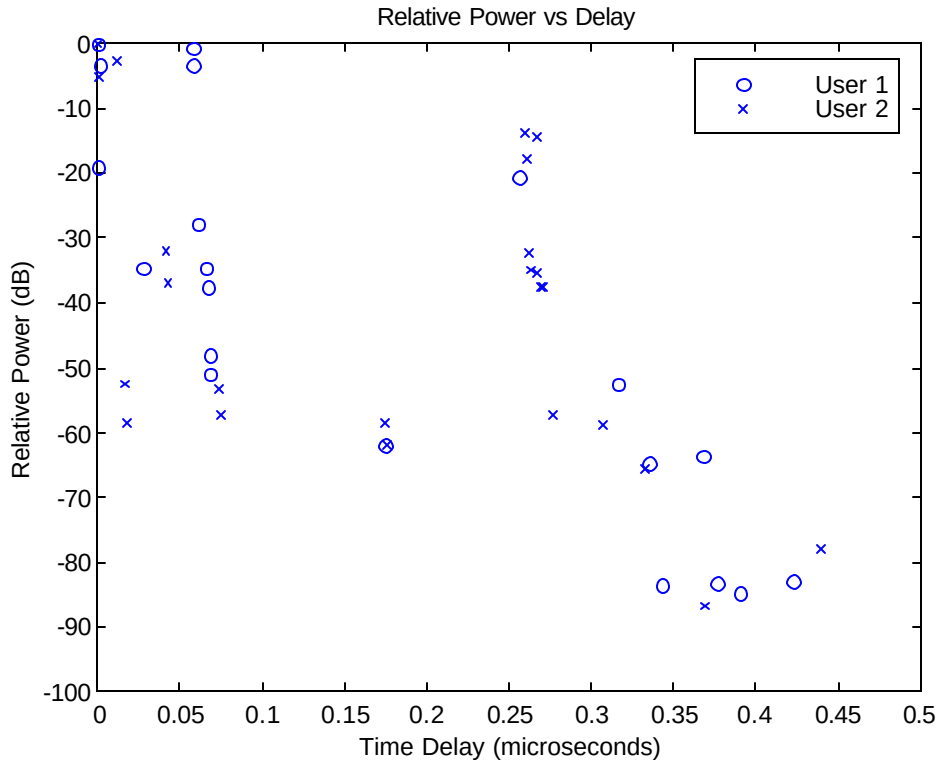

(A)

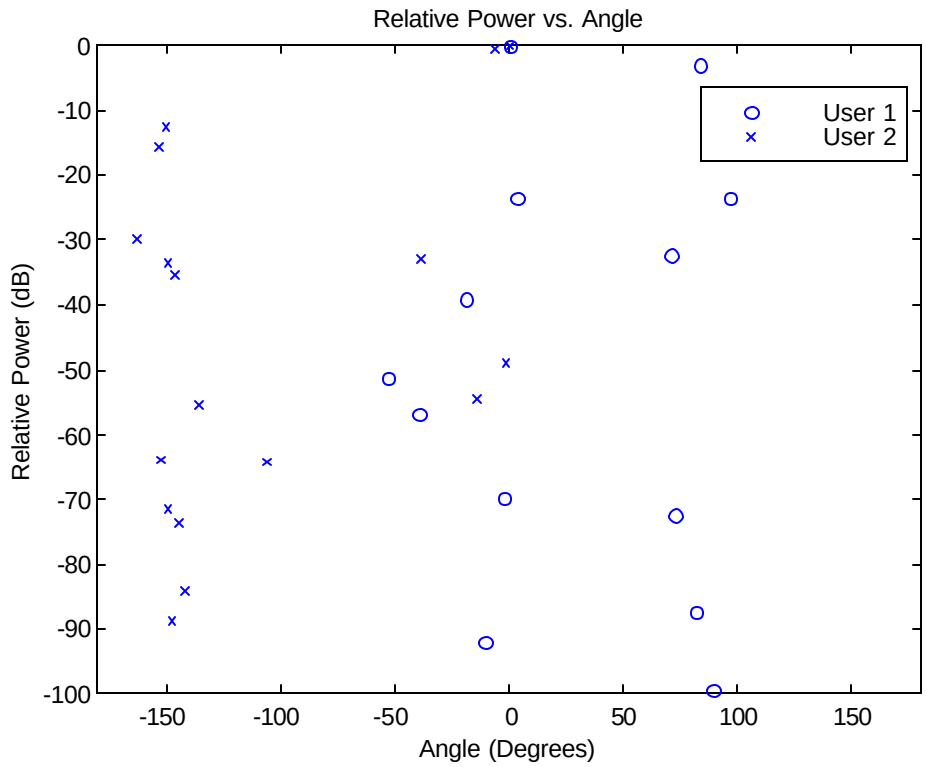

(B)

Figure 4.8 – Case 3 (A) Power-Delay Profile and (B) Power-Angle Profile

Figure 4.8 shows the power-delay and power-angle profiles for both mobile users in Case 3. The dominant multipath signal components shown in Figure 4.8A for user 1 correspond to reflected rays that fit in the gaps between the two buildings clearly illustrated in Figure 4.3B. The effect of these gaps can be seen through the banded structure (centered around both 0° and 80°) of the rays corresponding to mobile user 1 in Figure 4.8B. There is also qualitative agreement between the delay profiles of mobile user 2 in case 3 shown in Figure 4.8A along with both users in Figure 4.7A, which is not surprising since they both

correspond to scenarios in which there is a dominant ray with a multipath signal component. However, closer inspection of Figure 4.8B for mobile user 2 shows a banded structure (centered at 0° and -150°) similar to mobile user 1. The band around 0° corresponds to the dominant direct path and reflected signal components while the weaker rays centered around -150° correspond to diffraction ray mechanisms.

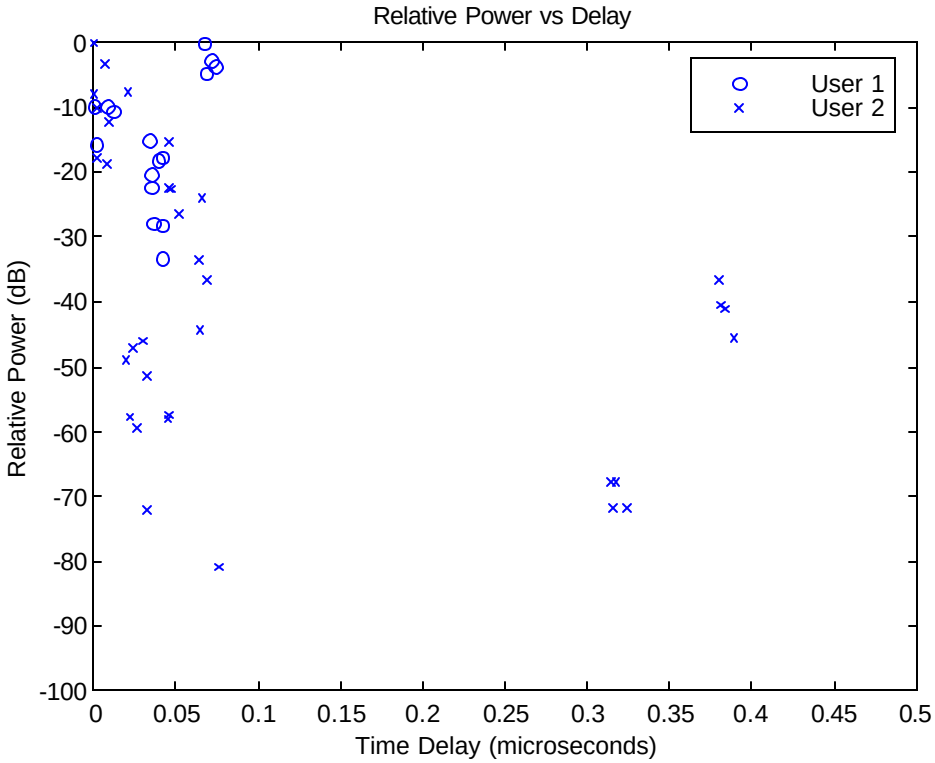

(A)

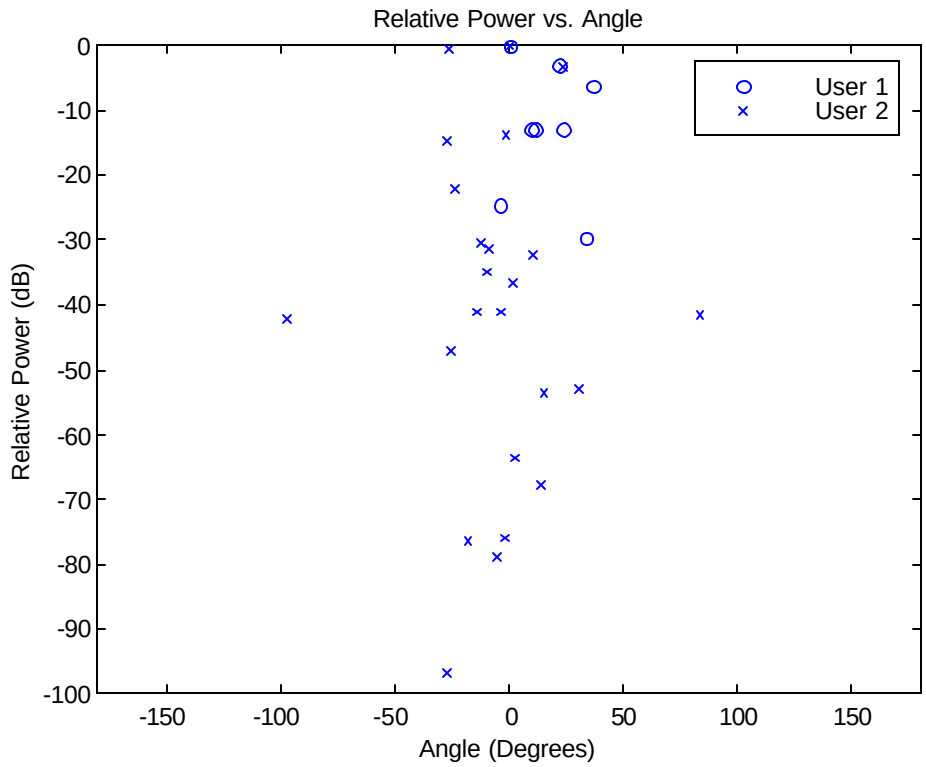

(B)

Figure 4.9 – Alley (A) Power-Delay Profile and (B) Power-Angle Profile

The power-delay and power-angle profiles for the mobile users in the Alley case are shown in Figure 4.9. Inspection of both graphs in Figure 4.9 show that the rays corresponding to user 1 are not spread very far in terms of both delay and angle. This occurs because user 1 is relatively far from the base station with all of the ray solutions involving diffraction (i.e. first order diffraction, second order diffraction-reflection, and second order reflection-diffraction). Referring to Figure 4.4, these rays all travel down the alley in which mobile user 1 is moving before traveling to the main street where the base station is located. The tendency

for these rays to be bundled together as they complete their path to the base station leads to the description of this kind of environment as an "urban canyon" observed in prior measurement studies [38]. This type of scenario is common in large cities and thus becomes important in characterizing the urban vector channel. Results such as those shown in this scenario motivate the need for array geometries that take into account these corridors of signal component arrival. The Alley scenario represents an extreme version of the urban canyon situation in that there is only one street for multipath signal components to arrive at the base station from the mobile users. This case also illustrates the importance of considering ray diffraction mechanisms in studies of this type.

The ray solutions corresponding to user 2 in this scenario are more conventional in terms of the scenarios considered thus far in that rays that correspond to reflection mechanisms are dominant. However, in these reflected rays are followed relatively closely by diffraction-based mechanisms. Again, the banding of the signals corresponding to mobile user 2 in Figure 4.9B indicates the effects of the urban canyon.

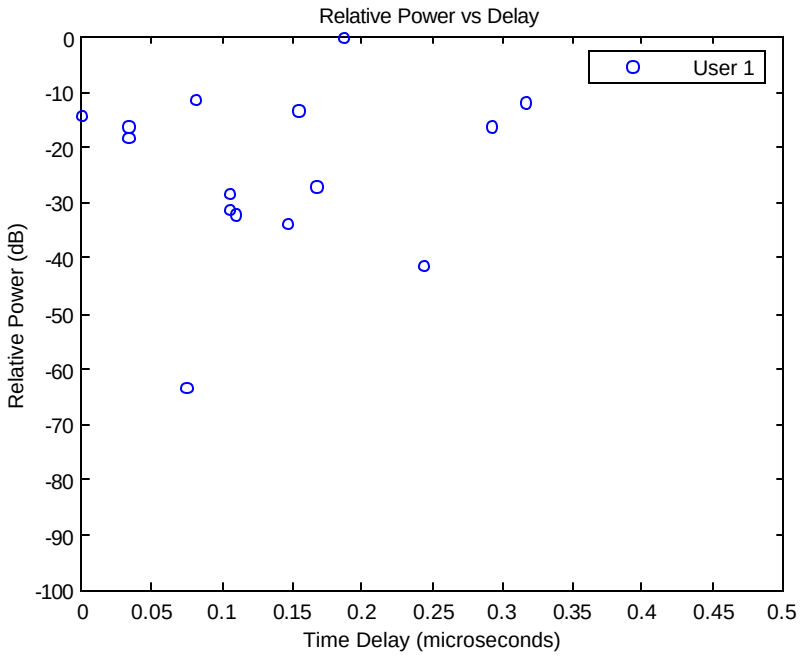

(A)

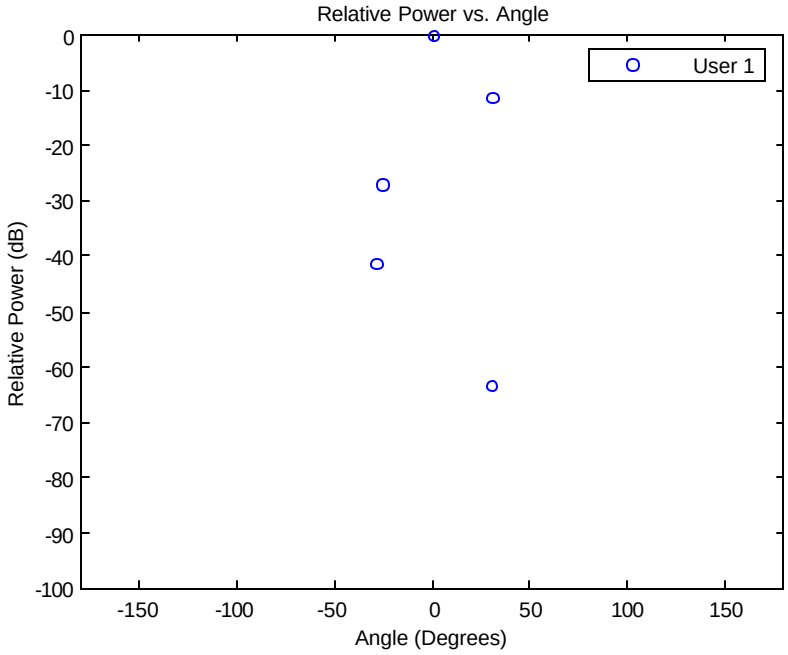

(B)

Figure 4.10 – Sixth Street (A) Power-Delay Profile and (B) Power-Angle Profile

It is significant to consider the power-delay and power-angle results of Figure 4.10 in terms of the generic urban scenarios considered previously in this section. The relatively low variation in angle of arriving signal energy indicates, like Figure 4.9B, the effect of the urban canyon focusing rays into particular angular sectors of the base station array. Comparison of Figure 4.10A with Figure 4.9A also allow us to comment that diffraction based mechanisms are dominant in this scenario since the strongest ray is not the first to arrive, which would be true when considering reflection-only situations. It can also be inferred by the lack of stronger rays with ground-bounce counterparts offset from diffracted rays, which was observed in earlier LOS and nearly-LOS scenarios. Like the alley case results, the results of the Austin simulation illustrate the need to consider diffraction based ray mechanisms.

4.4.2 – Spatial Signature Relative Angle Change

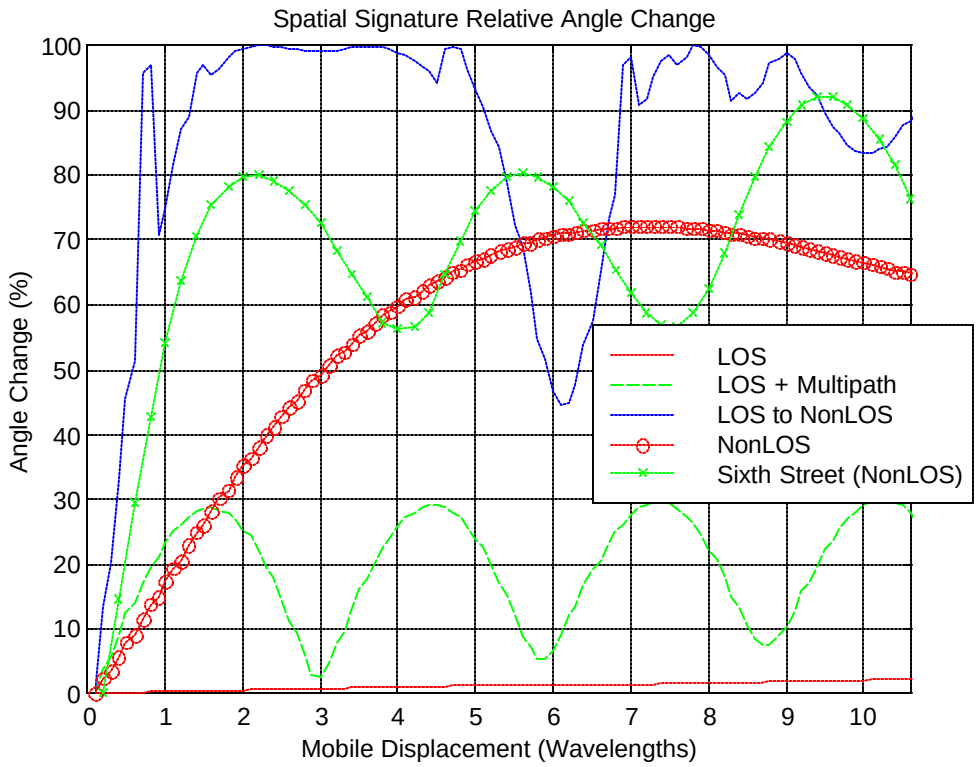

Figure 4.11 – Spatial Signature Relative Angle Change Overview

Legend Key	Scenario	User
LOS	Case 1	1
LOS + Multipath	Case 2	1
LOS to NonLOS	Alley	2
NonLOS	Alley	1
Sixth Street (NonLOS)	Sixth Street	1

Table 4.3 – Relative Angle Change Overview Graph Key

Figure 4.11 shows a summary plot of spatial signature relative angle change for the scenarios described in Section 4.3.4. Table 4.3 provides a reference matching the legend of Figure 4.11 to the particular users and scenarios

described in Section 4.3.4. The change between spatial signatures is measured between the first spatial signature in the trajectory with each subsequent spatial signature as the mobile user goes through a particular environment. Relative angle change simulations of this type give information about small-small scale spatial signature dynamics and provide insight into how often signature estimates need to be updated by the base station for effective downlink beamforming [27]. Table 4.4 summarizes the results of spatial signature relative angle change simulations for each of the scenarios tested in this chapter.

Scenario Name	User	Mean RAC (%)	Std RAC
Case 1	1	1.32	0.77
	2	0.31	0.15
Case 2	1	19.13	8.22
	2	42.18	19.69
Case 3	1	57.54	25.97
	2	87.62	11.90
Alley	1	56.42	19.53
	2	85.31	19.66
Sixth Street	1	68.93	17.76

Table 4.4 – Spatial Signature Relative Angle Change Summary Table

The LOS scenario, which corresponds to Case 1 mobile users, shows very little spatial signature relative angle change. This agrees with the model given in equations (4.3) and (4.4). Since each user's spatial signature in this case is a single, variably attenuated steering vector, only the vector amplitude is changing. Recall that the variable attenuation is due to varying constructive and destructive interference between direct path ray and ground-bounce ray. Thus, the angle characteristics of the spatial signature remain relatively constant. The scale of

spatial signature RAC illustrated in Figure 4.11 and shown in Table 4.4 is consistent with that of the RAC between two array steering vectors separated by several tenths of a degree. This agrees with the angular variation with respect to the base station of each user over the length of their displacement in Case 1.

The situation in Case 2, referred to as "LOS + Multipath" in Figure 4.11, shows greater amount of RAC and RAC variation than Case 1 results. The performance of this graph is consistent with the model given in equations (4.5) and (4.6) and is indicative of a particular fading scenario. Specifically, the magnitude of the RAC variation can be reproduced by considering the RAC of a superposition of two steering vectors (of this specific array geometry) and varying the strength of one steering vector (corresponding to the multipath component) to around 30% of the other steering vector (representing the dominant path). As the multipath steering vector becomes stronger relative to the dominant path steering vector, the RAC grows. This effect also explains why the spatial signature RAC is greater for user 2 than for user 1, as shown in Table 4.4. These results, like the previous result in Case 1, agree with measurement studies conducted using a smart antenna testbed [24].

In general, greater RAC occurs when steering vectors corresponding to multipath signal components are introduced or depart as the mobile user traverses a particular environment. This is the situation in the LOS to NonLOS plot in Figure 4.11. Recall that the appropriate mobile user in the alley case starts LOS with the base station array and then moves behind a building. This loss of a dominant steering vector explains the large jump in RAC with less than one

wavelength of mobile user displacement. It also explains the relative unpredictability of the graph since RAC measurements are made relative to the spatial signature with the dominant signal component included. Thus, we can conclude from this graph that situations in which there is a transition from one type of fading model to another causes particularly unstable spatial signature variation.

The NonLOS scenarios shown in Figure 4.11 corresponding to user 1 in the alley model and the sixth street model, have results very similar to the other NonLOS scenario (case 3, user 1). In these scenarios, there are no LOS rays to provide a dominant steering vector in the spatial signature representation of array output. Reflection ray mechanisms and diffraction ray mechanisms provide a relatively large number of steering vectors that each individually vary in strength as the mobile user moves through the environment. While the RAC in these scenarios do not reach the level that occurs when dominant signal components are added or removed, they still reach appreciable levels after relatively small mobile user displacement.

4.4.3 – Downlink Signal to Interference Ratio

Table 4.5 summarizes the two-user simulations of signal to interference ratio for the scenarios described in Section 4.3.4 using the methods described in Section 2.6. Spatial signature or DOA estimation (whichever is appropriate for the downlink beamforming method) is only performed at the first position of each mobile user. This was done to observe the effect of inaccurate spatial signature or DOA knowledge on SIR results. A detailed paper on this topic can be found in

Arredondo and Dandekar [27]. For all of these simulation results, interference energy is the energy intended for one mobile user that reaches the other mobile user. For the purpose of separating array effects and environment effects, DOA-based downlink beamforming methods are based upon their conventional definitions and do not include the refinements discussed in Chapter 3.

Scenario	Method	User 1 Mean SIR (dB)	User 1 Std SIR	User 2 Mean SIR (dB)	User 2 Std SIR
Case 1	DomDOA	2.50	0.06	2.95	0.01
	PseDOA	30.85	1.42	23.02	0.24
	SS	2.88	0.06	3.01	0.01
	PseSS	39.58	26.36	51.65	24.42
Case 2	DomDOA	27.54	4.33	16.17	2.36
	PseDOA	19.01	1.64	29.54	3.25
	SS	31.25	3.61	19.97	6.10
	PseSS	32.67	26.89	23.52	30.38
Case 3	DomDOA	17.18	2.78	7.15	4.45
	PseDOA	20.93	5.13	4.90	2.76
	SS	11.32	6.27	11.90	4.02
	PseSS	18.03	29.70	18.70	29.30
Alley	DomDOA	1.15	1.32	-1.02	4.99
	PseDOA	2.64	1.19	-1.94	7.63
	SS	5.30	0.50	-0.18	10.18
	PseSS	13.98	28.74	3.35	30.54

Table 4.5 – Downlink Signal to Interference Ratio Summary Table

Table 4.5 shows that the PseSS method generally performed better than the other downlink beamforming methods. While this method had the best average performance, it also had the greatest fluctuation. This greater fluctuation was because of the initial loss in downlink beamforming performance due to

inaccurate spatial signature knowledge, which is one of the motivations behind updating spatial signature estimates as often as possible as well as forecasting future spatial signatures based upon last known values (described in Section 4.4.4). The increased performance of these four methods due to more accurate spatial signature knowledge can be found in Dandekar [39].

The PseDOA method and SS method were behind the PseSS method. However, there was no clear second-place method with the PseDOA and SS method each outperforming the other in certain situations. While the DomDOA method generally did not perform as well, there were also situations where the method performed solidly.

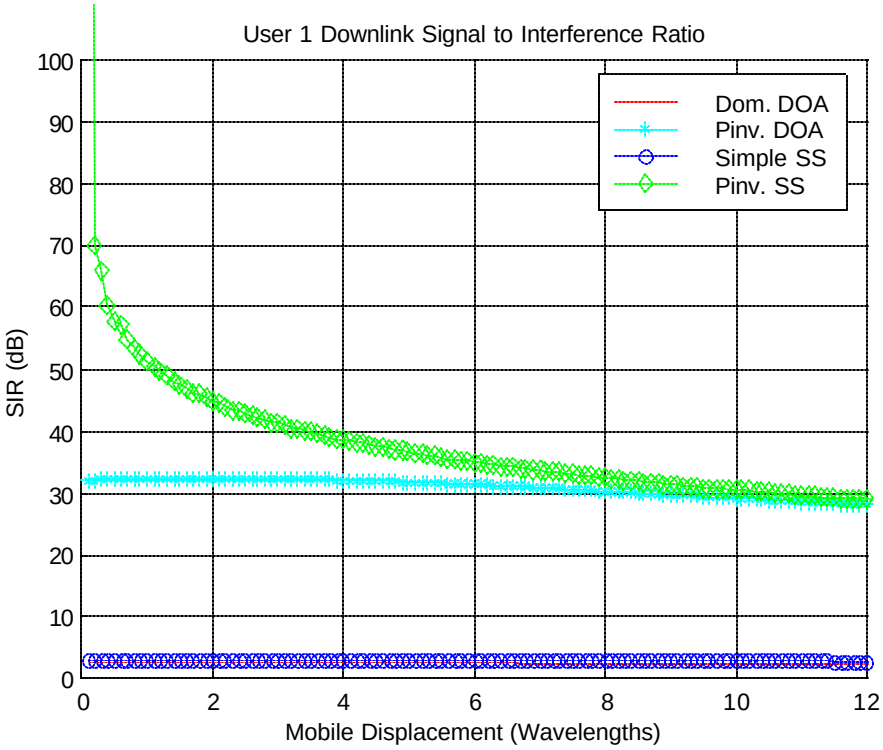

Figure 4.12 - Case 1 Downlink Signal to Interference Ratio – User 1

Figure 4.12 shows the downlink SIR simulation results for mobile user 1 in case 1. As the graph shows, the PseSS method performed the best but quickly lost performance as the last known spatial signature became more outdated. The pseudoinverse methods performed better than the other methods in this scenario for both mobile users. This occurred since the angular separation between the mobile users was so small. Specifically, methods relying on directional transmission alone maximized signal power transmitted to the mobile user without including reduction of interference power. As shown by the performance of the DomDOA and SS method in this scenario, directional methods alone transmit nearly equal amounts of signal and interference to the mobile users. Due to the fact that the spatial signatures for the mobile users were relatively stable in this scenario, as discussed in Section 4.3.4.1 and 4.4.2, the downlink beamforming performance was very stable. These results are all consistent with the smart antenna system measurements described in [8].

The downlink SIR performance graph for user 1 in case 2 is shown in Figure 4.13. All the methods in this situation worked relatively well. As shown in this graph and in Table 4.5, the PseSS method and the SS method performed comparably well. The DomDOA and PseDOA method in this scenario each worked best for a particular mobile user. The level of fluctuations for both mobile users in the PseSS method tended to decrease as the mobile users moved further along their trajectory since the PseSS method is particularly reliant on accurate spatial signature estimates. The other methods had relatively stable

levels of fluctuation that arose due to the combined multipath fading environment of both users.

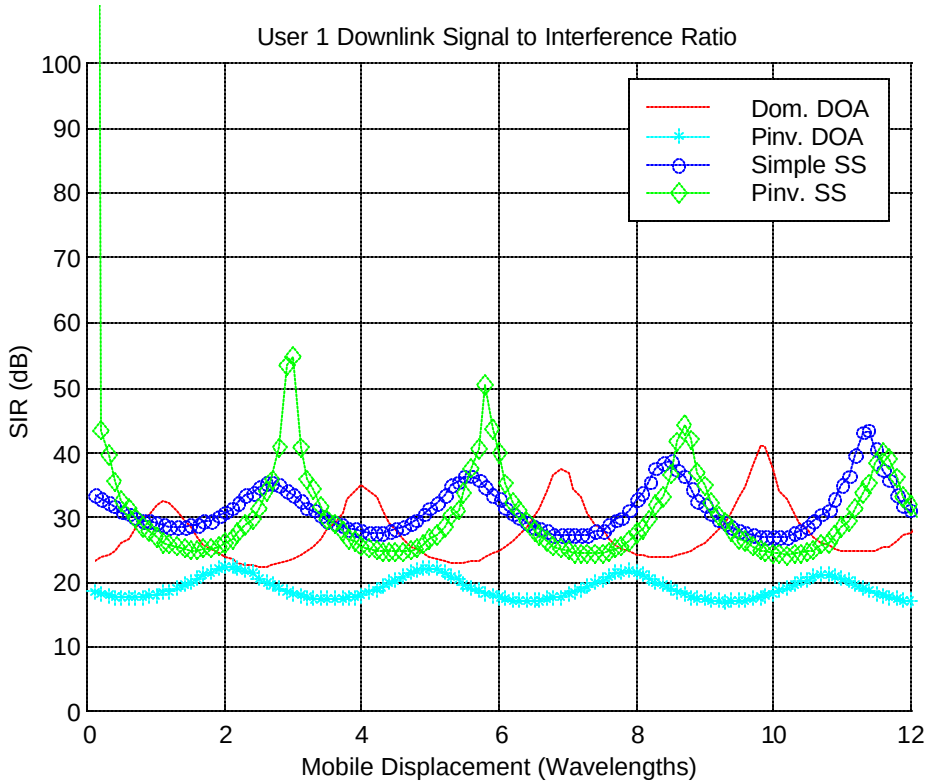

Figure 4.13 - Case 2 Downlink Signal to Interference Ratio – User 1

Case 3 downlink SIR results are shown in Figure 4.14 for mobile user 1. Recall from Figure 4.3 that this mobile user was NonLOS and nearly completely surrounded by buildings. As shown in Table 4.5, for this particular mobile user, the PseDOA method slightly outperformed the PseSS method in terms of average performance. As shown on the graph, the PseDOA method had much less fluctuation than the PseSS method. In addition, all four methods were able to get relatively high levels of SIR to this mobile user compared to that seen by the LOS

mobile user in this scenario. The favorable PseDOA results shown in Figure 4.14, along with results corresponding to Case 2, user 2 suggest that in the absence of perfect spatial signature information, DOA based methods may be a sound alternative due to their relatively stable performance.

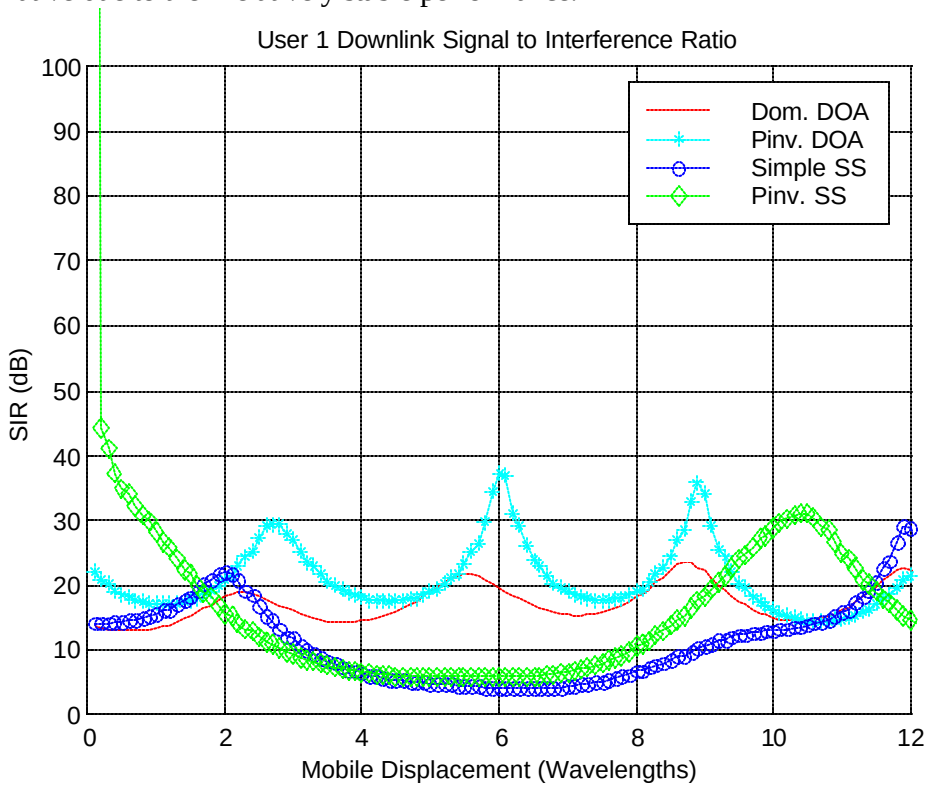

Figure 4.14 - Case 3 Downlink Signal to Interference Ratio – User 1

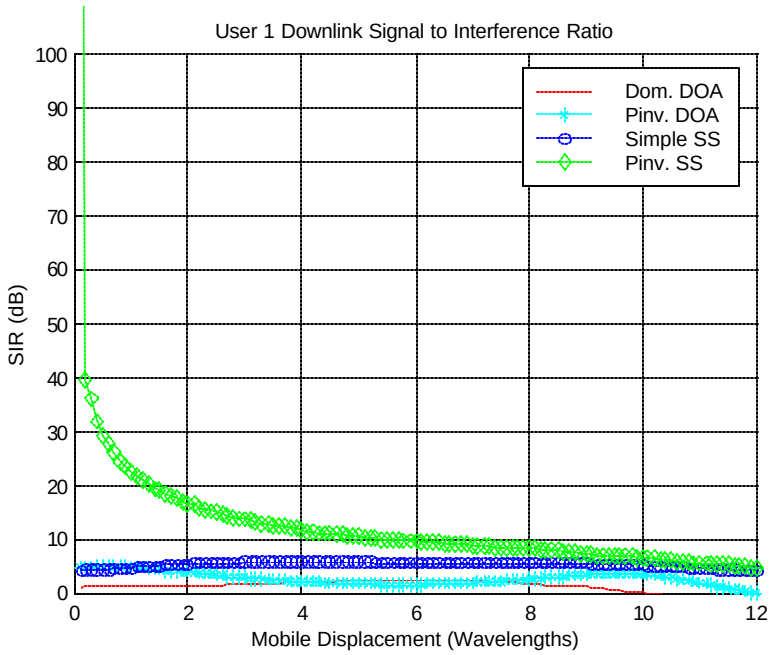

Figure 4.15 - Alley Downlink Signal to Interference Ratio – User 1

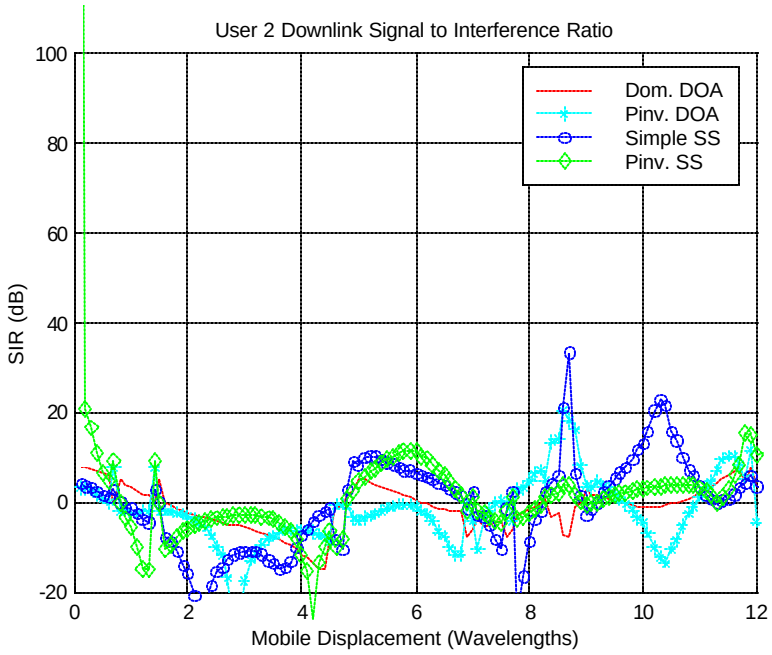

Figure 4.16 - Alley Downlink Signal to Interference Ratio – User 2

Figures 4.15 and 4.16 show the downlink SIR simulation results for mobile users 1 and 2 respectively in the alley scenario. Despite the fact that the spatial signature RAC (from Figure 4.11) gets relatively large for user 1, only the PseSS method suffers a large performance loss, as seen in Figure 4.15. However, it should be pointed out that the SIR for any of the methods for this mobile user is not particularly good. Figure 4.11 showed a very large change in spatial signature RAC for mobile user 2. As Figure 4.16 shows, the transition in channel characteristics responsible for this large RAC causes a breakdown of nearly all of the downlink beamforming methods after relatively little mobile user displacement. The results from this scenario represent an extreme urban canyon scenario since all signal energy is directed down a single street and there are no other sidestreets to provide multipath diversity. Chapter 5 will examine the urban vector channel in greater detail.

4.4.4 – Vector Channel Prediction

In the previous section, the performance of downlink beamforming methods was shown to be extremely sensitive to accurate spatial signature knowledge. Mobile user displacements corresponding to fractions of a single wavelength significantly degraded downlink beamforming performance. This degradation was specifically studied in [27]. Thus, it is important for the base station to have an accurate estimate of channel state information (CSI). The reason for this performance degradation is the changing multipath fading environment encountered as the mobile user moves along a given path. In the context of vector channel propagation, the spatial signature RAC metric

introduced in Section 4.2.1 and illustrated in Section 4.4.2 quantifies this changing fading environment.

Prediction of the fading channel encountered by conventional communications systems has been studied in the past. A survey of these scalar channel prediction techniques can be found in the paper by Duel-Hallen [40]. Duel-Hallen then specifically developed a low complexity, adaptive, long-range prediction system that models the scalar fading channel using an autoregressive (AR) model. Duel-Hallen also suggested that predictions were necessary on the order of several tens of milliseconds into the future, corresponding to several wavelengths of mobile user displacement.

The proposition to apply this kind of prediction to the vector channel was first shown by Arredondo [41-43]. Arredondo models each individual channel in the vector channel using a single AR model derived from past observations of all channels. This system uses anywhere between 6 and 10 wavelengths worth of known vector channel data to predict effectively up to 2 wavelengths into the future.

4.4.4.1 – Proposed Model

The quantitative motivation for spatial signature prediction can be found in the spatial signature variation and downlink beamforming studies found earlier in Chapter 4. Specifically, the degradation of downlink SIR performance (which ultimately leads to increased bit error rate) as spatial signature RAC increases motivates the need to keep spatial signature estimates accurate. In terms of the directional transmission capabilities of SDMA systems discussed in Chapter 2, a

qualitative motivation to spatial signature prediction is to aim signal energy to where the mobile user will be in the future rather than using an increasingly unreliable last known position.

In this dissertation, a novel extension to past prediction work is proposed. In this method, a vector autoregressive (VAR) spatial signature model is developed. This method uses a Kalman filter state space representation to recursively build the model. This limits the number of large matrix inversions and makes the method attractive for future real-time implementation.

The physical justification for this model arises from the mutual coupling study of Chapter 3. Since the antenna array elements are located so close to one another, the correlation among the element data can be used beneficially in forecasting without having to rely on storing many past channel values. Specifically, in the VAR formulation, each variable's forecast depends not only on the past values of that variable, but also on all the past values of the other variables. Also unlike [41-43], the prediction system used in this study also allows the model to vary from one channel to another.

The proposed spatial signature prediction method is based upon the treatment in Harvey [44] of a linear regression model. The basic model form is shown in equation (4.12):

$$\vec{\mathbf{y}}_t = (\vec{\mathbf{x}}_t)'\mathbf{B}_t + \vec{\mathbf{e}}_t \tag{4.12}$$

where $\vec{\mathbf{y}}_t$ is a 1 x M vector corresponding to the transpose spatial signature vector being predicted at time t where M is the number of antenna array elements. $\vec{\mathbf{x}}_t$ is an h x 1 vector that contains the current base station CSI which

are the past spatial signatures used to generate the predicted spatial signature. This vector takes the following form:

$$\vec{\mathbf{x}}_t = \begin{bmatrix} \vec{\mathbf{a}}_{t-1} \\ \hline \vdots \\ \hline \vec{\mathbf{a}}_{t-g} \end{bmatrix} \tag{4.13}$$

g is a constant that specifies the number of lagged spatial signatures to use which is related to the dimension of the $\vec{\mathbf{x}}_t$ by h = Mg. The matrix $\mathbf{B}_t$ is h x M and contains as its columns the vector $\vec{\mathbf{b}}_{t,i}$ for i = 1, … , M. $\vec{\mathbf{b}}_{t,i}$ is an h x 1 column vector that specifies the coefficients to apply to all components of the lagged spatial signatures in $\vec{\mathbf{x}}_t$ to develop the value of the ith component of the forecast spatial signature. $\vec{\mathbf{e}}_t$ is a 1 x M vector modeling the forecast error.

h observations are needed to develop an initial estimate of $\mathbf{B}_t$, (denoted as $\hat{\mathbf{B}}_h$) determined using the following equation:

$$\hat{\mathbf{B}}_h = \left(\mathbf{X}_h'\mathbf{X}_h\right)^{-1}\mathbf{X}_h\mathbf{Y}_h \tag{4.14}$$

where $\mathbf{X}_t$ is a t x h matrix that contains as row j (j = 1, …,t), the vector $\vec{\mathbf{x}}_j'$ and $\mathbf{Y}_t$ is a t x M matrix that contains as row j (j=1,…t), the vector $\vec{\mathbf{y}}_j$. To develop a refined estimate of $\hat{\mathbf{B}}_t$, for t > h+1, a Kalman filter representation of the model in equation (4.12) is used to build a recursive least squares estimator that does not require any further matrix inversions. For each of the i components (i=1,…M) and t > h+1 we can write [44]:

$$\hat{\vec{\mathbf{b}}}_{t,i} = \hat{\vec{\mathbf{b}}}_{t-1,i} + (\mathbf{X}_{t-1}'\mathbf{X}_{t-1})^{-1}\vec{\mathbf{x}}_t(y_{t,i} - \mathbf{x}_t'\hat{\vec{\mathbf{b}}}_{t-1,i})/f_t \tag{4.15}$$

$$(\mathbf{X}_t'\mathbf{X}_t)^{-1} = (\mathbf{X}_{t-1}'\mathbf{X}_{t-1})^{-1} - (\mathbf{X}_{t-1}'\mathbf{X}_{t-1})^{-1}\vec{\mathbf{x}}_t\vec{\mathbf{x}}_t'(\mathbf{X}_{t-1}'\mathbf{X}_{t-1})^{-1}/f_t \tag{4.16}$$

$$f_t = 1 + \vec{\mathbf{x}}_t'(\mathbf{X}_{t-1}'\mathbf{X}_{t-1})^{-1}\vec{\mathbf{x}}_t \tag{4.17}$$

After the given training interval is over, the estimate of $\hat{\mathbf{B}}_t$ is applied using the model form of equation (4.12) to forecast future spatial signatures based upon past known spatial signature values. As these forecasts go further into the interval of time when actual spatial signature values are not known, $\vec{\mathbf{x}}_t$ will rapidly only contain predicted spatial signatures and future forecasts will be a function of past forecasts. The number of predictions that are made after the training interval is referred to as the prediction horizon [43].

4.4.4.2 – Model Parameters

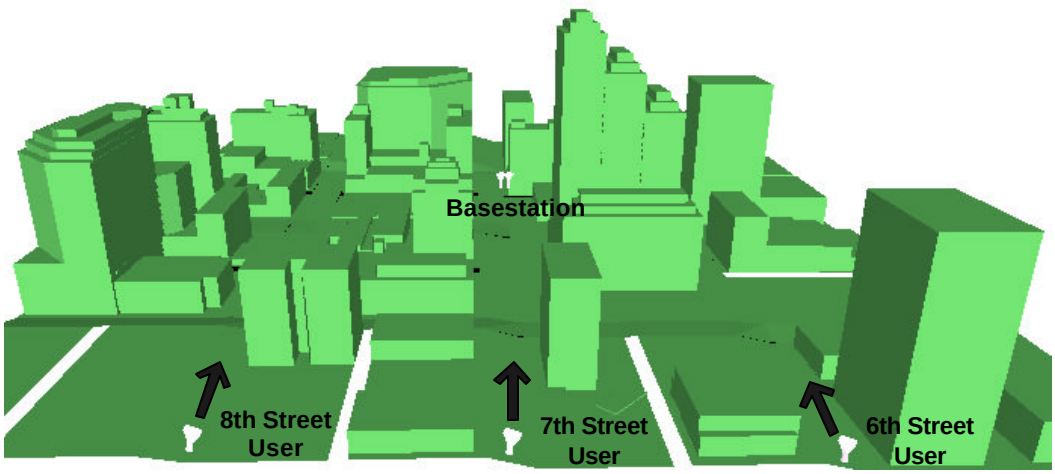

Figure 4.17 – Prediction Simulation Environment

The performance of the model described in the previous section was examined using simulation data corresponding to vector channel data in a 4 x 4 city block area of downtown Austin, Texas. These scenarios are illustrated in Figure 4.17 and all involve the use of uniform circular antenna array of $\lambda/2$ dipoles with mutual coupling effects included. There were three separate mobile user paths that were considered, corresponding to movement down sixth, seventh,

and eighth streets. High-resolution field simulations were made every $\lambda/5$ of mobile displacement over approximately 0.5 kilometers of city street. A time division duplexed system was assumed, with a total training interval of 35 spatial signatures. This corresponds to the type of system described in [43]. When regions of forecasted spatial signatures are included in the mobile trajectory, corresponding to base station predictions made during downlink, there were approximately 200 uplink-downlink cycles considered per mobile trajectory.

The sixth street trajectory is much longer than the one described in Section 4.3.4.5. Most of the length of this trajectory is NonLOS with the exception of several portions that provide LOS signal components. This is also the case with the eight street mobile user trajectory. In contrast, as shown in Figure 4.17, the seventh street mobile trajectory includes LOS signal components. These tests were chosen to be representative of the type of signal environment found in an urban microcell.

A central issue that needed to be addressed in the development of the model is a determination of g, the number of lagged spatial signature values to consider in the model. Since the basic model of 4.12 represents linear regression, an analysis of variance (ANOVA) based approach was used to identify the minimum necessary lag to achieve an acceptable level of explanatory power. Specifically, the r^2-statistic corresponding to the coefficient of determination [45] of the regression was developed using the simulation data described above. This test statistic measures the proportion of the total variation of the data that is fit by the regression model. This statistic only examines the accuracy of the one step

ahead forecast for each component of the spatial signature. In order to examine the effectiveness of the model several steps ahead, the spatial signature RAC metric described in Section 4.4.2 was used.

4.4.4.3 – Model Performance

Table 4.6 shows the coefficient of determination for the regression of one channel in each three cases described in the previous section. As this table shows, nearly all data variation in the one step ahead spatial signature forecasts can be explained by using a lag of 2 spatial signatures. Specifically, 93% or more of the observed data variation can be explained through a linear regression model using 2 lagged spatial signatures.

Scenario	Number of Lagged Spatial Signatures	Coefficient of Determination
Sixth Street	1	0.77
	2	0.99
Seventh Street	1	0.64
	2	0.93
Eighth Street	1	0.85
	2	0.97

Table 4.6 – Coefficient of Determination vs. Number of Lagged Spatial Signatures

While the above table justifies the choice of model and lag for one step ahead forecasts, the model needed to be able to generate accurate spatial signature forecasts as far into the future as possible after the end of the training period. The accuracy of these spatial signature forecasts was measured using spatial signature RAC over a prediction horizon corresponding to six wavelengths of mobile user

displacement. This satisfies the forecasting interval requirements of the long-range prediction scheme in [40], while also taking into account implementation issues by reducing the number of large matrix inversions necessary through use of the Kalman recursive update equations, (4.15)-(4.17).

Figure 4.18 illustrates the effectiveness of spatial signature prediction over the first 5 downlink cycles of the sixth street mobile user trajectory. Conventional spatial signatures refer to the situation when the last known uplink spatial signatures are used during the entire downlink interval. Forecast spatial signatures refer to predictions based upon known signatures at first and then eventually based upon predictions alone. The $\hat{\mathbf{B}}_t$ from equation (4.12) is fixed at the time of the last known spatial signature when developing the forecasts. As Figure 4.18 shows, when conventional spatial signatures are used, the RAC with respect to the actual spatial signatures quickly reaches 80 to 90%. This is consistent with the spatial signature RAC study conducted earlier in this chapter in Section 4.4.2. Use of forecasting allows the base station to have spatial signature estimates that are around 30% with respect to the actual values. Based upon the work described in [27], this improvement can lead to appreciable performance increases in downlink beamforming.

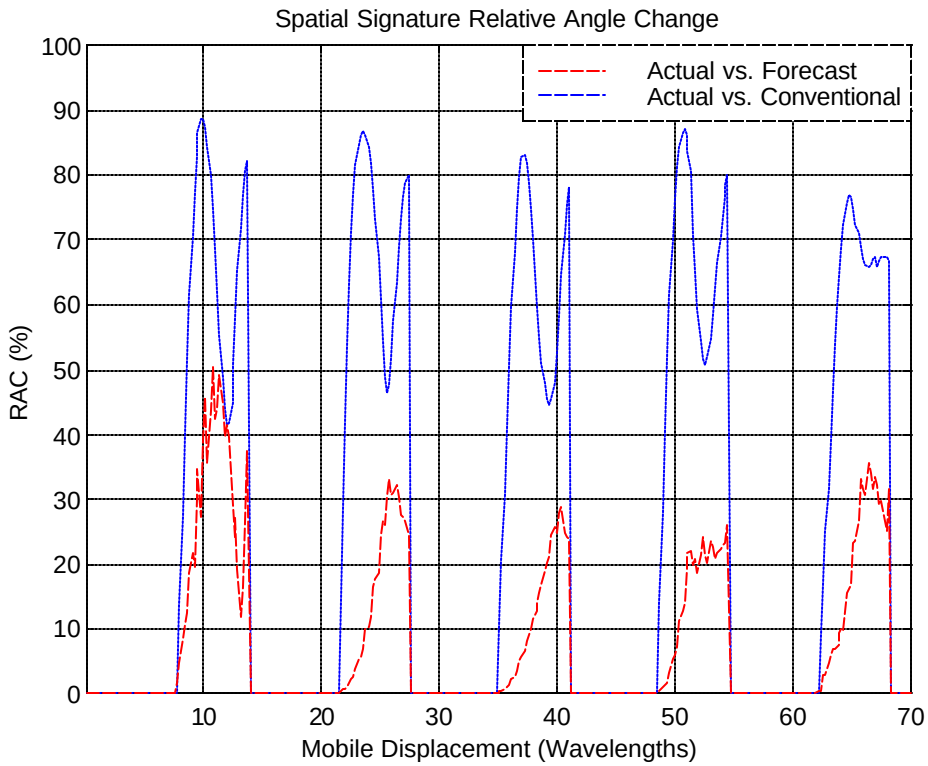

Figure 4.18 – Spatial Signature Prediction Performance Illustration for Sixth Street Trajectory

Figure 4.19 shows the average RAC at various levels of step-ahead forecasts for the eighth street trajectory. This graph illustrates the average performance of the prediction method over all 200 downlink periods of the user trajectory. As this graph shows, after six wavelengths of mobile user displacement, on average, the forecasted spatial signatures still have less RAC with actual values as do the conventional spatial signatures. However, predictions this far ahead into the future have an RAC with values that begin to converge to the RAC using the conventional approach.

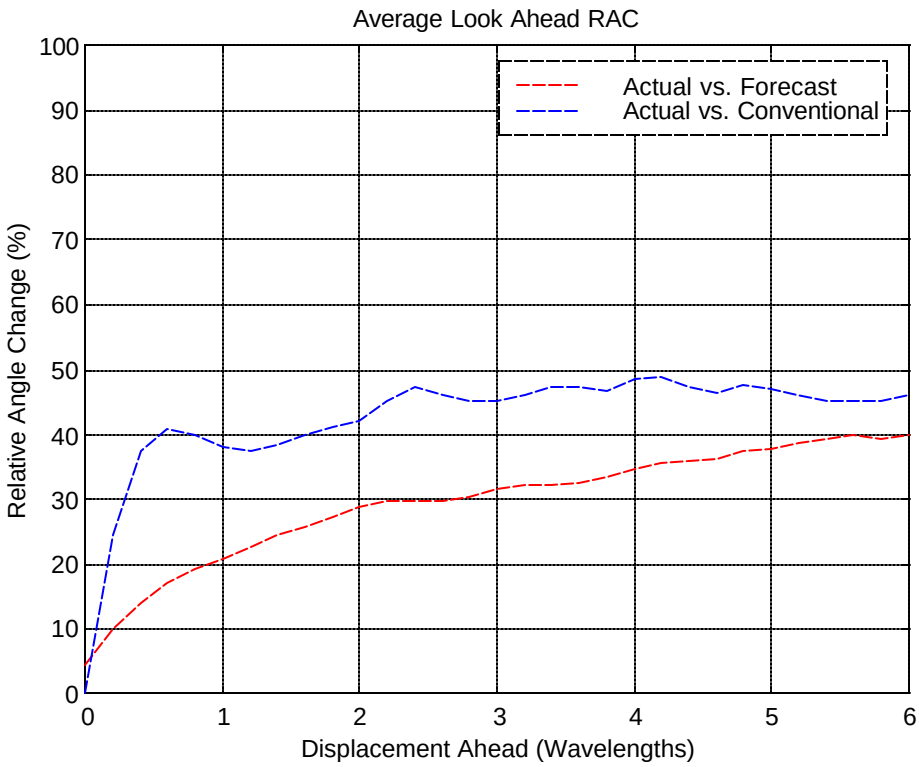

Figure 4.19 – Average Look Ahead Performance of Spatial Signature Prediction in Eighth Street Trajectory

Figure 4.20 shows the same performance graph as Figure 4.19 for the seventh street trajectory. Recall that this trajectory, unlike the sixth and eighth street trajectories, is LOS with the base station antenna array. This is reflected in the graph by the slower increase in spatial signature RAC between actual and conventional values. This is consistent with the spatial signature results discussed for LOS scenarios in Section 4.4.2. This graph also shows the forecast spatial signatures are slower to reach high levels of RAC with actual values than are conventional signatures. However, in these LOS scenarios, the work of [27]

shows that the even the level of spatial signature RAC corresponding to conventional values is not large enough to causes significant degradations in SIR during downlink beamforming. Thus, the performance increase illustrated in this graph is not as significant as it is for the NonLOS scenarios.

Results for all user trajectories are summarized in Table 4.7. As the table shows, on average, spatial signature prediction provides an appreciable improvement over the use of conventional spatial signature estimates during downlink. These improvements, particularly in the NonLOS scenarios will translate to improved performance during downlink beamforming [27].

Scenario	Average SS RAC Actual vs. Conventional (%)	Average SS RAC Actual vs. Forecast (%)
Sixth Street	49.2	37.7
Seventh Street	31.6	17.8
Eighth Street	43.1	29.4

Table 4.7 – Summary of Spatial Signature Prediction Results

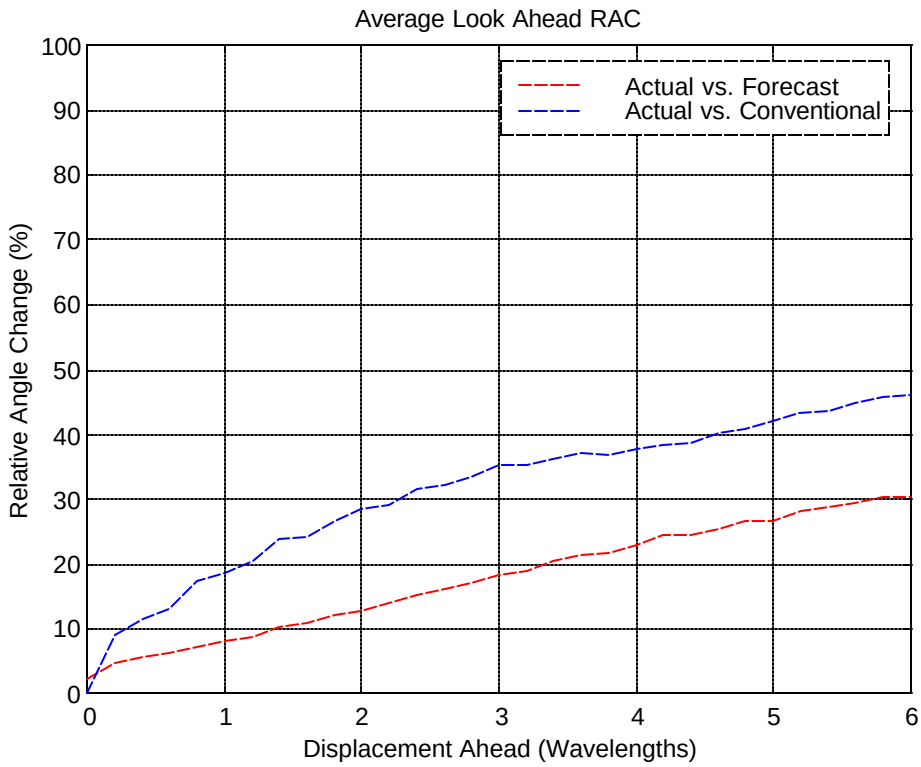

Figure 4.20 – Average Look Ahead Performance of Spatial Signature Prediction in Seventh Street Trajectory

4.5 – SUMMARY

A significant contribution of this work has been the development of a hybrid ray-tracing / moment method simulation tool for SDMA systems. This tool allowed small-scale vector channel effects to be studied in this chapter. Power-delay and power-angle profiles were developed for generic urban scenarios as well as in scenarios corresponding to an actual urban environment. The scale of delay studied was on the order of that which would be encountered in dense urban microcells. The types of power-angle profiles shown illustrated the urban

canyon effect that tended to make signal components transmitted from the mobile user arrive at the base station along certain angular corridors. The determination of these corridors has implications for the type of array geometry used in a particular cells. In addition to insights on the urban vector channel provided by these angle and delay profiles, insight was also gained in the types of ray tracing mechanisms needed to simulate particular urban scenarios. Specifically, the use of diffraction mechanisms was found to become very important when considering scenarios in which mobile users were shadowed by buildings.

Vector channel quantities of interest were also introduced in this chapter. The application of a simulation system to consider these facets of SDMA system performance through generic situations to verify conclusions from field measurements is a contribution of this research to the literature. Spatial signature relative angle change and downlink beamforming simulations were examined in this chapter for generic and realistic urban scenarios. Variation of spatial signatures and downlink beamforming scenarios generated using the novel hybrid MoM/ERT simulation system agreed with measurement data taken using a smart antenna testbed. Furthermore, relative angle change simulations in generic environments led to insights into the structure and validity of the spatial signature model discussed in Chapter 2. These relative angle change scenarios were used to make comments about the nature of multipath fading in the urban vector channel. Specifically, the transition of a mobile user from LOS to NonLOS or vice-versa caused particularly high levels of RAC that subsequently lead to appreciable losses in downlink beamforming performance. These LOS to NonLOS transitions

were shown to have slightly worse RAC performance than other NonLOS situations.

Several downlink beamforming methods were studied in this chapter. It was shown that the PseSS method nearly always outperformed the other methods for various configurations of mobile users in different environments. The other methods generally performed solidly, with no other method clearly superior in all scenarios. Downlink beamforming studies also showed a correlation between loss in accuracy of the spatial signature estimates and decreased SIR performance.

Spatial signature forecasting was also examined in this chapter using a novel vector autoregressive approach. The model was developed from a linear regression system using a Kalman filter to recursively update the estimated model coefficients and avoid unnecessarily large matrix inversions. This savings in computations makes this method more attractive for real-time implementation in future base stations. This prediction method generated forecasted spatial signatures that always outperformed the last-known spatial signatures from uplink that would otherwise be used during downlink. This increased performance is particularly important in NonLOS scenarios where current spatial signature estimates are more critical. The performance increase, demonstrated in terms of spatial signature RAC, helps to quantify the overall improvement that forecasting would provide during downlink beamforming.

Chapter 5 – SDMA System Planning

5.1 – BACKGROUND INFORMATION

In this dissertation, there are cellular network level issues that were studied at a higher level than the previous research topics. The impact of smart antenna technology was specifically examined on issues such as cell site design and mobile user handoff. This is increasingly important as smart antenna technology becomes more accepted for use in next generation cellular systems. While it would be simple to introduce the basic use of antenna arrays into next generation cellular systems by simply replacing conventional base station antennas, techniques to maximize their performance are a complicated issue.

The optimal allocation of basic resources such as base station hardware and channels of radio spectra in a certain coverage area is the central issue in system-level cellular communications [46,47]. The criteria by which these strategies are assessed involve maximizing overall system capacity and reliability while effectively managing the amount of interference between the mobile users. Obviously, all of the technical solutions to these system level problems must be addressed in an economically sound manner.

A cell is the region over which a single base station provides coverage. The coverage region of a particular cell is the geographic region over which the power received by a mobile user is above a certain threshold. In earlier generation cellular communications systems, cells were considered that were on the order of kilometers in radius. However, as user demand increased, the power

transmitted by each base station was lowered and bandwidth resources were reallocated more often to smaller cells. These small cells, referred to as microcells, have coverage radii on the order of hundreds of meters [48,49]. There are still smaller cells, referred to as picocells, which cover areas corresponding to individual buildings or floors of a building. However, the focus of this chapter will be placed on urban microcell environments.

The ability of antenna arrays to perform directional transmission and reception could raise the question how to most effectively deploy base stations and design cells using smart antenna techniques in a particular environment. However, since existing cellular infrastructure and base station deployment is often dictated by non-technical issues (e.g. economics, zoning, etc), research must consider the upgrade of existing networks to systems making use of smart antenna technology. This is the central issue of the papers by Aroudaki [50] and Kronestedt [51].

Another issue that needs to be considered with cellular system planning is call handoff as a mobile user moves from one cell to another. Handoff scenarios are dependent upon the propagation environment of the cell, the amount of interference from other users and base stations, and the distance of the mobile user from the base station. In general, handoffs occur when time-averaged signal power level, measured by mobile user or base station, drops below a certain threshold value.

In summary, the addition of SDMA technology into existing cellular communication networks may have the following advantages [50]:

1. Cell capacity increase – Improved frequency reuse made possible through SDMA technology can allow the number of channels in a cell to be increased.
2. Spectrum savings – Improved frequency reuse may allow current demand to be met with fewer channels.
3. Interference reduction – Adaptive SDMA technology may allow downlink interference seen by a given mobile user (from the signals intended for the other mobile users) to be reduced significantly.

Vector channel propagation was considered during individual mobile user trajectories through typical urban environments in Chapter 4. These simulations were run at a spatial resolution on the order of fractions of a wavelength and thus considered small-scale channel effects. In this chapter, the hybrid MoM-ERT system from Chapter 4 is applied to consider large-scale propagation and vector channel statistics in urban microcells. Specifically, power-delay and power-angle plots, spatial signature relative angle change, and downlink beamforming techniques discussed in Chapter 4 for individual mobile trajectories will be considered in a statistical sense in simulations corresponding to microcells in downtown Austin, Texas (Sections 5.31-5.3.3). The architecture of these urban microcells along with issues related to mobile user handoff between microcells will also be considered in this chapter in Sections 5.3.2 and 5.3.4.

5.2 – APPROACH

Past studies of SDMA system planning rely on statistical channel characterizations that do not directly consider the mobile environment or mutual coupling effects [48,50-59]. The focus of these studies is geared more towards high-level simulation of system capacity, outage probabilities, and bit-error rate. Only the study by Dam [60] considers a realistic channel through site-specific field measurements using antenna array hardware. The system measured by Dam was not fully adaptive, relying instead on a combination of fixed and switched beams. Thus, the focus of this dissertation research is to consider the intermediate topics between existing work in low-level channel simulation and high-level capacity studies.

The electromagnetic ray tracing research topic discussed previously is an ideal tool for studying SDMA planning issues. ERT has predominantly been used in the past for system planning studies [28, 30, 49]. Thus it is a natural extension of work of this kind to apply these tools to the study of SDMA systems. For this reason, two Virtual Reality Markup Language (VRML) visualization tools have been developed on top of the underlying hybrid MoM-ERT system for the explicit purpose of system planning. The first of these tools displays the geometric ray tracing solutions for a mobile user moving through a particular environment. This helps to provide some intuition for the time varying nature of the vector channel as a mobile user travels. A screenshot of this program using data from downtown Austin simulations is illustrated below in Figure 5.1.

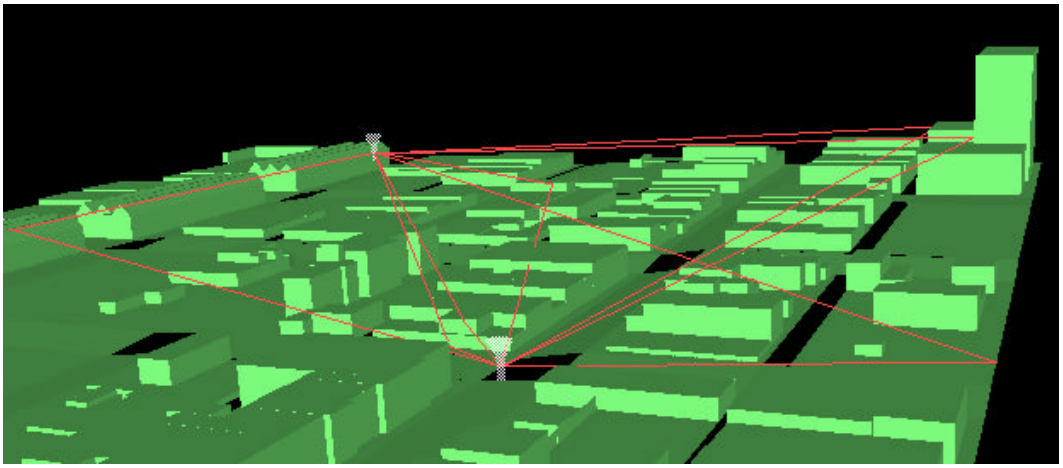

Figure 5.1 – VRML Ray Solution Tool Screen Capture

The second related VRML tool displays the power received at each point in an ERT model due to a base station at a particular location. This power display is dynamic; the effect of changing the beamforming weights applied to the antenna array elements is displayed.

These tools along with others, are used to study SDMA planning issues. Whereas past studies of ray tracing applied to system planning focused on received power alone, more is required to study SDMA systems. For example, issues like direction of arrival and spatial signature statistics are examined in urban microcell environments. This has implications for the downlink beamforming algorithms and continuing studies in uplink spatial signature prediction discussed in Chapter 4. Downlink beamforming algorithms, in general, are very difficult to study in realistic environments. Thus, the ability to simulate their performance in urban environments and display the results in an intuitive form is of great value.

More fundamental questions also need to be studied using this suite of tools. Specifically, the issue of using the antenna array to produce fixed beams, adaptive beams, or a hybrid strategy needs to be addressed. As an example of a hybrid scheme, consider a situation in which the antenna array maintains a fixed beam in a particular direction to serve a large number of users traveling along a main highway. This array could also have adaptive beams in other directions to serve a small volume of users in the less traveled area around the cell.

Handoff issues also need to be considered between base stations making use of SDMA. Another related question is the idea of fixed versus variable cell shape. The difference between these two schemes is illustrated below in Figure 5.2. Many of these studies require traffic and site specific data to be taken into account. The figure shows a fixed cell architecture, in which base stations cover a particular mobile user if they are in a certain geographic area and the borders between regions is determined by the amount of power transmitted by each base station. A variable cell shape is also illustrated in Figure 5.2, which shows how directional transmission can be used by base stations in surrounding cells to serve users who would otherwise be in the geographic region corresponding to another base station. This could potentially allow the load encountered by overloaded cells to be reduced through coordination with surrounding cells.

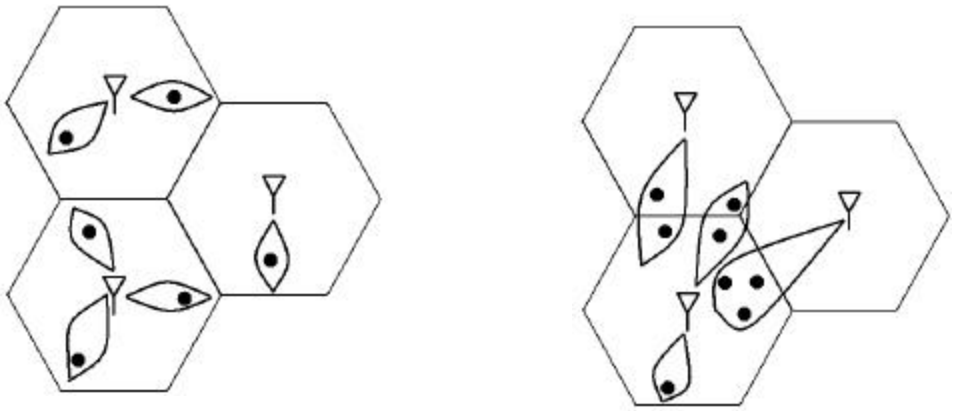

Figure 5.2 – Fixed Cell Shape (Left) versus Variable Cell Shape (Right)

5.2.1 – Microcell Scenarios

There were five microcells that were tested in this study corresponding to different geographic regions in downtown Austin, Texas. Each microcell covers a 4 x 4 square block area of the city. The base station antenna array was a uniform circular array with half-wave dipole elements operating at 1.8 GHz. The base station antenna array was located 20 meters off of the ground at the center of each microcell. At this height, the array was below the rooftops of many of the buildings. However, the buildings in this particular model was not as tall as the simulations / measurements described in [49,61] corresponding to Manhattan. These five microcells will be referred to as "Northeast", "Northwest", "Southeast", "Southwest", and "Center", which describes the portion of downtown Austin that each microcell covers. Each microcell had a diameter of approximately 500 meters. The Austin simulations described in Chapter 4 correspond to the Center microcell. Field measurements, described in [62], were also performed in this microcell.

Simulations were performed on a grid overlaid on the city streets of each microcell. The density of grid was chosen to allow simulations to be performed approximately every 5 square meters. Each of these possible mobile user positions was simulated 1.5 meters off of the ground surface. The material properties match those described in Chapter 4.

5.3 – RESULTS

Section 5.3.1 expands upon the results for power-delay and power-angle profiles given in Chapter 4. Specifically, in this section, statistical characterizations are made in the various urban microcells to aid in system planning. Power distribution plots over the microcells is the topic of Section 5.3.2. In this section, the benefit of using smart antenna techniques will be quantified. In addition, power distributions during a handoff scenario will be considered. Section 5.3.3 studies spatial signature RAC, introduced in Chapter 4, at a large scale over the microcell. Section 5.3.4 considers the application of the downlink beamforming techniques introduced in Chapter 2 to mobile users in the microcell. Finally, Section 5.3.5, applies the MoM characterization techniques of Chapter 3 to study the effect of the base station tower on the overall array radiation pattern.

5.3.1 – Power-Delay and Power-Angle Statistics

In Chapter 4, power-delay and power-angle profiles were considered for individual trajectories of mobile users in generic urban scenarios. These profiles showed a tendency for rays to have delays on the order of 0.5 μs after the arrival

of the dominant multipath component. This value is consistent with delays incurred by radiation traveling on the order of 100-200 meters.

Figure 5.3 shows a histogram of the ray delays for a representative urban microcell in downtown Austin. To develop these plots, power-delay profiles, similar to the ones shown in Section 4.4.1 are generated for each mobile position on the grid of positions simulated in the urban microcell. All rays that were more than 40 dB below the dominant signal component were discarded [61] and the resulting ray delays were collected on the histogram over all positions. By considering ray delay data relative to the time of arrival of the dominant signal path, the effect of mobile user position in the microcell is removed.

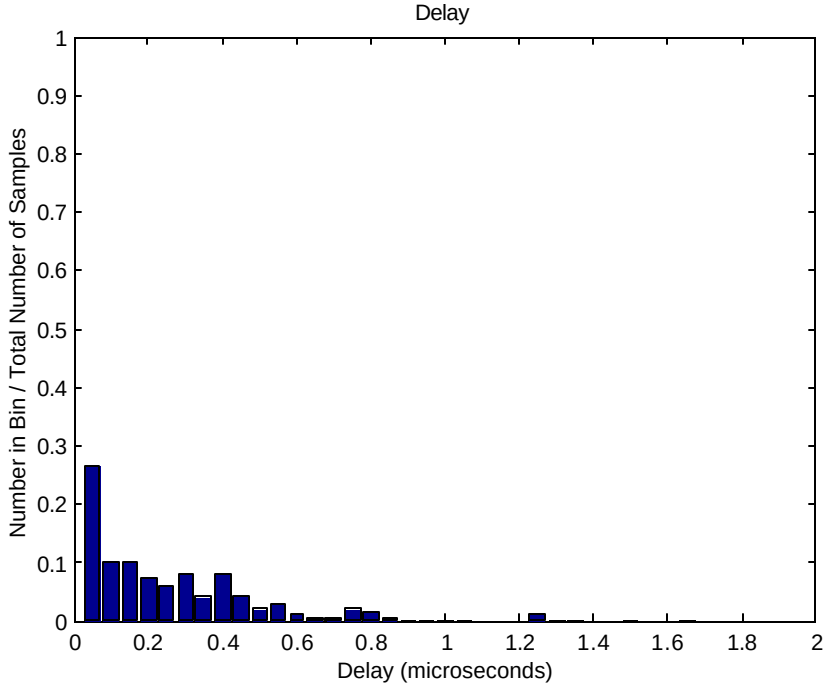

Figure 5.3 – Histogram of Ray Delay Relative to Dominant Signal Path Component at All User Positions in the Central Microcell

As Figure 5.3 shows, nearly all of the received rays have delays that are less than 0.8 μs. Knowledge of these parameters is crucial for system design since it specifies the level of inter-symbol and inter-chip interference that will be present in a system. For example, the chip rate in an IS-95 system is 1.22 Mchips/second, which corresponds to a chip duration of 0.8 μs. The delays simulated in this microcell of downtown Austin, are smaller than similar values for downtown Manhattan reported in [61]. However, as the author of [61] reported, these larger delays can be attributed to the particularly tall buildings in that mobile environment.

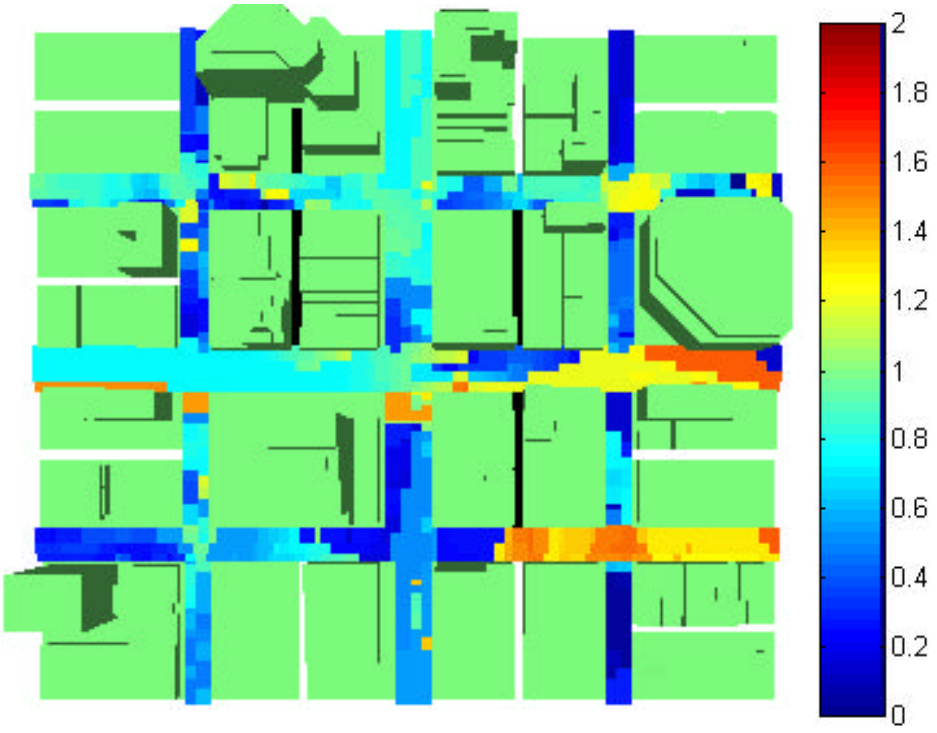

Figure 5.4 – Ray Delay Overview Plot in Central Microcell (in μs)

Figure 5.4 addresses the issue of how the varying delays are distributed in the microcell. Specifically, this plot shows the maximum ray delay at each mobile user position. As mentioned in Section 5.2.1, the base station in the microcell is at the center of the grid of buildings. The delays tend to be in the 0.6 μs to the 0.8 μs range in the LOS and nearly-LOS areas corresponding to the left side of the cell. The higher delays around 1.5 μs tend to be in the areas surrounded by the larger buildings in the cells.

More interesting results, from an array signal processing perspective, can be found by considering the distribution of ray angles received in the urban microcell simulations. Similar to the ray delay distribution simulations, rays were discarded which were 40 dB down from the dominant signal component. The distributions of angles were considered in two different contexts. In the first, the distribution of angle was measured relative to the dominant signal path component. A representative figure illustrating this type of angle distribution is shown for the Southwest microcell in Figure 5.5.

Figure 5.5 shows that multipath signal components in this microcell are often centered about the dominant signal component. This is a significant observation in that it has implications for antenna array design. Specifically, it implies that when dominant signal energy is received in a particular direction, it is not as important to search far from this angle when looking for resolvable multipath signal components. It also implies that the resolution of DOA algorithms used in direction finding applications needs to be high enough to resolve multipath signal components that do not have much angular separation.

Further, even if super-resolution DOA algorithms (e.g. MUSIC) can resolve these multipath components, DOA-based downlink beamforming algorithms may not necessarily be able to synthesize radiation patterns with directional peaks that are so close given a particular array geometry.

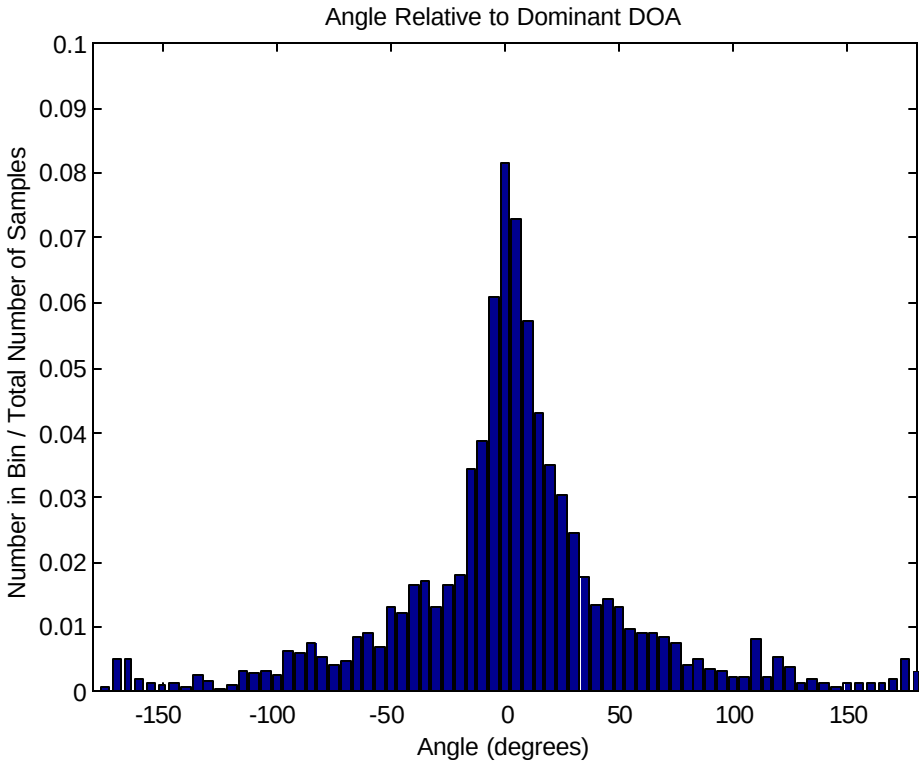

Figure 5.5 – Histogram of Ray Angles Relative to Dominant Signal Component in the Southwest Microcell

The second angular distribution that was considered in this chapter is the distribution of absolute ray angles. These angles are measured relative to the coordinate system of the array, rather than with respect to any particular signal component. Figure 5.6 shows the representative histogram of this type corresponding to the Southwest and Central microcells.

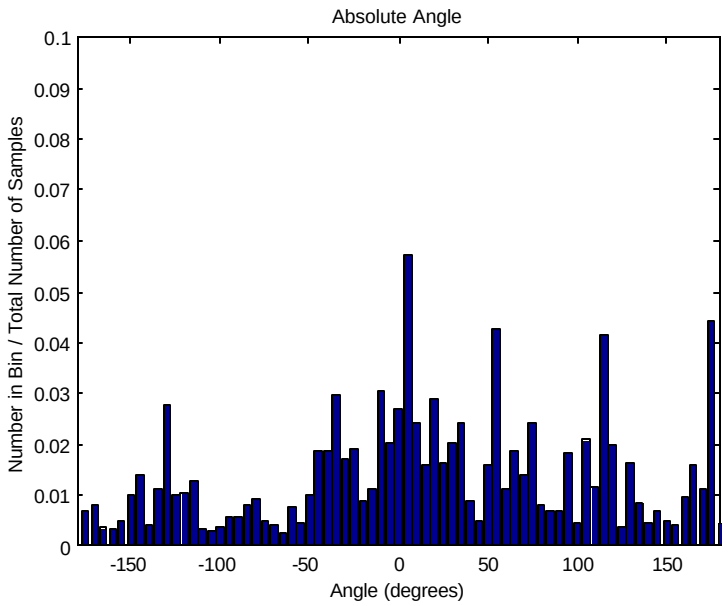

(A)

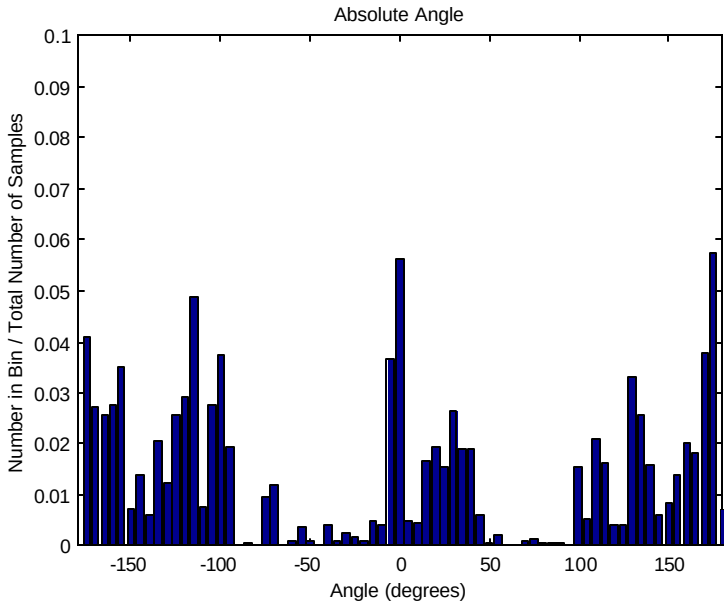

(B)

Figure 5.6 – Histogram of Ray Angles Relative to Array Coordinate System in the (A) Southwest Microcell and (B) Central Microcells

The plots in Figure 5.6 show a banded structure in the DOAs of signal components incident to the array. Figure 5.6B, in particular, is consistent with the urban-canyon phenomena discussed in Chapter 4. Combined with the results of Figure 5.5, further comments can be made regarding the necessary capabilities of future SDMA base stations. The banding structure limiting incident signal energy to certain corridors of incidence to the array, shown in Figure 5.6, motivates the use of smaller subarrays each covering certain angular sectors. The tight distribution of DOAs around the dominant signal component shown in Figure 5.5 further implies that each of these subarrays may not often need to interact with other subarrays.

5.3.2 – Cell Architecture

The geographic region over which the received power exceeds a given threshold determines the exact shape of the microcell covered by a particular base station. This threshold power is chosen to allow for minimum system SNR and SIR requirements. In a microcell where antenna arrays are introduced, but no smart antenna algorithms are implemented, the simplest solution would be to have each element uniformly excited to create an omni-directional radiation pattern. A more sophisticated solution would be to introduce smart antenna algorithms for downlink beamforming when transmitting to different portions of the cell. Table 5.1 summarizes the average power received at all simulated points in the microcells by using the simple uniform excitation as well as more complex DOA-based and SS-based downlink beamforming techniques (DomDOA and SS method respectively from Chapter 2):

Microcell	Uniform		DomDOA		SS	
	Mean (dB)	Std	Mean (dB)	Std	Mean (dB)	Std
Central	-66.4	21.1	-62.2	21.9	-58.0	21.8
Northeast	-57.9	17.5	-53.8	17.2	-49.7	17.2
Northwest	-57.6	21.6	-54.0	20.5	-50.2	20.6
Southeast	-51.0	9.3	-46.8	9.1	-42.5	8.9
Southwest	-56.2	18.2	-52.2	15.8	-48.5	16.1

Table 5.1 – Summary of Microcell Power Statistics

As the table shows, use of both DOA-based and SS-based downlink beamforming provides a significant improvement over a simple uniform array excitation. Specifically, the DomDOA method provides approximately 4 dB over uniform excitation and the SS method provides about 7.5 dB over uniform excitation. This increased performance comes at the expense of increased smart array processing since DOA / SS estimation at each mobile user location would be required.

Figure 5.7 shows the power distribution in the Southwest microcell when using the SS method for beamforming. As expected, the power is higher in the sections of the model LOS with the antenna array. In even the closer NonLOS sidestreets, the power level is relatively low. The shape of the cell is generally diamond-shaped about the base station array, with main axes determined by the LOS streets in the cell. This is consistent with measurements and simulations discussed in [49,63] for urban microcells making uses of conventional antenna base stations.

The shape of the power contours obtained with the SS method is similar to the power contours of the DomDOA and uniform excitation methods. However, the power levels are uniformly higher for the SS method over the DomDOA method. Similarly, the DomDOA method has higher power levels than the uniform excitation method.

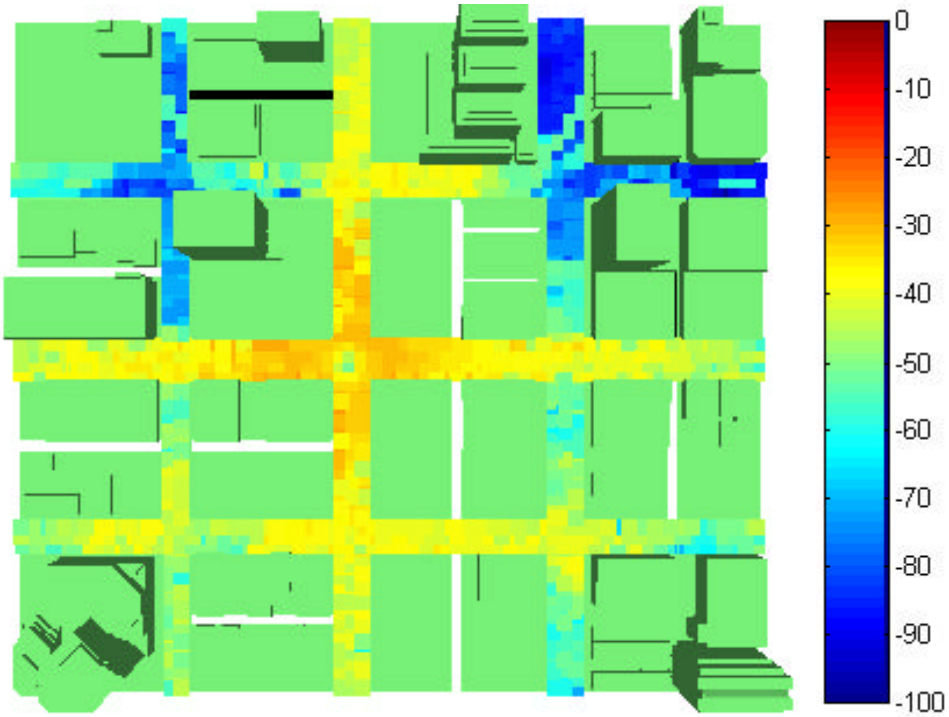

Figure 5.7 – Southwest Microcell Shape using SS Downlink Beamforming Method

The benefit of using a smart antenna array follows from the increase in power through use of SS and DOA based beamforming. By paying for the increased processing needed by these methods, the contours defining constant levels of power will be pushed away from the center cell. This increase makes the

geographic region covered by the cell larger and reduces the number of cells necessary in a particular environment.

This increase in signal power through use of can also be used to aid in handoff scenarios by allowing for variable cell shape. Variable cell shape, illustrated in Figure 5.2, allows one base station to service a mobile user who would otherwise be in the geographic region covered by another cell. To illustrate this, consider a handoff scenario between one microcell and other. Under normal circumstances, corresponding to the situation when both base stations are uniformly excited, handoff will occur at a given geographic location between the two cells. However, if one of these base stations uses DOA or SS-based downlink beamforming to specifically target a mobile user, by the results of Table 5.1, this will boost the signal received by that base station by anywhere between 4 and 8 dB. This has the effect of extending the geographic area covered by a particular base station. Determining when to use these downlink beamforming techniques to increase signal power and change cell shape can then be made a function of the relative load of the microcells in question and the different configurations of mobile users in the cells.

5.3.3 – Large Scale Spatial Signature Variation

Chapter 4 showed spatial signature variation during trajectories of length on the order of wavelengths of mobile users displacement. These scenarios gave insight into the validity of the spatial signature model. They also illustrated how inaccurate spatial signature knowledge could lead to losses in downlink beamforming performance. In this section, we consider spatial signature variation

over regions corresponding to entire urban microcells. These simulations give insight into the uniqueness of the superposition of steering vectors that make up the spatial signature (discussed in Chapter 2). Since spatial signature RAC variation can be translated to particular multipath fading environments (as done in Chapter 4), knowledge of the distribution of RAC can yield information about the microcell vector channel.

Figure 5.8 shows the overall histogram of spatial signature RAC in the Southwest microcell. The graph was generated by considering the RAC between all pairs of points on the grid of simulated positions. The graph shows that in three-quarters of the cases, the spatial signature RAC is 80% or more. Referring the definition of spatial signature RAC in Chapter 2, along with the discussion in [23], this implies that spatial signatures are not very correlated with one another in this environment. This characterizes the environment as being predominantly NonLOS and motivates the need to update spatial signatures often as users move through the microcell. It also motivates the use of the spatial signature prediction algorithm considered in Chapter 4.

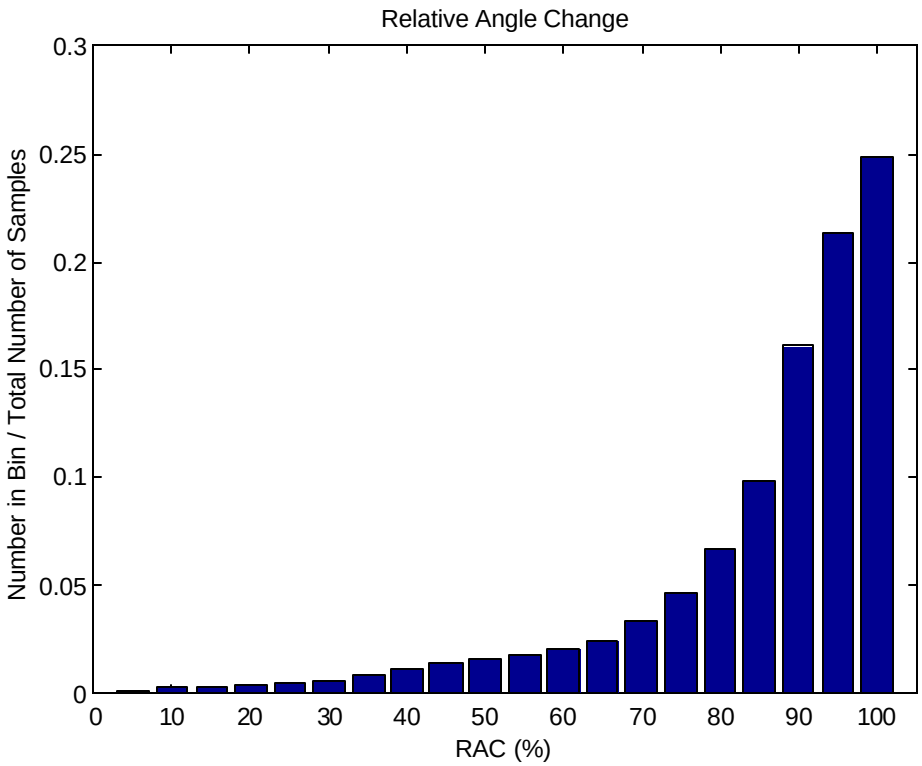

Figure 5.8 – Cumulative Frequency Histogram of Spatial Signature RAC in the Southwest Microcell

Another component to large-scale spatial signature RAC study is the effect of position in the cell on spatial signature RAC. This is illustrated in Figure 5.9 for the Southwest microcell. The two subplots show the contours of spatial signature RAC over the entire microcell relative to the spatial signature in an LOS intersection of the model (Figure 5.9A) and a NonLOS intersection (Figure 5.9B).

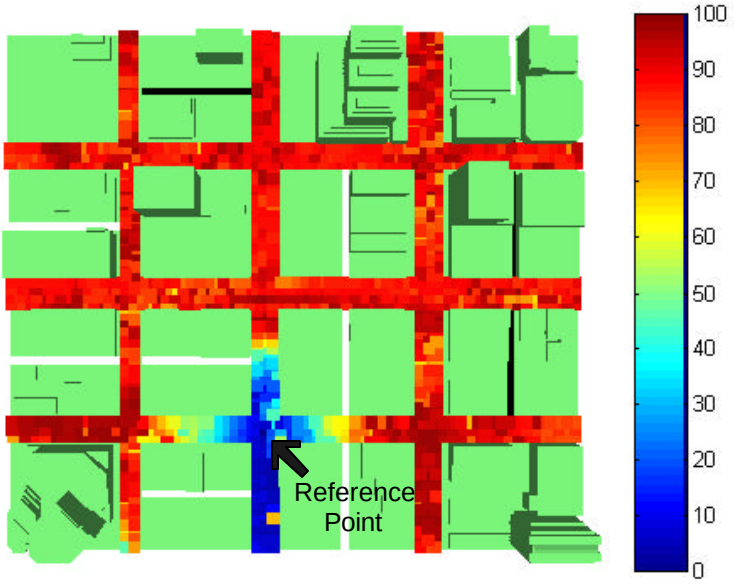

(A)

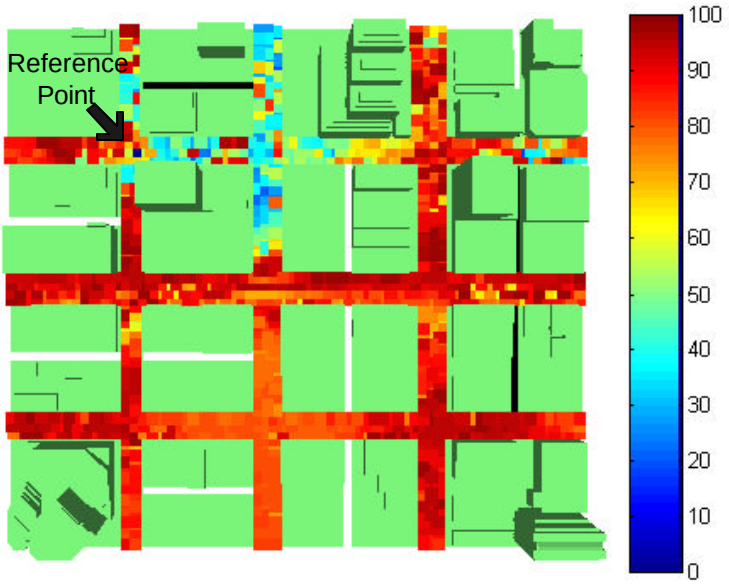

(B)

Figure 5.9 – Spatial Signature RAC Distribution in Southwest Microcell for (A) LOS Position and (B) NonLOS Position

Figure 5.9 shows that there is a definite relationship between spatial signature RAC and proximity in the microcell. In Figure 5.9A, while the RAC approaches 80-90% over much of the microcell, there is a region around the LOS reference point at which the RAC remains low around 15%. As positions are considered further from this point up and down the street corresponding to a LOS region as well as the NonLOS cross street (LOS and NonLOS relative to the base station), the RAC steadily increases. This increase is greater on the NonLOS cross street than it is in the LOS area. The intuition behind this behavior is that the dominant multipath signal component for these locations remains relatively constant in this region. This makes this situation analogous to the "LOS + Dominant Multipath" situation considered in Section 4.4.2.

Figure 5.9B shows the same results for a NonLOS reference point. This point is behind a large building blocked from the base station. The shape of the RAC contours in Figure 5.9B show that the multipath environment at the reference point is similar to that of the LOS intersection one block to the west. This implies that the signal components are likely traveling down this intersection to reach the NonLOS reference point. The contours show that there is relatively low RAC in this intersection, which means that the spatial signatures at the reference point and in this intersection share a subset of steering vectors. These common steering vectors correspond to common multipath components when users at both locations transmit to the base station array.

5.3.4 – Array Omni-Directional Pattern Synthesis

Antenna arrays deployed in next-generation base stations may not necessarily be mounted at the top of the cellular tower. This side-mounting is not governed by technical issues, but rather through mechanical or zoning constraints. This was the case in the deployment of antenna arrays in wireless local loop base stations described by Xu [64]. In this situation, the tower blocks the omni-directional control signals transmitted by the array, resulting in service degradation to users in particular angular sectors.

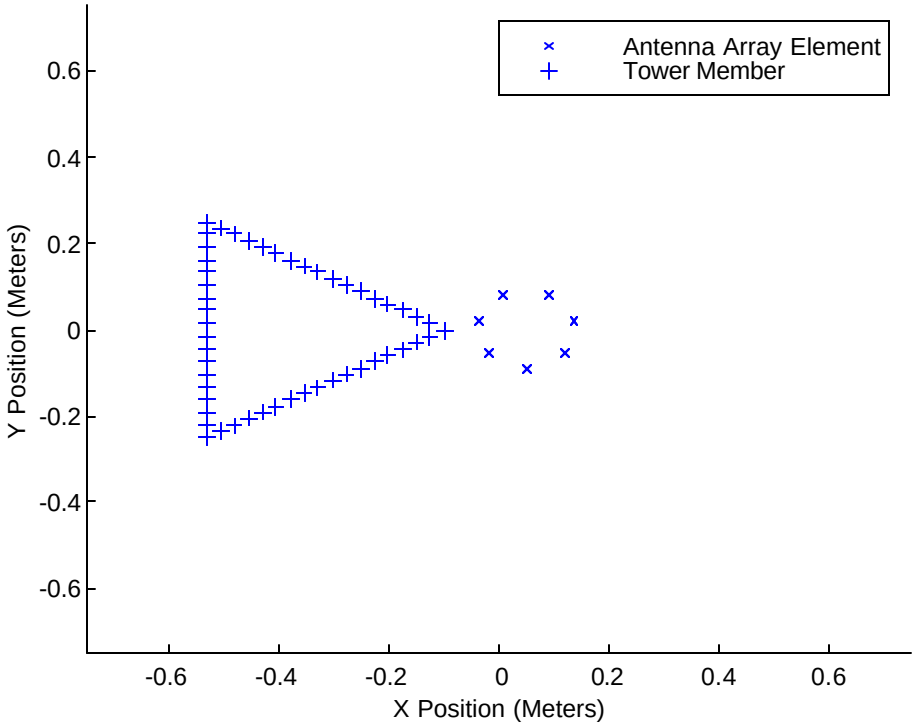

Figure 5.10 – Antenna Array and Tower Material Positions

In Chapter 3, MoM simulation was used to compensate for the electromagnetic interaction between antenna array elements. This technique can be extended to compensate for local scattering occurring near the array. Figure 5.10 illustrates an extreme case of this kind of local scattering. The figure shows a cross-section from above of antenna array element and tower material positions. The tower is modeled as a series of wires making up a triangular prism. The wires and the prism are aligned with to be in the same direction as the orientation of the array elements. The array elements are each half-wave dipoles transmitting at 1.8 GHz in an array that is 9 cm in diameter. Wires that are several wavelengths long represent the tower.

Even though the previous sections have shown applications where it is desirable to have the array transmit directionally, in this section, we consider omni-directional transmission of control signals covering the entire cell area. The tower has the effect of severely attenuating the signals sent towards it, creating the overall array radiation pattern shown in Figure 5.11. This pattern is the result of a uniform excitation to the array elements. The two nulls at 160° and 200° will cause users in these angular sectors to not be served as well as users in other sectors.

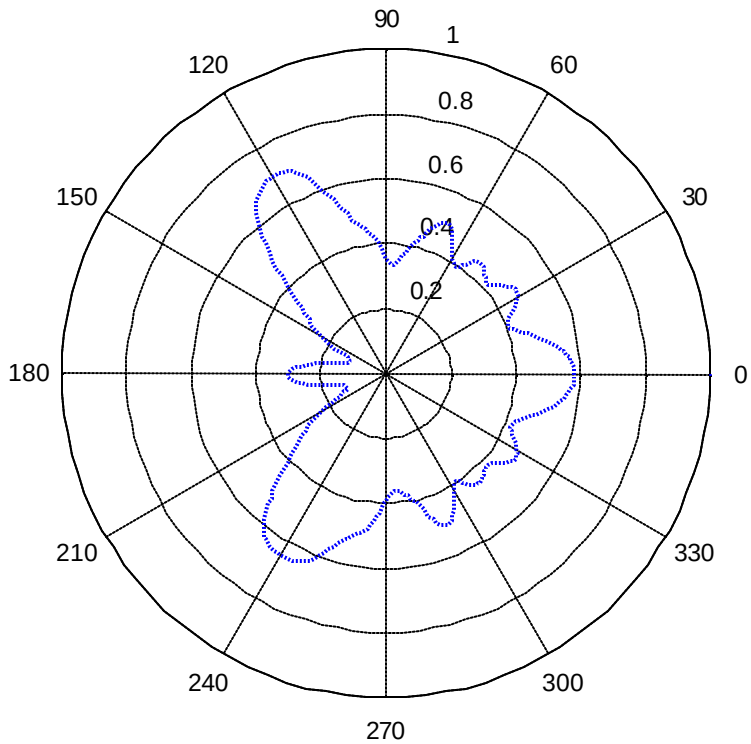

Figure 5.11 – Non-Optimized Omni-Directional Array Radiation Pattern in Presence of Blocking Tower

Non-linear optimization was used to determine the array excitation needed to synthesize a better omni-directional radiation pattern. Given the radiation patterns of the ith array element, $\vec{\mathbf{E}}_i(\theta)$, generated using NEC simulations described in Chapter 3, the problem is to find the weight vector, $\vec{\mathbf{w}}$, such that the objective function in equation (5.1) is minimized. $\vec{\mathbf{E}}_i(\theta)$, is a vector containing the 360 (θ=1,…360) E-field values characterizing the transmission pattern of the ith array element. The ith element (i=1,…M) of the weight vector represents the

complex value used to scale the ith array element pattern. These individual element patterns are then summed to give the total array radiation pattern.

$$\vec{\mathbf{w}}^{*} = \arg\min_{\vec{\mathbf{w}}} \frac{\operatorname{std}_{\theta}\left[\left|\sum_{i=1}^{M} w_i \vec{\mathbf{E}}_i(\theta)\right|\right]}{\operatorname{mean}_{\theta}\left[\left|\sum_{i=1}^{M} w_i \vec{\mathbf{E}}_i(\theta)\right|\right]} \tag{6.1}$$

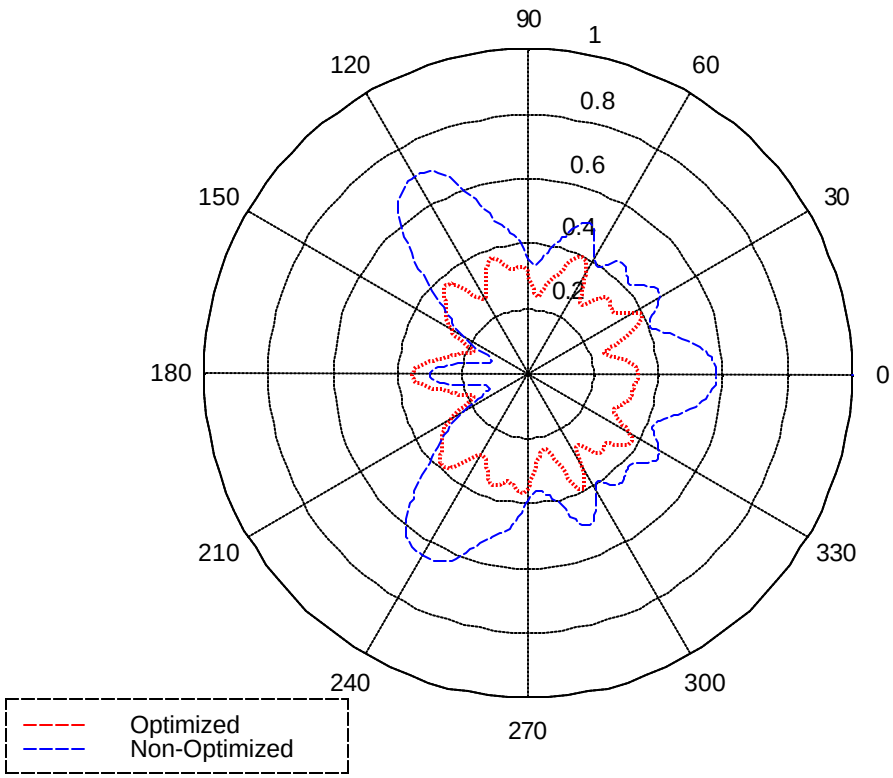

Figure 5.12 – Omni-Directional Array Radiation Pattern in Presence of Blocking Tower

This multivariate optimization problem was solved using the Fletcher-Powell optimization technique [65]. The resulting optimized radiation pattern is shown along with the non-optimized pattern in Figure 5.12. The nulls are still present in the radiation pattern, but the distance from peak-to-null has been

greatly reduced. Thus, the goal of serving users in all sectors of the base station coverage area is fulfilled. However, as the figure shows, this comes at the cost of reducing the strength of the field in directions where there had previously been ample gain.

With this technique we can further consider the cell-architecture issue from Section 5.3.2. In 5.3.2, the microcell power contours with uniform excitation, DOA, and SS beamforming, were found to be diamond-shaped with main axes determined by the LOS streets. We can apply the pattern synthesis algorithm to the fields in a rectangular path around the base station array instead of the individual element radiation patterns. This rectangular path goes down the center of the streets determining the boundary of a 2 x 2 city block area centered about the microcell base station. The new optimization problem is given in equation (5.2) and Figure 5.13 shows the resulting power distribution over the microcell with the optimized weights.

$$\vec{\mathbf{w}}^{*} = \arg\min_{\vec{\mathbf{w}}} \frac{\operatorname*{std}_{\text{Path}}\left[\left|\sum_{i=1}^{M} w_i \vec{\mathbf{E}}_i(\text{Path})\right|\right]}{\operatorname*{mean}_{\text{Path}}\left[\left|\sum_{i=1}^{M} w_i \vec{\mathbf{E}}_i(\text{Path})\right|\right]} \tag{5.2}$$

The figure shows that the optimized weights reduce the power levels received in each of the LOS intersections of the microcell to a level closer to that of local NonLOS portions of the corresponding streets. This changes the effective cell shape from a diamond to a shape that more closely resembles square. However, this flexibility in cell shape comes at the loss in average power of the entire microcell area of 4 dB. There is a definite limit on the capability of the

array to drastically change the power distribution over large areas introduced due to the fact that array elements are so close together (i.e. less than half a wavelength). However, this is required for other components of smart antenna system operation.

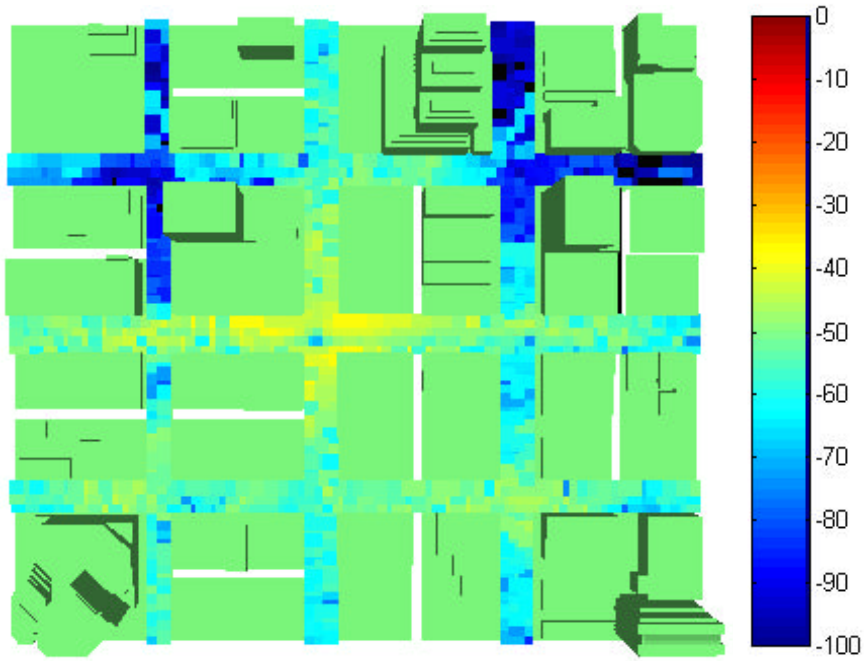

Figure 5.13 – Southwest Microcell Shape with Optimized Beamforming Weights

5.4 – SUMMARY

The focus of this chapter was on vector channel propagation characteristics in urban microcells. The first set of results showed power-delay and power-angle statistics over the group of simulated microcells. The statistics associated with power-delay are significant because they characterize the amount of inter-symbol and inter-chip interference that will be present in the system. A delay-over diagram was also generated which characterizes the level of delay that

will be encountered in different portions of the microcell. Power-angle statistics were significant because of the implications for array geometry design, DOA analysis, and downlink beamforming. Specifically, the results of this study showed a tendency for signal energy to be received along certain corridors relative to the base station. Furthermore angle statistics also showed multipath signal components to be centered about the dominant signal component. This motivates the use of sub-arrays in the microcell that are each responsible for particular sectors.

Power distribution plots were used to characterize urban microcell shape. This shape and received power statistics were further considered in the presence of DOA-based and SS-based downlink beamforming. DOA-based techniques provided a 4 dB improvement in average received power over uniform element excitation and SS-based beamforming provided an 8 dB improved. These performance increases have the effect of increasing cell size, or equivalently, reducing the amount of power necessary at the base station to retain a given cell size.

Spatial signature relative angle change statistics were also considered over the urban microcell. These statistics helped characterize the overall multipath signal environment present in the cell. They also motivate the need to update spatial signature estimates often and/or use the spatial signature prediction technique described in Chapter 4. Insights into the structure of spatial signatures at different points in the microcell were also gained from the discussion in Chapter 4.

Finally, multivariate optimization techniques were applied to study omni-directional pattern synthesis in urban microcells. This pattern synthesis was considered in two different situations. The first applies pattern synthesis to compensate for local tower scattering. This helps keep user service more uniform in all sectors of the microcell. The second applies the technique to modify cell shape. For a dense collection of urban microcells not necessarily laid out with technical issues in mind, the ability to variably adjust cell-shape has definite applications. These pattern synthesis studies were generally successful, but resulted in a loss of average power transmitted.

Chapter 6 - Conclusions

This dissertation demonstrates how electromagnetic modeling techniques can be applied to the holistic study of SDMA systems. A foundation for unifying low-level electromagnetic principles with propagation and system level concepts in communication system performance has been developed. Computational electromagnetics techniques, including electromagnetic ray tracing and the Method of Moments were used to investigate:

1. Mutual coupling characteristics
2. Radio frequency (RF) propagation statistics
3. SDMA urban microcell system planning issues

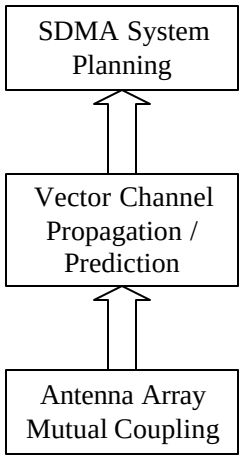

Figure 6.1 – Research Topic Hierarchy

This research considers SDMA systems at three different scales. At the lowest level, illustrated on the research hierarchy Figure 6.1, was the study of antenna array mutual coupling conducted in Chapter 3. The electromagnetics

community has long understood the physics governing antenna array mutual coupling. However, while the smart antenna community has recognized the existence of mutual coupling, there has been little work considering the quantitative effects of coupling over a wide range of communications topics. The contribution of this dissertation is the demonstration, through field measurements, of the benefits of antenna array moment-method mutual coupling compensation. Another novel aspect of this research is the demonstration of the implications of mutual coupling compensation at a higher level in communications system performance. Specifically, the role of mutual coupling in direction-finding and downlink beamforming was considered in this research. A significant contribution of this work has been the development of a hybrid ray-tracing / moment method simulation system for SDMA systems. This has allowed, for the first time, a large cross-section of SDMA-related issues to be studied that consider mutual coupling effects.

The hybrid ray-tracing / moment method simulation system was first applied to a study of vector channel propagation and prediction in Chapter 4, the middle level in Figure 6.1. Through this system, generic urban scenarios were simulated and the results compared with measurement studies made using a smart antenna testbed. The application of a simulation system to consider various facets of SDMA system performance through generic situations is a contribution of this research to the literature. These simulations allowed power-angle and power-delay profiles to be generated which allowed comments to be made on the theoretical spatial signature model of narrowband vector channel. This model

was further considered in a simulation study of spatial signature relative angle change. The performance of several downlink beamforming algorithms was also studied, verifying the results of measurement studies while also motivating the need to keep spatial signature estimates current. This led to a study of spatial signature forecasting. While this topic has been studied in the past, a novel method for prediction was presented in this research. This method, relying on a vector auto-regressive model of spatial signature dynamics, effectively satisfies the requirements in the literature for a long-range prediction method. It also takes into account real-time implementation issues through the use of a Kalman filter that recursively updates coefficient values without the need for large matrix inversions.

The study of mutual coupling considered effects at a very small scale corresponding to distances of under a wavelength. Vector channel propagation and prediction study worked at a larger scale by considering several wavelengths of mobile user displacement. At the highest level of Figure 6.1, is original research in SDMA system planning. This study, documented in Chapter 5, considers system performance at a very large scale, corresponding to hundreds of meters. Specifically, the hybrid ray-tracing / moment method system was applied to a novel study of SDMA microcells. These simulations determined cell architecture and quantified, for the first time, the impact on this architecture of downlink beamforming. Simulations were run to determine the distribution of multipath component delay and angle statistics. These statistics allowed comments to be made pertaining to the levels of inter-symbol and inter-chip

interference present in the system. They also allowed comments to be made on the type of array geometries that will be needed to optimize future SDMA base stations. Moment-method simulations along with multivariate optimization were used to conduct new research into antenna array pattern synthesis that takes into account cellular tower effects. This problem was identified through first-hand deployment of smart antenna base stations and, to the author's knowledge, has not been addressed in the literature.

In summary, this dissertation has demonstrated how interdisciplinary research can be applied to the holistic study of SDMA communications systems. This study used computational electromagnetic simulations, consideration of array signal processing algorithm performance, and field measurements using prototype smart antenna hardware, to gain new insights in next-generation SDMA systems.

Bibliography

[1] H. Liu and G. Xu, "A subspace method for signature waveform estimation in synchronous cdma systems," *IEEE Trans. on Communications*, vol. 44, pp. 1346-1354, October 1996.

[2] S. Y. Kim and G. Xu, "Antenna gain for adaptive smart antenna system," *Proc. of IEEE Vehicular Technology Conference*, vol. 2, pp. 1168-1172, May 1997.

[3] J. Kang, S. Y. Kim, A. Kavak, and G. Xu, "Improved fast algorithm for spatial signature estimation," *Proceedings of ICASSP 2000*, vol. 5, pp. 3085-3088, June 2000.

[4] H. Krim and M. Viberg, "Two decades of array signal processing research: the parametric approach," *IEEE Signal Processing Magazine*, vol. 13, pp. 67-94, July 1996.

[5] A. Kavak, W. Yang, S. Kim, K. R. Dandekar, and G. Xu, "Experimental studies of indoor propagation characteristics of a smart antenna system at 1.8 GHz," *SPIE Aerosense Proceedings '99*, March 1999.

[6] R. Ertel, P. Cardieri K. Sowerby, T. Rappaport, and J. Reed, "Overview of spatial channel models for antenna array communication systems," *IEEE Personal Communications Magazine*, vol. 5, pp. 10-22, February 1998.

[7] L. Bigler, "Robust directional transmission beamforming techniques for smart antenna systems," *M.S. Thesis: Univ. of Texas at Austin*, 1998.

[8] S.-S. Jeng, G. Okamoto, G. Xu, H.-P. Lin, and W. Vogel, "Experimental evaluation of smart antenna system performance for wireless communications," *IEEE Trans. on Antennas and Propagation*, vol. 46, June 1998.

[9] K. R. Dandekar, "Space division multiple access systems: Using ray tracing for vector channel propagation study," *M.S. Thesis: Univ. of Texas at Austin*, 1998.

[10] B. Friedlander and A. Weiss, "Direction finding in the presence of mutual coupling," *IEEE Trans. on Antennas Propagation*, vol. 39, pp. 273-284, March 1991.

[11] J. Pierre and M. Kaveh, "Experimental performance of calibration and direction finding algorithms," *Proceedings of ICASSP 1991*, pp. 1365-1368, 1991.

[12] C. See, "A method for array calibration in parametric sensor array processing," *Proceedings of ICCS 1994*, pp. 915-919, 1994.

[13] C. See, "Sensor array calibration in the presence of mutual coupling and unknown sensor gains and phases," *Electronics Letters*, vol. 30, pp. 373-374, March 1994.

[14] A. Lemma, E. Deprettere, and A. van der Veen, "Experimental analysis of antenna coupling for high-resolution doa estimation algorithms," *1999 IEEE 2nd Workshop on Signal Processing Advances in Wireless Communications*, pp. 362-365, July 1999.

[15] I. Gupta and A. Ksienski, "Effect of mutual coupling on the performance of adaptive arrays," *IEEE Trans. on Antennas and Propagation*, vol. 31, Sept. 1983.

[16] K. Pasala and E. Friel, "Mutual coupling effects and their reduction in wideband direction of arrival estimation," *IEEE Trans. on Aerospace and Electronic Systems*, vol. 30, Oct. 1994.

[17] T. Svantesson, *Direction finding in the presence of mutual coupling*, Chalmers University of Technology Technical Report No. 307L, 1999.

[18] T. Su, K. R. Dandekar, and H. Ling, "Simulation of mutual coupling effect in circular arrays for direction finding applications," *Microwave and Optical Technology Letters*, Sept. 2000.

[19] R. Adve and T. Sarkar, "Compensation for the effects of mutual coupling on direct data domain adaptive algorithms," vol. 48, Jan. 2000.

[20] C. Balanis, Antenna Theory: Analysis and Design 2nd Edition, Wiley & Sons, New York, 1998.

[21] A. Paulraj and T. Kailath, "Direction of arrival estimation by eigenstructure method with unknown sensor gain and phase," *Proceedings of ICASSP 1998*, pp. 640-643, March 1985.

[22] G. J. Burke and A. J. Poggio, "Numerical electromagnetics code (nec)-method of moments," Technical Document 11, Naval Ocean Systems Center, San Diego, Calif., Jan. 1981.

[23] A. Kavak, M. Torlak, W.J. Vogel, and G. Xu, "Measurements, statistical modeling, and directional properties in outdoor environments," *IEEE Trans. on Microwave Theory and Techniques*, vol. 48, pp. 930-937, June 2000.

[24] S. Jeng, G. Xu, H.-P. Lin, and W.J. Vogel, "Experimental studies of spatial signature variation at 900 mhz for smart antenna systems," *IEEE Trans. on Antennas and Propagation*, vol. 46, pp. 953-962, July 1998.

[25] J. Winters, "Smart antennas for wireless systems," *IEEE Personal Communications Magazine*, pp. 23-27, Feb. 1998.

[26] K. R. Dandekar, A. Arredondo, G. Xu, and H. Ling, "Using ray tracing to study urban vector channel propagation characteristics," *Proceedings of the 1999 Vehicular Technology Conference*, vol. 1, pp. 381-385.

[27] A. Arredondo, K. R. Dandekar, G. Xu, "The quantitative effects of inaccurate uplink spatial signature observations on downlink signal to interference ratio," *1999 IEEE 2nd Workshop on Signal Processing Advances in Wireless Communications*, pp. 345-349, July 1999.

[28] V. Erceg, S. Fortune, J. Ling, A. Rustako, and R. Valenzuela, "Comparisons of a computer-based propagation prediction tool with experimental data collected in urban microcellular environments," *IEEE Journal on Selected Areas in Communications*, vol. 15, pp. 677-684, May 1997.

[29] L. Greenstein, N. Amitay, T. Chu, L. Cimini, G. Foschini, M. Gans, C. Lin, A. Rustako, R. Valenzuela, and G. Vannucci, "Microcells in personal communications systems," *IEEE Communications Magazine*, pp. 76-88, December 1992.

[30] M. Lawton and J. McGeehan, "The application of a deterministic ray launching algorithm for the prediction of radio channel characteristics in

small-cell environments," *IEEE Trans. on Vehicular Technology*, vol. 43, pp. 955-968, November 1994.

[31] M. F. Catedra, J. Perez, F. Saez de Adana and O. Guiterrez, "Efficient ray tracing techniques for three-dimensional analysis of propagation in mobile communications: application to picocell and microcell scenarios," *IEEE Antennas and Propagation Magazine*, vol. 40, pp. 15-28, April 1998.

[32] S. Lee, J. Baldauf, and R. Kipp, "CPATCH: antenna coupling in complex environments," *DEMACO Tech. Rep.*, Champaign, IL, October 1994.

[33] G. Benavides, "A Fast Algorithm to Calculate Channel Characteristics of an Urban Environment" *M.S. Thesis: Univ. of Texas at Austin*, 1998.

[34] I. Kelly, G. Benavides, R. Bhalla, H. Ling, W. Vogel, and M. Foltz, "Urban channel propagation modeling using the shooting and bouncing ray technique," *IEEE Antennas and Propagation Society International Symposium 1997 Digest*, vol. 3, pp. 2018-2021, July 1997.

[35] R. Lytle, "Measurement of earth medium electrical characteristics: techniques, results, and applications," *IEEE Trans. on Geoscience Electronics*, vol. 12, no. 3, pp. 81-101, 1974.

[36] A. Kavak, W.J. Vogel, and G. Xu, "Using gps to measure ground complex permittivity," *Electronics Letters*, vol. 34, no. 3, pp. 254-255, February 1998.

[37] A. Fourie and D. Nitch, "SuperNEC: antenna and indoor-propagation simulation program," *IEEE Antennas and Propagation Magazine*, vol. 42, pp. 31-48, June 2000.

[38] A. Kuchar, J.-P. Rossi, and E. Bonek, "Directional macro-cell channel characterization from urban measurements," *IEEE Trans. on Antennas and Propagation*, vol. 48, pp. 137-147, February 2000.

[39] K. R. Dandekar, A. Arredondo, G. Xu, and H. Ling, "Using ray tracing to evaluate smart antenna system performance in outdoor wireless communications," *SPIE Aerosense Proceedings '99*, March 1999.

[40] A. Duel-Hallen, S. Hu, and H. Hallen, "Long-range prediction of fading signals," *IEEE Signal Processing Magazine*, vol. 17, pp. 62-75, 2000.

[41] A. Arredondo, "Using an adaptive linear prediction filter for downlink beamforming: a proof of concept," Department of Electrical and Computer Engineering Seminar, Univ. of Texas at Austin, July, 1997.

[42] A. Arredondo, "A method to model and predict the mobile vector channel," Univ. of Texas at Austin, Department of Electrical and Computer Engineering Seminar, April, 1999.

[43] A. Arredondo, K. Dandekar, and G. Xu, "Vector channel modeling and prediction for improvement of downlink signal-to-noise ratio," *IEEE Transactions on Communications*, Submitted for Publication.

[44] A. Harvey, Time series models: second edition, The MIT Press, Cambridge, Massachusetts, 1993.

[45] G. Casella and R. Berger, Statistical inference, Duxbury Press, Belmont, California, 1990.

[46] D. Everitt, "Traffic engineering of the radio interface for cellular mobile networks," P*roceedings of the IEEE*, vol. 82, no. 9, pp. 1371-1382, September 1994.

[47] S. Rappaport and L. Hu, "Microcellular communication systems with hierarchical macrocell overlays: traffic performance models and analysis," *Proceedings of the IEEE*, vol. 82, no. 9, pp. 1383-1397, September 1994.

[48] J. Liberti and T. Rappaport, Smart antennas for wireless communications: is-95 and third generation cdma applications, Prentice Hall Communications Engineering and Emerging Technologies Series, Upper Saddle River, New Jersey, 1999.

[49] M. Catedra and J. Perez-Arriaga, Cell planning for wireless communications, Artech House, Boston, Massachusetts, 1999.

[50] H. Aroudaki and K. Bandelow, "Effects of introducing adaptive antennas into existing gsm networks," *Proceedings of the IEEE Vehicular Technology Conference Spring 1999*, May 1999.

[51] F. Kronestedt and S. Andersson, "Migration of adaptive antennas into existing networks," *Proceedings of the IEEE Vehicular Technology Conference*, pp. 1670-1674, 1998.

[52] F. Chin, Y. Zhou, Y. Liang, and C. Ko, "Downlink capacity of multi-rate DS-CDMA with antenna array and SIR based power control in multi-cell environment," *Proceedings of the 2000 Vehicular Technology Conference*, vol. 1, pp. 116-121.

[53] D. Giancola, F. Margherita, S. Parolari, A. Picciriello, and U. Spagnolini, "Analysis of the spectral efficiency of a fully adaptive antenna array system in gsm/dcs networks," *Proceedings of the 1999 Vehicular Technology Conference*, vol. 1, pp. 812-815.

[54] W. Ye and A. Haimovich, "Performance of cellular cdma with cell site antenna arrays, rayleigh fading, and power control error," *IEEE Trans. on Communications*, vol. 48, pp. 1151-1159.

[55] A. Levy, C. Cordier, L. Farache, and S. Mayrargue, "Impact of practical implementation errors on the capacity of cellular networks using adaptive antennas," *Proceedings of the 1997 Vehicular Technology Conference*, vol. 2, pp.1233-1237.

[56] R. Menolascino, M. Pizarroso, F. Galliano, B. Salas, "Planning a third generation mobile network with adaptive antennas," *Proceedings of the 1999 Vehicular Technology Conference*, vol. 1, pp.648-652.

[57] A. Naguib, A. Paulraj, and T. Kailath, "Capacity improvement with base-station antenna arrays in cellular cdma," *IEEE Trans. on Vehicular Technology*, vol. 43, pp. 691-698.

[58] S. Swales, M. Beach, and D. Edwards, "Adaptive antenna arrays for future generation cellular communications networks," *Proceedings of the Sixth International Conference on Antennas and Propagation*, vol. 1, pp. 321-325.

[59] M. Wells, "Adaptive antennas for frequency re-use in every cell of a gsm network," *IEE Colloquium on Mobile Communications Towards the Year 2000*, pp. 11/1-11/6.

[60] H. Dam, M. Berg, S. Andersson, R. Bormann, M. Frerich, F. Ahrens, and T. Henss, "Performance evaluation of adaptive antenna base stations in a commercial gsm network," *Proceedings of the 1999 Vehicular Technology Conference*, vol. 1, pp. 47-51.

[61] W. Lee, Mobile communications engineering: theory and applications, McGraw Hill Telecommunications, New York, 1998.

[62] A. Kavak, M. Torlak, W.J. Vogel, and G. Xu, "Mobile transmit diversity and TDD downlink performance for smart antennas in fast fading scenarios," *2000 IEEE Antennas and Propagation Society International Symposium*, vol. 2, pp. 944-947.

[63] A. Goldsmith and L. Greenstein, "A measurement-based model for predicting coverage areas of urban microcellular environments," *IEEE Trans. on Vehicular Technology*, vol. 11, pp.1013-1023.

[64] G. Xu, President and CTO of Navini Networks, Dallas TX. Personal interview, September, 2000.

[65] R. Daniels, An Introduction to Numerical Methods and Optimization, North-Holland, New York, 1978.